

# The IceCube Neutrino Observatory

## Contributions to ICRC 2017 Part II: Properties of the Atmospheric and Astrophysical Neutrino Flux

---

### Contents

<b>1 Search for Astrophysical Tau Neutrinos in Six Years of High-Energy Starting Events in IceCube — PoS (ICRC2017) 974</b>	<b>6</b>
<b>2 Multi-flavour PeV neutrino search with IceCube — PoS (ICRC2017) 1002</b>	<b>14</b>
<b>3 High Energy Astrophysical Neutrino Flux Measurement Using Neutrino-induced Cascades Observed in 4 Years of IceCube Data</b> PoS (ICRC2017) 968	<b>22</b>
<b>4 A Measurement of the Diffuse Astrophysical Muon Neutrino Flux Using Eight Years of IceCube Data — PoS (ICRC2017) 1005</b>	<b>30</b>
<b>5 Characterizing the Flux of Atmospheric Neutrinos with IceCube-DeepCore</b> PoS (ICRC2017) 1028	<b>38</b>
<b>6 Measurement of High Energy Neutrino – Nucleon Cross Section and Astrophysical Neutrino Flux Anisotropy Study of Cascade Channel with IceCube</b> — PoS (ICRC2017) 978	<b>46</b>
<b>7 Observation of Astrophysical Neutrinos in Six Years of IceCube Data</b> PoS (ICRC2017) 981	<b>54</b>
<b>8 All-flavor Multi-Channel Analysis of the Astrophysical Neutrino Spectrum with IceCube — PoS (ICRC2017) 976</b>	<b>62</b>
<b>9 Differential limit on an EHE neutrino flux component in the presence of astrophysical background from nine years of IceCube data</b> PoS (ICRC2017) 975	<b>70</b>
<b>10 Improving Future High-Energy Tau Neutrino Searches in IceCube</b> PoS (ICRC2017) 973	<b>78</b>

## 11 Search for Astrophysical Tau Neutrinos with the IceCube Waveforms

POS (ICRC2017) 1009

86

## IceCube Collaboration Member List

M. G. Aartsen<sup>2</sup>, M. Ackermann<sup>52</sup>, J. Adams<sup>16</sup>, J. A. Aguilar<sup>12</sup>, M. Ahlers<sup>20</sup>, M. Ahrens<sup>44</sup>, I. Al Samarai<sup>25</sup>, D. Altmann<sup>24</sup>, K. Andeen<sup>33</sup>, T. Anderson<sup>49</sup>, I. Anseau<sup>12</sup>, G. Anton<sup>24</sup>, C. Argüelles<sup>14</sup>, J. Auffenberg<sup>1</sup>, S. Axani<sup>14</sup>, H. Bagherpour<sup>16</sup>, X. Bai<sup>41</sup>, J. P. Barron<sup>23</sup>, S. W. Barwick<sup>27</sup>, V. Baum<sup>32</sup>, R. Bay<sup>8</sup>, J. J. Beatty<sup>18,19</sup>, J. Becker Tjus<sup>11</sup>, K.-H. Becker<sup>51</sup>, S. BenZvi<sup>43</sup>, D. Berley<sup>17</sup>, E. Bernardini<sup>52</sup>, D. Z. Besson<sup>28</sup>, G. Binder<sup>9,8</sup>, D. Bindig<sup>51</sup>, E. Blaufuss<sup>17</sup>, S. Blot<sup>52</sup>, C. Boehm<sup>44</sup>, M. Börner<sup>21</sup>, F. Bos<sup>11</sup>, D. Bose<sup>46</sup>, S. Böser<sup>32</sup>, O. Botner<sup>50</sup>, J. Bourbeau<sup>31</sup>, F. Bradascio<sup>52</sup>, J. Braun<sup>31</sup>, L. Brayeur<sup>13</sup>, M. Brenzke<sup>1</sup>, H.-P. Bretz<sup>52</sup>, S. Bron<sup>25</sup>, J. Brostean-Kaiser<sup>52</sup>, A. Burgman<sup>50</sup>, T. Carver<sup>25</sup>, J. Casey<sup>31</sup>, M. Casier<sup>13</sup>, E. Cheung<sup>17</sup>, D. Chirkin<sup>31</sup>, A. Christov<sup>25</sup>, K. Clark<sup>29</sup>, L. Classen<sup>36</sup>, S. Coenders<sup>35</sup>, G. H. Collin<sup>14</sup>, J. M. Conrad<sup>14</sup>, D. F. Cowen<sup>49,48</sup>, R. Cross<sup>43</sup>, M. Day<sup>31</sup>, J. P. A. M. de André<sup>22</sup>, C. De Clercq<sup>13</sup>, J. J. DeLaunay<sup>49</sup>, H. Dembinski<sup>37</sup>, S. De Ridder<sup>26</sup>, P. Desiati<sup>31</sup>, K. D. de Vries<sup>13</sup>, G. de Wasseige<sup>13</sup>, M. de With<sup>10</sup>, T. DeYoung<sup>22</sup>, J. C. Díaz-Vélez<sup>31</sup>, V. di Lorenzo<sup>32</sup>, H. Dujmovic<sup>46</sup>, J. P. Dumm<sup>44</sup>, M. Dunkman<sup>49</sup>, B. Eberhardt<sup>32</sup>, T. Ehrhardt<sup>32</sup>, B. Eichmann<sup>11</sup>, P. Eller<sup>49</sup>, P. A. Evenson<sup>37</sup>, S. Fahey<sup>31</sup>, A. R. Fazely<sup>7</sup>, J. Felde<sup>17</sup>, K. Filimonov<sup>8</sup>, C. Finley<sup>44</sup>, S. Flis<sup>44</sup>, A. Franckowiak<sup>52</sup>, E. Friedman<sup>17</sup>, T. Fuchs<sup>21</sup>, T. K. Gaisser<sup>37</sup>, J. Gallagher<sup>30</sup>, L. Gerhardt<sup>9</sup>, K. Ghorbani<sup>31</sup>, W. Giang<sup>23</sup>, T. Glauch<sup>1</sup>, T. Glüsenkamp<sup>24</sup>, A. Goldschmidt<sup>9</sup>, J. G. Gonzalez<sup>37</sup>, D. Grant<sup>23</sup>, Z. Griffith<sup>31</sup>, C. Haack<sup>1</sup>, A. Hallgren<sup>50</sup>, F. Halzen<sup>31</sup>, K. Hanson<sup>31</sup>, D. Hebecker<sup>10</sup>, D. Heereman<sup>12</sup>, K. Helbing<sup>51</sup>, R. Hellauer<sup>17</sup>, S. Hickford<sup>51</sup>, J. Hignight<sup>22</sup>, G. C. Hill<sup>2</sup>, K. D. Hoffman<sup>17</sup>, R. Hoffmann<sup>51</sup>, B. Hokanson-Fasig<sup>31</sup>, K. Hoshina<sup>31,a</sup>, F. Huang<sup>49</sup>, M. Huber<sup>35</sup>, K. Hultqvist<sup>44</sup>, M. Hünnefeld<sup>21</sup>, S. In<sup>46</sup>, A. Ishihara<sup>15</sup>, E. Jacobi<sup>52</sup>, G. S. Japaridze<sup>5</sup>, M. Jeong<sup>46</sup>, K. Jero<sup>31</sup>, B. J. P. Jones<sup>4</sup>, P. Kalaczynski<sup>1</sup>, W. Kang<sup>46</sup>, A. Kappes<sup>36</sup>, T. Karg<sup>52</sup>, A. Karle<sup>31</sup>, U. Katz<sup>24</sup>, M. Kauer<sup>31</sup>, A. Keivani<sup>49</sup>, J. L. Kelley<sup>31</sup>, A. Kheirandish<sup>31</sup>, J. Kim<sup>46</sup>, M. Kim<sup>15</sup>, T. Kintscher<sup>52</sup>, J. Kiryluk<sup>45</sup>, T. Kittler<sup>24</sup>, S. R. Klein<sup>9,8</sup>, G. Kohnen<sup>34</sup>, R. Koirala<sup>37</sup>, H. Kolanoski<sup>10</sup>, L. Köpke<sup>32</sup>, C. Kopper<sup>23</sup>, S. Kopper<sup>47</sup>, J. P. Koschinsky<sup>1</sup>, D. J. Koskinen<sup>20</sup>, M. Kowalski<sup>10,52</sup>, K. Krings<sup>35</sup>, M. Kroll<sup>11</sup>, G. Krückl<sup>32</sup>, J. Kunnen<sup>13</sup>, S. Kunwar<sup>52</sup>, N. Kurahashi<sup>40</sup>, T. Kuwabara<sup>15</sup>, A. Kyriacou<sup>2</sup>, M. Labare<sup>26</sup>, J. L. Lanfranchi<sup>49</sup>, M. J. Larson<sup>20</sup>, F. Lauber<sup>51</sup>, D. Lennarz<sup>22</sup>, M. Lesiak-Bzdak<sup>45</sup>, M. Leuermann<sup>1</sup>, Q. R. Liu<sup>31</sup>, L. Lu<sup>15</sup>, J. Lünemann<sup>13</sup>, W. Luszczak<sup>31</sup>, J. Madsen<sup>42</sup>, G. Maggi<sup>13</sup>, K. B. M. Mahn<sup>22</sup>, S. Mancina<sup>31</sup>, R. Maruyama<sup>38</sup>, K. Mase<sup>15</sup>, R. Maunu<sup>17</sup>, F. McNally<sup>31</sup>, K. Meagher<sup>12</sup>, M. Medici<sup>20</sup>, M. Meier<sup>21</sup>, T. Menne<sup>21</sup>, G. Merino<sup>31</sup>, T. Meures<sup>12</sup>, S. Miarecki<sup>9,8</sup>, J. Micallef<sup>22</sup>, G. Momenté<sup>32</sup>, T. Montaruli<sup>25</sup>, R. W. Moore<sup>23</sup>, M. Moulai<sup>14</sup>, R. Nahnhauser<sup>52</sup>, P. Nakarmi<sup>47</sup>, U. Naumann<sup>51</sup>, G. Neer<sup>22</sup>, H. Niederhausen<sup>45</sup>, S. C. Nowicki<sup>23</sup>, D. R. Nygren<sup>9</sup>, A. Obertacke Pollmann<sup>51</sup>, A. Olivás<sup>17</sup>, A. O’Murchadha<sup>12</sup>, T. Palczewski<sup>9,8</sup>, H. Pandya<sup>37</sup>, D. V. Pankova<sup>49</sup>, P. Peiffer<sup>32</sup>, J. A. Pepper<sup>47</sup>, C. Pérez de los Heros<sup>50</sup>, D. Pieloth<sup>21</sup>, E. Pinat<sup>12</sup>, M. Plum<sup>33</sup>, P. B. Price<sup>8</sup>, G. T. Przybylski<sup>9</sup>, C. Raab<sup>12</sup>, L. Rädcl<sup>1</sup>, M. Rameez<sup>20</sup>, K. Rawlins<sup>3</sup>, I. C. Rea<sup>35</sup>, R. Reimann<sup>1</sup>, B. Relethford<sup>40</sup>, M. Relich<sup>15</sup>, E. Resconi<sup>35</sup>, W. Rhode<sup>21</sup>, M. Richman<sup>40</sup>, S. Robertson<sup>2</sup>, M. Rongen<sup>1</sup>, C. Rott<sup>46</sup>, T. Ruhe<sup>21</sup>, D. Ryckbosch<sup>26</sup>, D. Rysewyk<sup>22</sup>, T. Sälzer<sup>1</sup>, S. E. Sanchez Herrera<sup>23</sup>, A. Sandrock<sup>21</sup>, J. Sandroos<sup>32</sup>, S. Sarkar<sup>20,39</sup>, S. Sarkar<sup>23</sup>, K. Satalecka<sup>52</sup>, P. Schlunder<sup>21</sup>, T. Schmidt<sup>17</sup>, A. Schneider<sup>31</sup>, S. Schoenen<sup>1</sup>, S. Schöneberg<sup>11</sup>, L. Schumacher<sup>1</sup>, D. Seckel<sup>37</sup>, S. Seunarine<sup>42</sup>, J. Soedingrekso<sup>21</sup>, D. Soldin<sup>51</sup>, M. Song<sup>17</sup>, G. M. Spiczak<sup>42</sup>,

C. Spiering<sup>52</sup>, J. Stachurska<sup>52</sup>, M. Stamatikos<sup>18</sup>, T. Stanev<sup>37</sup>, A. Stasik<sup>52</sup>, J. Stettner<sup>1</sup>, A. Steuer<sup>32</sup>, T. Stezelberger<sup>9</sup>, R. G. Stokstad<sup>9</sup>, A. Stöbl<sup>15</sup>, N. L. Strotjohann<sup>52</sup>, G. W. Sullivan<sup>17</sup>, M. Sutherland<sup>18</sup>, I. Taboada<sup>6</sup>, J. Tatar<sup>9,8</sup>, F. Tenholt<sup>11</sup>, S. Ter-Antonyan<sup>7</sup>, A. Terliuk<sup>52</sup>, G. Tešić<sup>49</sup>, S. Tilav<sup>37</sup>, P. A. Toale<sup>47</sup>, M. N. Tobin<sup>31</sup>, S. Toscano<sup>13</sup>, D. Tosi<sup>31</sup>, M. Tselengidou<sup>24</sup>, C. F. Tung<sup>6</sup>, A. Turcati<sup>35</sup>, C. F. Turley<sup>49</sup>, B. Ty<sup>31</sup>, E. Unger<sup>50</sup>, M. Usner<sup>52</sup>, J. Vandenbroucke<sup>31</sup>, W. Van Driessche<sup>26</sup>, N. van Eijndhoven<sup>13</sup>, S. Vanheule<sup>26</sup>, J. van Santen<sup>52</sup>, M. Vehring<sup>1</sup>, E. Vogel<sup>1</sup>, M. Vraeghe<sup>26</sup>, C. Walck<sup>44</sup>, A. Wallace<sup>2</sup>, M. Wallraff<sup>1</sup>, F. D. Wandler<sup>23</sup>, N. Wandkowsky<sup>31</sup>, A. Waza<sup>1</sup>, C. Weaver<sup>23</sup>, M. J. Weiss<sup>49</sup>, C. Wendt<sup>31</sup>, J. Werthebach<sup>21</sup>, S. Westerhoff<sup>31</sup>, B. J. Whelan<sup>2</sup>, S. Wickmann<sup>1</sup>, K. Wiebe<sup>32</sup>, C. H. Wiebusch<sup>1</sup>, L. Wille<sup>31</sup>, D. R. Williams<sup>47</sup>, L. Wills<sup>40</sup>, M. Wolf<sup>31</sup>, J. Wood<sup>31</sup>, T. R. Wood<sup>23</sup>, E. Woolsey<sup>23</sup>, K. Woschnagg<sup>8</sup>, D. L. Xu<sup>31</sup>, X. W. Xu<sup>7</sup>, Y. Xu<sup>45</sup>, J. P. Yanez<sup>23</sup>, G. Yodh<sup>27</sup>, S. Yoshida<sup>15</sup>, T. Yuan<sup>31</sup>, M. Zoll<sup>44</sup>

<sup>1</sup>III. Physikalisches Institut, RWTH Aachen University, D-52056 Aachen, Germany

<sup>2</sup>Department of Physics, University of Adelaide, Adelaide, 5005, Australia

<sup>3</sup>Dept. of Physics and Astronomy, University of Alaska Anchorage, 3211 Providence Dr., Anchorage, AK 99508, USA

<sup>4</sup>Dept. of Physics, University of Texas at Arlington, 502 Yates St., Science Hall Rm 108, Box 19059, Arlington, TX 76019, USA

<sup>5</sup>CTSPS, Clark-Atlanta University, Atlanta, GA 30314, USA

<sup>6</sup>School of Physics and Center for Relativistic Astrophysics, Georgia Institute of Technology, Atlanta, GA 30332, USA

<sup>7</sup>Dept. of Physics, Southern University, Baton Rouge, LA 70813, USA

<sup>8</sup>Dept. of Physics, University of California, Berkeley, CA 94720, USA

<sup>9</sup>Lawrence Berkeley National Laboratory, Berkeley, CA 94720, USA

<sup>10</sup>Institut für Physik, Humboldt-Universität zu Berlin, D-12489 Berlin, Germany

<sup>11</sup>Fakultät für Physik & Astronomie, Ruhr-Universität Bochum, D-44780 Bochum, Germany

<sup>12</sup>Université Libre de Bruxelles, Science Faculty CP230, B-1050 Brussels, Belgium

<sup>13</sup>Vrije Universiteit Brussel (VUB), Dienst ELEM, B-1050 Brussels, Belgium

<sup>14</sup>Dept. of Physics, Massachusetts Institute of Technology, Cambridge, MA 02139, USA

<sup>15</sup>Dept. of Physics and Institute for Global Prominent Research, Chiba University, Chiba 263-8522, Japan

<sup>16</sup>Dept. of Physics and Astronomy, University of Canterbury, Private Bag 4800, Christchurch, New Zealand

<sup>17</sup>Dept. of Physics, University of Maryland, College Park, MD 20742, USA

<sup>18</sup>Dept. of Physics and Center for Cosmology and Astro-Particle Physics, Ohio State University, Columbus, OH 43210, USA

<sup>19</sup>Dept. of Astronomy, Ohio State University, Columbus, OH 43210, USA

<sup>20</sup>Niels Bohr Institute, University of Copenhagen, DK-2100 Copenhagen, Denmark

<sup>21</sup>Dept. of Physics, TU Dortmund University, D-44221 Dortmund, Germany

<sup>22</sup>Dept. of Physics and Astronomy, Michigan State University, East Lansing, MI 48824, USA

<sup>23</sup>Dept. of Physics, University of Alberta, Edmonton, Alberta, Canada T6G 2E1

<sup>24</sup>Erlangen Centre for Astroparticle Physics, Friedrich-Alexander-Universität Erlangen-Nürnberg,



D-91058 Erlangen, Germany

<sup>25</sup>Département de physique nucléaire et corpusculaire, Université de Genève, CH-1211 Genève, Switzerland

<sup>26</sup>Dept. of Physics and Astronomy, University of Gent, B-9000 Gent, Belgium

<sup>27</sup>Dept. of Physics and Astronomy, University of California, Irvine, CA 92697, USA

<sup>28</sup>Dept. of Physics and Astronomy, University of Kansas, Lawrence, KS 66045, USA

<sup>29</sup>SNOLAB, 1039 Regional Road 24, Creighton Mine 9, Lively, ON, Canada P3Y 1N2

<sup>30</sup>Dept. of Astronomy, University of Wisconsin, Madison, WI 53706, USA

<sup>31</sup>Dept. of Physics and Wisconsin IceCube Particle Astrophysics Center, University of Wisconsin, Madison, WI 53706, USA

<sup>32</sup>Institute of Physics, University of Mainz, Staudinger Weg 7, D-55099 Mainz, Germany

<sup>33</sup>Department of Physics, Marquette University, Milwaukee, WI, 53201, USA

<sup>34</sup>Université de Mons, 7000 Mons, Belgium

<sup>35</sup>Physik-department, Technische Universität München, D-85748 Garching, Germany

<sup>36</sup>Institut für Kernphysik, Westfälische Wilhelms-Universität Münster, D-48149 Münster, Germany

<sup>37</sup>Bartol Research Institute and Dept. of Physics and Astronomy, University of Delaware, Newark, DE 19716, USA

<sup>38</sup>Dept. of Physics, Yale University, New Haven, CT 06520, USA

<sup>39</sup>Dept. of Physics, University of Oxford, 1 Keble Road, Oxford OX1 3NP, UK

<sup>40</sup>Dept. of Physics, Drexel University, 3141 Chestnut Street, Philadelphia, PA 19104, USA

<sup>41</sup>Physics Department, South Dakota School of Mines and Technology, Rapid City, SD 57701, USA

<sup>42</sup>Dept. of Physics, University of Wisconsin, River Falls, WI 54022, USA

<sup>43</sup>Dept. of Physics and Astronomy, University of Rochester, Rochester, NY 14627, USA

<sup>44</sup>Oskar Klein Centre and Dept. of Physics, Stockholm University, SE-10691 Stockholm, Sweden

<sup>45</sup>Dept. of Physics and Astronomy, Stony Brook University, Stony Brook, NY 11794-3800, USA

<sup>46</sup>Dept. of Physics, Sungkyunkwan University, Suwon 440-746, Korea

<sup>47</sup>Dept. of Physics and Astronomy, University of Alabama, Tuscaloosa, AL 35487, USA

<sup>48</sup>Dept. of Astronomy and Astrophysics, Pennsylvania State University, University Park, PA 16802, USA

<sup>49</sup>Dept. of Physics, Pennsylvania State University, University Park, PA 16802, USA

<sup>50</sup>Dept. of Physics and Astronomy, Uppsala University, Box 516, S-75120 Uppsala, Sweden

<sup>51</sup>Dept. of Physics, University of Wuppertal, D-42119 Wuppertal, Germany

<sup>52</sup>DESY, D-15738 Zeuthen, Germany

<sup>a</sup>Earthquake Research Institute, University of Tokyo, Bunkyo, Tokyo 113-0032, Japan

**Acknowledgment:** The authors gratefully acknowledge the support from the following agencies and institutions: USA - U.S. National Science Foundation-Office of Polar Programs, U.S. National Science Foundation-Physics Division, University of Wisconsin Alumni Research Foundation, the Center for High Throughput Computing (CHTC) at the University of Wisconsin - Madison, the Open Science Grid (OSG) grid infrastructure and the Extreme Science and Engineering Discovery Environment (XSEDE); U.S. Department of Energy, and National Energy Research Scientific Computing Center; Particle Astrophysics research computing center at the University of Maryland; Institute for Cyber-Enabled Research at Michigan State University; Astroparticle Physics Computational Facility at Marquette University; Belgium - Funds for Scientific Research (FRS-FNRS and FWO), FWO Odysseus and Big Science programs, Belgian Federal Science Policy Office (Belspo); Germany - Bundesministerium für Bildung und Forschung (BMBF), Deutsche Forschungsgemeinschaft (DFG), Helmholtz Alliance for Astroparticle Physics (HAP), Initiative and Networking Fund of the Helmholtz Association; Deutsches Elektronen Synchrotron (DESY); Cluster of Excellence (PRISMA ? EXC 1098); High Performance Computing Cluster of the IT-Center of the RWTH Aachen; Sweden - Swedish Research Council, Swedish Polar Research Secretariat, Swedish National Infrastructure for Computing (SNIC), and Knut and Alice Wallenberg Foundation; Canada - Natural Sciences and Engineering Research Council of Canada, Calcul Québec, Compute Ontario, WestGrid and Compute Canada; Denmark - Villum Fonden, Danish National Research Foundation (DNRF); New Zealand - Marsden Fund, New Zealand; Australian Research Council; Japan - Japan Society for Promotion of Science (JSPS) and Institute for Global Prominent Research (IGPR) of Chiba University; Korea - National Research Foundation of Korea (NRF); Switzerland - Swiss National Science Foundation (SNSF).

## Search for Astrophysical Tau Neutrinos in Six Years of High-Energy Starting Events in IceCube

---

### The IceCube Collaboration<sup>†</sup>

<sup>†</sup> [http://icecube.wisc.edu/collaboration/authors/icrc17\\_icecube](http://icecube.wisc.edu/collaboration/authors/icrc17_icecube)

E-mail: [marcel.usner@icecube.wisc.edu](mailto:marcel.usner@icecube.wisc.edu)

The IceCube Neutrino Observatory at the geographic South Pole is a cubic kilometer Cherenkov detector built to measure high-energy neutrinos from cosmic sources. It has reported the detection of a diffuse flux of astrophysical neutrinos in the energy range from  $\sim 10$  TeV to  $\sim 10$  PeV consistent with a neutrino flavor ratio of  $\nu_e : \nu_\mu : \nu_\tau \simeq 1 : 1 : 1$  as expected from pion decay in astrophysical sources after propagation to Earth. However, no tau neutrino has been identified so far. Its observation would be a smoking gun for astrophysical neutrinos and constrain their possible sources. The double bang channel is most promising for identifying tau neutrino interactions. Its event signature is unique to the tau flavor, linking two consecutive particle showers from the charged current interaction of a tau neutrino with an ice nucleus and the subsequent decay of the produced tau lepton. It can only be well resolved at deposited energies above a few 100 TeV where the average tau decay length is larger than 20 m. Results are presented from an analysis which uses an optimized direct reconstruction of the double bang event signature using six years of high-energy starting events (HESE) in IceCube. It is the most recent search for tau neutrinos allowing a measurement of the high-energy flavor ratio which, for the first time, is sensitive to the tau neutrino fraction.

**Corresponding authors:** M. Usner<sup>\*1</sup>

<sup>1</sup> *DESY, Platanenallee 6, D-15738 Zeuthen, Germany*

*35th International Cosmic Ray Conference — ICRC217  
10–20 July, 2017  
Bexco, Busan, Korea*

---

<sup>\*</sup>Speaker.

## 1. Introduction

The IceCube Neutrino Observatory at the South Pole is a Cherenkov detector built to measure high-energy neutrinos from cosmic sources. A volume of  $\sim 1 \text{ km}^3$  of the Antarctic ice is instrumented with 5160 digital optical modules (DOMs). Neutrinos are observed via Cherenkov light emitted by secondary particles produced in deep-inelastic neutrino-nucleon interactions. Details about the detector instrumentation can be found in [1]. The IceCube collaboration has reported a diffuse flux of astrophysical neutrinos in the energy range from  $\sim 10 \text{ TeV}$  to  $\sim 10 \text{ PeV}$  using multiple years of operation [2, 3, 4, 5]. It is consistent with an observed flavor ratio of  $\nu_e : \nu_\mu : \nu_\tau = 1 : 1 : 1$ , however no tau neutrino interaction has been identified so far. IceCube has observed many track-like events which can be readily distinguished from cascade-like events. While track-like events are generated in  $\nu_\mu$  interactions, cascade-like events may be generated in both  $\nu_e$  and  $\nu_\tau$  as well as neutral current interactions. Therefore, the knowledge about the tau neutrino fraction is largely unconstrained since no tau neutrino interaction could be identified so far.

An observation of a tau neutrino interaction in IceCube would be interesting for three reasons. First, it could significantly improve the measurement precision of the astrophysical flavor ratio and thus constrain possible production mechanisms and sources of cosmic neutrinos. The expected ratio of  $\sim 1 : 1 : 1$  at Earth arises from the assumption that neutrinos are produced in the decays of charged pions and secondary muons leading to a flavor ratio of  $1 : 2 : 0$  at the source [6]. There are other source scenarios like the muon-damped case with  $0 : 1 : 0$  and the neutron-beam case with  $1 : 0 : 0$  at the source leading to detectable flavor ratios at Earth that deviate from the usually modeled  $1 : 1 : 1$  expectation [7, 8]. Second, atmospheric tau neutrinos from cosmic ray air showers are strongly suppressed. In the relevant energy range above  $100 \text{ TeV}$  the atmospheric neutrino flux is expected to be dominated by a charm component of which almost entirely only the  $D_s$  decay produces detectable tau neutrinos. The flavor ratio of the prompt neutrino flux is expected to be of the order of  $\sim 1 : 1 : 0.1$ . Taking current upper limits on a prompt neutrino flux into consideration [9], the observation of a tau neutrino event around  $1 \text{ PeV}$  in IceCube is  $\sim 100$  times more likely to be of astrophysical than of atmospheric origin. Third, only few tau neutrinos have ever been detected in dedicated accelerator experiments and none at energies accessible to IceCube [10, 11].

There are many different signatures of tau neutrino interactions in IceCube. The most interesting signature is the "double bang" (or "double cascade"). A charged current tau neutrino interaction creates a hadronic cascade and a tau lepton that decays into a hadronic or an electromagnetic cascade, thereby linking two subsequent cascades. It accounts for  $\sim 59\%$  of all tau neutrino interactions. The mean decay length of the tau lepton scales with its energy and is on average  $\sim 50 \text{ m}$  per  $\text{PeV}$  tau energy. Therefore, most double cascade events at energies below  $\sim 100 \text{ TeV}$  cannot be resolved in IceCube and effectively look like single cascades.

Without tau neutrino identification, previous all-flavor ratio measurements were only based on distinguishing track-like from cascade-like events and thus showed a large degeneracy between the electron- and tau-neutrino fractions [12, 13]. The most recent direct search for tau neutrino interactions in IceCube has seen no events and set an integrated upper limit on the tau neutrino flux of  $\phi_{\nu_\tau}(E_{\nu_\tau}) < 5.1 \cdot 10^{-18} (E_{\nu_\tau}/100 \text{ TeV})^{-2} \text{ GeV}^{-1} \text{ cm}^{-2} \text{ sr}^{-1} \text{ s}^{-1}$  [14]. A combination of both results discussed in [13] and [14] gave the most stringent all-flavor ratio measurement including the most sensitive constraint on the tau neutrino fraction so far [15].

The analysis presented here introduces a new identification method of tau neutrino interactions in IceCube by explicitly reconstructing events with a double cascade hypothesis. It aims at the discovery of the first tau neutrino interaction in IceCube and the measurement of the astrophysical neutrino flavor ratio sensitive to all flavors. It uses the high-energy starting events collected between 2010 and 2016 in the energy range between 60 TeV and 10 PeV deposited electromagnetic-equivalent energy. The sensitivity increases by identifying tau neutrino events with a decay length as low as  $\sim 20$  m and a deposited electromagnetic-equivalent energy above  $\sim 100$  TeV. In Section 2 the well-known data sample of high-energy starting events is revisited and the reconstruction of double cascade events is described. In Section 3 the observables, analysis method and systematic uncertainties are explained. The results are discussed in Section 4 and summarized in Section 5.

## 2. Data Sample and Event Reconstruction

The data sample used for this analysis is the high-energy starting event selection (HESE) [2]. Neutrino events are identified by defining the outer detector boundary as a veto region and by requiring that no more than 3 of the first 250 photoelectrons occur within the veto. In addition, at least 6000 photoelectrons are required per event corresponding to an energy threshold of  $\sim 30$  TeV deposited electromagnetic-equivalent energy. Recently this event selection was updated to include a total of six years of data and now consists of 82 events [5]. Above a deposited energy of 60 TeV considered for this analysis there are 49 events on a total estimated atmospheric background of  $9.0^{+3.4}_{-1.9}$ .

Three starting event topologies are considered (see Figure 1). **Single cascades** are produced in electron-neutrino and all-flavor neutral current interactions. **Double cascades** are only produced in charged current tau neutrino interactions where the tau lepton decay produces either a hadronic or an electromagnetic cascade. **Tracks** are produced by muons in charged current muon neutrino interactions, in charged current tau neutrino interactions where the tau lepton decays into a muon and by muons from atmospheric air showers that do not trigger the veto condition.

Reconstruction of cascade- and track-like events is well established in IceCube [16]. An event is reconstructed using a maximum-likelihood fit where the expected arrival time distribution of photoelectrons from a hypothesis is compared to the observed distribution at each DOM. For the first time double cascade events are explicitly reconstructed. The event hypothesis is constructed by extending a single cascade hypothesis by two more parameters: the decay length and the electromagnetic-equivalent energy deposited in the decay. Consequently, the second (decay) cascade is related to the first (interaction) cascade by assuming the two are connected by a particle traveling at the speed of light and in the same direction as the primary neutrino. Both assumptions are perfectly reasonable considering the energy scale and resolution of IceCube.

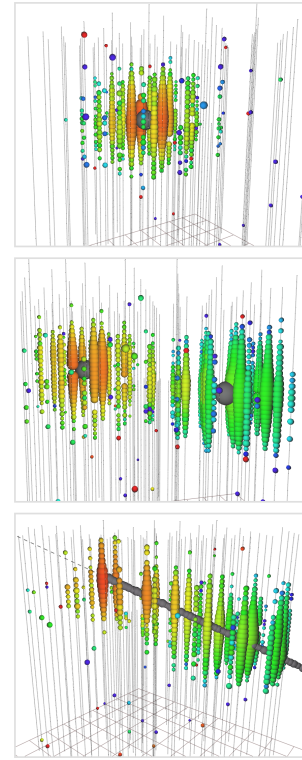


**Figure 1:** Simulated starting event topologies: single cascade (top), double cascade (middle) and track (bottom).

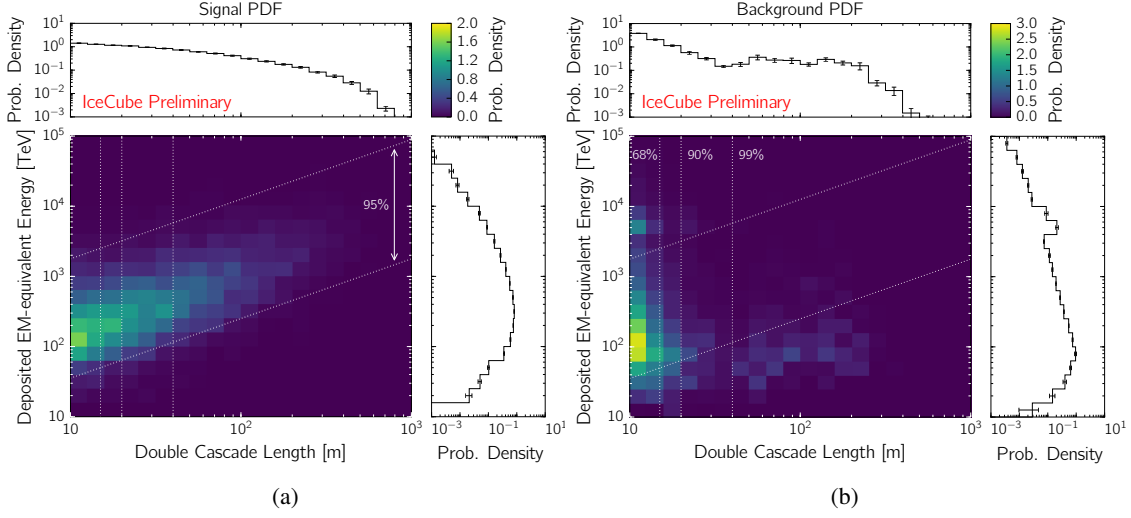


**Figure 2:** Probability density distributions in the double cascade sample for (a) charged current tau neutrino events where the tau lepton decay produces either a hadronic or an electromagnetic cascade and (b) for all remaining events including atmospheric and astrophysical backgrounds assuming an  $E_\nu^{-2.3}$  astrophysical neutrino flux. The observables are the total deposited electromagnetic-equivalent energy and the double cascade length. They show a linear correlation for signal events due to the energy dependence of the mean decay length of the tau lepton. The diagonal lines indicate the 95% signal containment and the vertical lines indicate the 68%, 90% and 99% background exclusion, respectively. The dominant background close to the threshold of 10m double cascade length are misreconstructed single cascades.

Each event is reconstructed assuming all three event hypotheses. If the best-fit of the double cascade reconstruction does not result in both cascades having at least 1 TeV deposited energy and a vertex with a maximum distance of 50m outside the fiducial volume, the event is classified as single cascade or track based on which hypothesis has a greater likelihood. For all remaining double cascade candidate events two topology estimators are defined on the basis of the reconstructed vertex positions and energies of the double cascade event hypothesis. The **energy asymmetry**  $E_A = (E_1 - E_2)/(E_1 + E_2)$  quantifies how much of the total deposited energy can be attributed either to the first or the second vertex. An energy asymmetry of  $\pm 1$  means that the event is a single cascade by definition. The **energy confinement**  $E_C = (E_{C,1} + E_{C,2})/E_{\text{tot}}$  gives the relation between the deposited energy  $E_{C,i}$  that is confined to a region of  $\pm 40\text{m}$  around the vertex position of each cascade  $i = 1, 2$  and the total deposited energy  $E_{\text{tot}}$  that is obtained from the deconvolution of all possible energy losses along the track hypothesis. An energy confinement close to 1 means that the event is very likely either a single or a double cascade. Events are classified as tracks by requiring  $E_C < 0.99$ . Double cascade events are selected by requiring a length greater than 10m,  $E_C \geq 0.99$  and  $-0.98 \leq E_A \leq 0.3$ . All remaining events are classified as single cascades. Consequently, a **ternary particle id** (PID) is constructed using this classification scheme for three event topologies.

The total deposited energy and the decay length are used as observable for all events classified as double cascades by this PID selection method (see Figure 2). Although the deposited energy is not a direct measure of the tau energy the correlation between the mean decay length and the energy of the tau lepton (c.f. Section 1) also holds for the total deposited energy. The correlation of the total deposited energy and the decay length is clearly visible for the signal distribution. Since the

decay length of the tau lepton scales with its energy and the astrophysical neutrino flux is falling steeply with energy, most double cascade events in the six-year data sample are expected to look very similar to single cascades – in contrast to the event signature illustrated in Figure 1 (middle). In fact, only  $\sim 25\%$  of all tau neutrino events expected in the HESE data sample have a decay length greater than 10m. The mean selection efficiency of these events is  $\sim 50\%$ . The average misidentification fraction for single cascades and tracks is  $\sim 10\%$  and the misidentification fraction for double cascades ranges from  $\sim 50\%$  to  $\sim 5\%$  depending on the tau decay length. Successfully identified tau neutrino events have a median resolution of  $\sim 3$  m decay length and a neutrino energy range from  $\sim 200$  TeV to  $\sim 10$  PeV.

### 3. Analysis

The analysis method to measure the astrophysical neutrino flavor ratio is a binned maximum-likelihood fit where a sum of Monte Carlo templates each containing the observables for an astrophysical or an atmospheric flux component is varied until it best describes the experimental data. The likelihood is constructed using the Poisson probability for each observation bin and a Gaussian penalty factor for each nuisance parameter using prior knowledge of the systematic errors [13].

The observables used in the likelihood fit are the total deposited electromagnetic-equivalent energy and the zenith angle for the single cascade sample and the track sample. For the double cascade sample the total deposited electromagnetic-equivalent energy and the double cascade length are used. The dependence on the zenith angle is omitted in the double cascade sample due to limited statistics. It is used in the single cascade and track samples because it constrains the atmospheric background. In the double cascade sample, however, most of the background above 60 TeV is of astrophysical origin, hence the loss of information is inconsequential.

The astrophysical neutrino flux is modeled as a single power-law without a spectral cut-off. The flavor normalizations  $\phi_{\nu_e}$ ,  $\phi_{\nu_\mu}$  and  $\phi_{\nu_\tau}$  as well as the common spectral index  $\gamma$  are free parameters of the fit. The atmospheric muon flux is based on the pure-proton extragalactic composition of the H3a composition model [17] using SYBILL 2.1 as hadronic interaction model [18]. It is renormalized to the number of expected muons estimated from events that are tagged in the veto region of the detector as described in [2]. The atmospheric muon flux is modeled with a statistical error of  $\pm 30\%$  that is determined from the number of these tagged events in experimental data. The HKKMS06 model [19] is used to describe the conventional atmospheric neutrinos from the decay of pions and kaons and the ERS model [20] is used to describe the prompt atmospheric neutrinos from the decay of charmed mesons. Both models are modified to match newer measurements of the primary cosmic ray spectrum in the "knee" region based on the H3a composition model [17, 21]. Furthermore, both atmospheric neutrino fluxes are modified with the generalized self-veto probability as described in [22] to account for the self-veto effect of atmospheric neutrinos accompanying the vetoed muons from the same cosmic ray induced air shower in the atmosphere. An uncertainty of  $\pm 30\%$  on the conventional atmospheric neutrino flux includes uncertainties of the cosmic ray spectrum and composition ( $\pi/K$  ratio) and hadronic interactions models. Since no prompt neutrino flux has been observed so far the prior is set to zero and the uncertainty is estimated to be  $+65\%$  in units of ERS which is derived from the 90% upper prompt limit from the six-year diffuse muon neutrino observation [9].



An energy scale is introduced as a systematic nuisance parameter that accounts for a potential bias of  $\pm 15\%$  on the deposited electromagnetic-equivalent energy. It arises from a  $\pm 10\%$  uncertainty on the relative DOM efficiency and a  $^{+10\%}_{-7\%}$  uncertainty on the scattering and absorption of the ice model. An additional systematic nuisance parameter is an ice anisotropy scale that accounts for a potential bias on the double cascade length based on the modulation of the nominal ice scattering of  $^{+4\%}_{-8\%}$  known as ice anisotropy [23]. Its uncertainty is estimated to be  $\pm 30\%$ .

The main parameters of interest for constraining the flavor ratio are the astrophysical flux normalizations  $\phi_{\nu_e}$ ,  $\phi_{\nu_\mu}$  and  $\phi_{\nu_\tau}$ . Sensitivity calculations are based on a 1 : 1 : 1 flavor ratio assuming an astrophysical per-flavor flux of  $\phi_\nu(E_\nu) = 1.5 \cdot 10^{-18} (E_\nu/100 \text{ TeV})^{-2.3} \text{ GeV}^{-1} \text{ cm}^{-2} \text{ sr}^{-1} \text{ s}^{-1}$  corresponding to the best-fit in [3]. The expected number of events in the double cascade sample for a six-year dataset with this spectrum is  $2.318^{+0.038}_{-0.029}$  tau neutrino events on a total astrophysical and atmospheric background of  $0.939^{+0.219}_{-0.092}$  events. The majority of tau neutrino events are not identifiable as such and are thus classified as single cascades for neutral current interactions or charged current interactions where the tau decay length is too short or as tracks if the tau lepton decays into a muon. The number of identifiable tau neutrino events is strongly dependent on the assumed astrophysical neutrino flux and can be significantly reduced by a steeper spectrum, a spectral cut-off or a more complex spectral shape.

The sensitivity to constrain the tau neutrino flux is defined as median detection significance of the best-fit hypothesis compared to the null hypothesis where the tau neutrino flux is zero using a likelihood ratio test. Injecting the aforementioned astrophysical flux at a flavor ratio of 1 : 1 : 1 and modeling the test-statistic distribution as a  $\chi^2$  distribution with one degree of freedom under the assumption of Wilks' theorem [24] the median detection significance for a six-year dataset is  $2.5 \sigma$ . The all-flavor ratio sensitivity is derived from a two-dimensional profile likelihood scan comparing each test point to the best-fit hypothesis using a likelihood ratio test. The confi-

dence levels are determined by modeling the test-statistic distribution as a  $\chi^2$  distribution with two degrees of freedom. In Figure 3 this profile likelihood scan around the best-fit of the injected flavor ratio of 1 : 1 : 1 is shown for a binary PID of cascades and tracks and a ternary PID of single cascades, double cascades and tracks using the Asimov dataset [25]. The binary PID corresponds to the method used in previous HESE publications and the ternary PID is the extension described here. It can clearly be seen how the degeneracy in the electron- and tau-neutrino fractions is decreased by the introduction of observables that are sensitive to the double cascade topology.

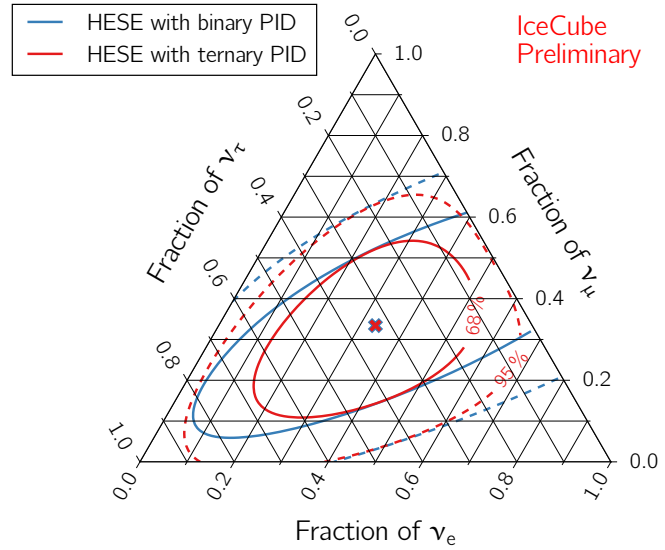


**Figure 3:** Median all-flavor ratio sensitivity using a binary PID of cascades and tracks (standard HESE) and a ternary PID of single cascades, double cascades and tracks (this work)



## 4. Results

No tau neutrino candidate event with a deposited energy above 60 TeV was observed. Consequently, the best-fit of the tau neutrino normalization is zero. The total astrophysical flux normalization and spectral index are consistent with the results discussed in [5]. The integrated 90% upper limit of the tau neutrino flux is  $\phi_{\nu_\tau}(E_{\nu_\tau}) < 2.95 \cdot 10^{-18} (E_{\nu_\tau}/100 \text{ TeV})^{-2.94} \text{ GeV}^{-1} \text{ cm}^{-2} \text{ sr}^{-1} \text{ s}^{-1}$ . The best-fit astrophysical neutrino fractions are  $f_{\nu_e} = 0.51^{+0.12}_{-0.13}$ ,  $f_{\nu_\mu} = 0.49^{+0.12}_{-0.13}$  and  $f_{\nu_\tau} = 0.00^{+0.16}_{-0.00}$  which correspond to a flavor ratio of  $\sim 1 : 1 : 0$ . A two-dimensional profile likelihood scan around the best-fit flavor ratio is shown in Figure 4. The flavor ratio of  $\sim 1 : 1 : 1$  expected from pion decay at the source is in agreement with the best-fit. The previously published flavor ratio measurement is shown in comparison [13]. Note that these contours are smaller with respect to the electron- and muon-neutrino fractions since they are derived from the combination of multiple data samples (including HESE) that contain a large number of track-like events. However, the tau neutrino fraction can be constrained better with the method presented here due to the increased sensitivity in the double cascade channel. This result will be included in a similar combined analysis in the future.

The lack of tau neutrino candidate events is best explained by either a statistical fluctuation or a spectral shape that is more complex than a single unbroken power-law. The updated HESE data sample including two more years revealed a lack of events with a deposited electromagnetic-equivalent energy above 200 TeV. The accumulation of more low-energy and fewer high-energy events might arise from a more complex spectral composition. However, it is not possible to distinguish more complex models from the assumed single power-law model with the currently available data. For a differential flux model with reduced assumptions on the spectral shape by fitting an independent flux normalization in each energy band [5], the prediction of identifiable tau neutrino events is  $1.441^{+0.024}_{-0.018}$  on a total background of  $0.938^{+0.219}_{-0.092}$  events, assuming a flavor ratio of  $1 : 1 : 1$ . Not observing any tau neutrino candidate event then corresponds to a p-value of 9.3%.

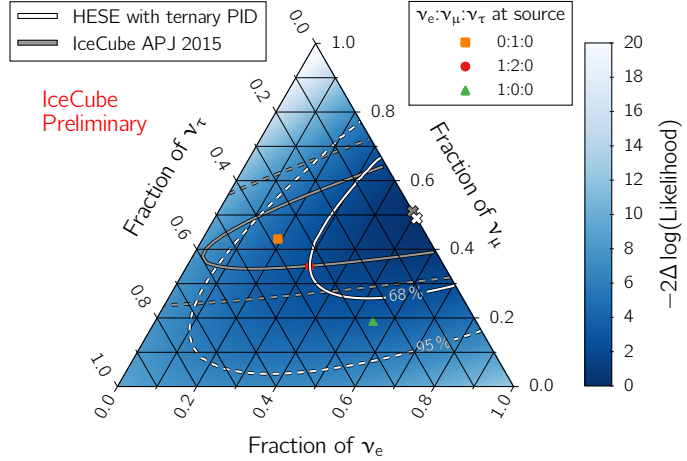


**Figure 4:** All-flavor ratio measurement using the ternary PID (this work) on the six-year HESE data sample. The best-fit is marked with 'x'. The solid and dashed lines show the 68% and 95% contours, respectively. Compositions expected at Earth are marked for three different source scenarios. The gray lines show the previously published 68% and 95% contours [13].

## 5. Summary and Future Plans

The work presented here extends the high-energy starting event analysis by introducing the reconstruction of a double cascade event hypothesis. On the basis of tau neutrino sensitive observ-

ables a ternary PID is defined to measure the astrophysical flavor ratio and constrain the tau neutrino fraction with an improved sensitivity. No tau neutrino candidates were observed. The measured flavor ratio of  $\sim 1 : 1 : 0$  is in agreement with an expectation of  $\sim 1 : 1 : 1$  from pion decay at the source. There are multiple efforts to improve the constraints on the astrophysical neutrino flavor ratio by combining numerous event selections [26], by extending the double cascade reconstruction to events in the entire fiducial volume (including the veto region) [27] and by improving alternative detection methods of tau neutrino interactions [28].

## References

- [1] **IceCube** Collaboration, M. G. Aartsen et al., *JINST* **12** (2017) P03012.
- [2] **IceCube** Collaboration, M. G. Aartsen et al., *Science* **342** (2013) 1242856.
- [3] **IceCube** Collaboration, M. G. Aartsen et al., *Phys. Rev. Lett.* **113** (2014) 101101.
- [4] **IceCube** Collaboration, [PoS \(ICRC2015\) 1081](#) (2016).
- [5] **IceCube** Collaboration, [PoS \(ICRC2017\) 0981](#) (these proceedings).
- [6] H. Athar, C. S. Kim, and J. Lee, *Modern Physics Letters A* **21** (2006) 1049–1065.
- [7] P. Lipari, M. Lusignoli, and D. Meloni, *Phys. Rev. D* **75** (Jun, 2007) 123005.
- [8] M. Bustamante, J. F. Beacom, and W. Winter, *Phys. Rev. Lett.* **115** (2015) 161302.
- [9] **IceCube** Collaboration, M. G. Aartsen et al., *Astrophys. J.* **833** (2016) 3.
- [10] **OPERA** Collaboration, S. Dusini et al., *AIP Conference Proceedings* **1666** (2015) 110003.
- [11] **DONuT** Collaboration, K. Kodama et al., *Phys. Rev. D* **78** (Sep, 2008) 052002.
- [12] **IceCube** Collaboration, M. G. Aartsen et al., *Phys. Rev. Lett.* **114** (2015) 171102.
- [13] **IceCube** Collaboration, M. G. Aartsen et al., *Astrophys. J.* **809** (2015) 98.
- [14] **IceCube** Collaboration, M. G. Aartsen et al., *Phys. Rev. D* **93** (2016) 022001.
- [15] **IceCube** Collaboration, [PoS \(ICRC2015\) 1066](#) (2016).
- [16] **IceCube** Collaboration, M. G. Aartsen et al., *JINST* **9** (2014) P03009.
- [17] T. K. Gaisser, *Astropart. Phys.* **35** (2012) 801–806.
- [18] E.-J. Ahn, R. Engel, T. K. Gaisser, P. Lipari, and T. Stanev, *Phys. Rev. D* **80** (2009) 094003.
- [19] M. Honda, T. Kajita, K. Kasahara, S. Midorikawa, and T. Sanuki, *Phys. Rev. D* **75** (2007) 043006.
- [20] R. Enberg, M. H. Reno, and I. Sarcevic, *Phys. Rev. D* **78** (2008) 043005.
- [21] **IceCube** Collaboration, M. G. Aartsen et al., *Phys. Rev. D* **89** (2014) 062007.
- [22] T. K. Gaisser, K. Jero, A. Karle, and J. van Santen, *Phys. Rev. D* **90** (2014) 023009.
- [23] **IceCube** Collaboration, *Proceedings of ICRC2013 0580* (2014).
- [24] S. S. Wilks, *Annals Math. Statist.* **9** (1938) 60–62.
- [25] G. Cowan, K. Cranmer, E. Gross, and O. Vitells, *Eur. Phys. J.* **C71** (2011) 1554.
- [26] **IceCube** Collaboration, [PoS \(ICRC2017\) 0976](#) (these proceedings).
- [27] **IceCube** Collaboration, [PoS \(ICRC2017\) 0973](#) (these proceedings).
- [28] **IceCube** Collaboration, [PoS \(ICRC2017\) 1009](#) (these proceedings).

## Multi-flavour PeV neutrino search with IceCube

---

### The IceCube Collaboration<sup>†</sup>

<sup>†</sup> [http://icecube.wisc.edu/collaboration/authors/icrc17\\_icecube](http://icecube.wisc.edu/collaboration/authors/icrc17_icecube)

E-mail: [lu.lu@icecube.wisc.edu](mailto:lu.lu@icecube.wisc.edu)

The IceCube observatory, located at the South Pole has been completed in 2010 and is the largest neutrino detector in the world. PeV neutrinos have been discovered in previous analyses which were optimised for different event topologies. A new search has been developed to select PeV cascades that are not fully contained in the detector. It is therefore sensitive to the Glashow resonance at 6.3 PeV. Together with the existing high-energy-starting-events (HESE) and extreme-high-energy (EHE) channels, the combined event selection provides the highest sensitivity to the beyond-PeV region, where a cut-off in the spectrum could occur. We will show the sensitivities for six years of data taking to demonstrate the preferred scenario for the cut-off energies and possible constraints on the flavour-dependent cut-off. The result is important both for understanding the source properties and for providing the possibility of reliable astrophysical-background estimations of GZK neutrino searches.

**Corresponding authors:** L. Lu<sup>\*1</sup>

<sup>1</sup> *Department of Physics, Chiba University, Chiba 263-8522, Japan*

*35th International Cosmic Ray Conference - ICRC2017  
10-20 July, 2017  
Bexco, Busan, Korea*

---

\*Speaker.

## 1. Introduction

After more than a century since the discovery of cosmic-rays, we know little about their origins. These charged particles carry extreme energies and are expected to interact with gas and radiation at the source, producing pions which subsequently decay into neutrinos and photons. The fact that neutrinos are weakly-interactive makes them ideal messengers for studying the high-energy universe but also makes them hard to be detected. One example of indirect measurement of neutrinos is to detect Cherenkov photons, which are emitted by charged particles produced in the interactions between neutrinos and matter in a transparent medium such as in water or ice.

The IceCube Neutrino Observatory, located at the South Pole, was completed in 2010 with more than 5000 photo-sensors buried in the deep ice that instrument a volume of one cubic-kilometre to search for such Cherenkov photons. The detection of extraterrestrial neutrinos has been reported in [1] and in particular four neutrinos with deposited energy greater than 1 PeV have been found [2, 3, 4]. The discoveries by the IceCube collaboration opened a new window for multi-messenger astronomy that allows to probe the cosmic-ray sources and their properties via the neutrino channel. For instance, the energy of the neutrinos is expected to be  $\sim 5\%$  of the energy of the nucleon at the source. By measuring a cut-off in the energy spectrum of the neutrinos one could learn about the acceleration capability of the source. More importantly, a significant constraint on the existence of a spectral cut-off at high energies would provide information on whether the observed IceCube spectrum extends beyond few PeV, and if it might be connected with the sources of ultra-high energy cosmic-rays.

The Glashow resonance [5] at 6.3 PeV enhances the detection probability for electron anti-neutrinos and could be used to constrain a potential spectral cut-off in the PeV energy range. In this paper, we introduce a new event selection that was developed to recover PeV events which failed the selection criteria of both, the high-energy starting event sample (HESE) [2] and the extreme-high energy event sample for on-line alerts (EHE-PeV) [1, 7]. The sensitivity for constraining a cut-off with all three combined sample is shown for 6 years of data-taking.

## 2. A new channel for PeV neutrinos

Among the four multi-PeV events seen so far by IceCube, three are cascades with vertex positions inside the detector volume and one is a through-going track. Several analyses targeting different physics goals [1, 2, 4, 8] have detected these events independently. The HESE sample relies on a veto technique [2] to efficiently reject cosmic-ray background and only selects events with vertex positions located within the fiducial volume. The EHE-PeV sample selects through-going tracks induced by  $\nu_\mu$  with energies  $\sim 1$  PeV. To illustrate the characteristics of electron neutrinos selected by HESE, Figure 1(a) shows the vertex position of HESE-selected  $\nu_e$  events of energies greater than 1 PeV. Figure 1(b) shows events which are selected neither by HESE nor by EHE-PeV.

As expected, the HESE selection is limited by the fiducial volume. The gap at  $z \approx -200$  m indicates the position of the dust layer in the ice, which is known to feature strong absorption and scattering of light. High-energy events often register significant amount of signals in the detector but with a vertex position at or outside of the detector boundary. It is evident that to increase the

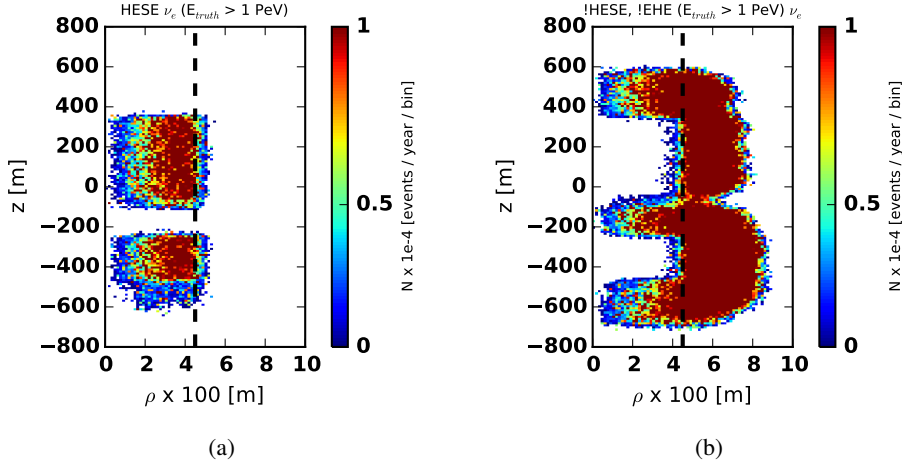


**Figure 1:** (a) Vertex positions of simulated multi-PeV electron neutrinos selected by HESE. (b) Vertex positions for those which failed the selection criteria of both, HESE and EHE-PeV. The colour scale indicates the event rate per bin.  $\rho, z$  denote cylindrical coordinates with the origin in the center of IceCube. The neutrino spectrum is assumed to be  $E^{-2}$  for neutrinos with  $\nu_e/\bar{\nu}_e = 1 : 1$ .

effective volume of the HESE sample, one needs to extend the allowed region for the interaction vertex position to the outside of the detector. The goal of this analysis is therefore the selection of PeV Energy Partially-contained Events (PEPE), with special focus on the Glashow resonance at 6.3 PeV. The dust-layer is also excluded in the new event selection.

Since the branching ratio of the  $W^-$  decay is  $\sim 67\%$  for hadron jets and  $\sim 11\%$  for electromagnetic showers, the dominant Glashow signals are cascade-like events. A previous study from IceCube [8] already explored the possibility of including the partially-contained cascade channel using a simple classification of the events based on their reconstructed properties. Here we propose to use machine-learning techniques to further enhance the classification of signal and background with emphasis on the signal purity at the energy of the Glashow resonance.

There are  $> 10^7$  events generating at least  $10^3$  photoelectrons in the ice per year although only few of which are expected to be PeV neutrino signals. The majority of the events are track-like background from muons produced by cosmic rays propagating in the atmosphere. To ensure the new event sample is statistically independent from the HESE and EHE-PeV samples, the events that pass the former two selections are excluded from the PEPE sample. Next a gradient-boosted decision tree (BDT) [9] was trained with 11 observables such as the rise time of the PMT waveform, and the displacement of the mean position of the detected photons from the interaction vertex. Note that none of the BDT inputs needs high-level reconstructions, which reduces the effects due to uncertainties on the ice properties. Only electron neutrinos of generated energies  $> 1$  PeV are labelled as signal in the training. Selection efficiencies and expected rates for signal and background at various steps in the selection process is shown in Figure 2.

Approximately  $\sim 20\%$  of the electron neutrinos are selected by HESE, leaving the remaining of  $\sim 80\%$  unexplored. By selecting events of BDT score  $> 0.5$ ,  $\sim 40\%$  of the PeV signals are saved by PEPE. The remaining 40% are rejected due to being located in the dust layer or having vertex positions too far away from the edge of the detector to be identified as signal. The events

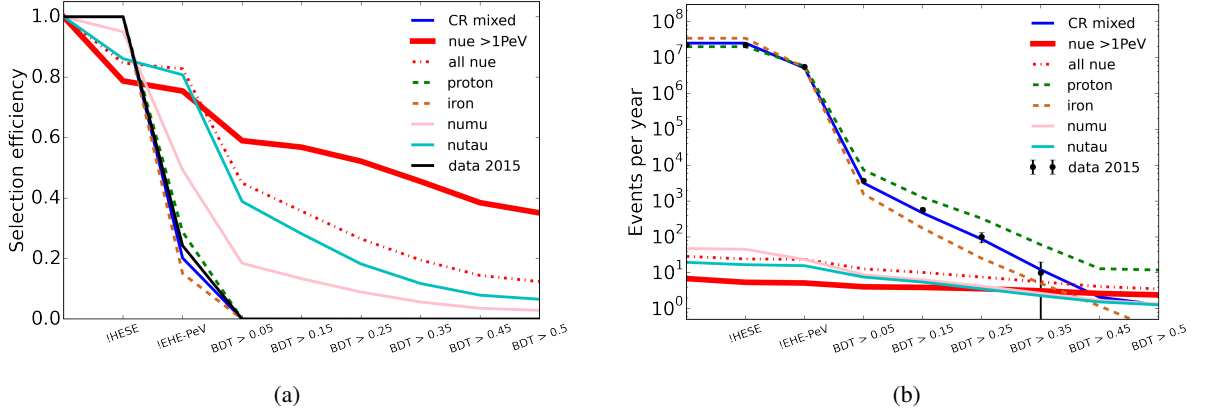


**Figure 2:** Decrease of selection efficiency and event rate due to HESE, EHE-PeV and BDT score requirements. 10% of data took in 2015 is shown in black to compare with simulations. The solid red lines are expectations of electron neutrinos of energy greater than 1 PeV under the assumption of an  $E^{-2}$  spectrum.

with vertex position more than a string-spacing away from the outermost layer of the detector are less bright, harder to be distinguished from background, and more difficult to reconstruct. An illustration of events kept or rejected by the BDT cut is shown in Figure 3.

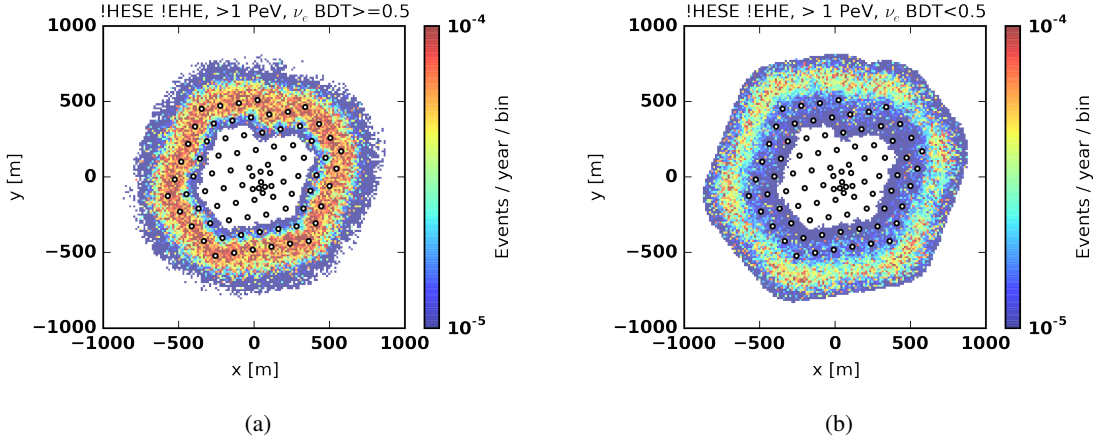


**Figure 3:** (a) X-Y projection for vertex positions of electron neutrinos with energy  $> 1$  PeV and BDT score  $> 0.5$  (b) Vertex positions for electron neutrinos of energy  $> 1$  PeV and BDT score  $< 0.5$ .

For cosmic-ray background, the BDT score is found to be correlated with the fraction of the energy carried by the leading muon over the total energy of all muons reaching IceCube. High-energy muons lose energy stochastically and could register as cascade-like signals when the track travels outside of the detector. Cosmic-rays with BDT score  $> 0.5$  are mostly high-energy leading muons of energy  $\sim$  PeV carrying  $> 90\%$  of the total muon signal in the shower. These rare events are dominantly produced in the air-showers originating from cosmic-ray protons. Simulations were generated via CORSIKA [10] with SIBYLL2.3 [11], charm components have been included. The dominant contribution is from kaons and pions and the charm fraction is less than 10% for leading muons with energies of  $\sim 1$  PeV.



To reconstruct cascade-like events, a point-like Cherenkov light emitter is assumed and the expectations of the number of Cherenkov photons and their arrival times at each DOM is compared to observations or simulated events. Photons from the tracks that comprise the background have worse agreement with such a hypothesis than photons from cascades. This allows further reduction of the background using a goodness-of-fit estimator. The final event selection parameters are optimised for the best data-MC agreement in the background-dominated region and the best signal-background separation in the signal-dominated region, defined by a BDT score  $> 0.5$  and a goodness-of-fit  $< 10$ .

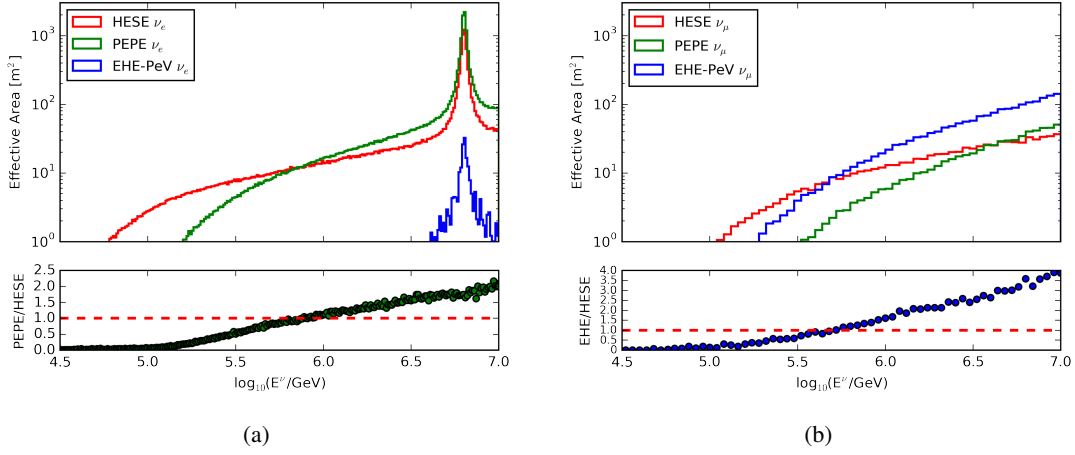


**Figure 4:** Effective area for  $\nu_e$  (a) and  $\nu_\mu$  (b) of HESE, PEPE and EHE-PeV

The effective areas averaged over solid angle of  $\nu_e$  and  $\nu_\mu$  are shown in Figure 4. The PEPE sample surpasses HESE at  $\sim 500$  TeV for detecting electron neutrinos and the gain increases with neutrino energy.

### 3. Event reconstruction of partially-contained cascades

The reconstruction of partially-contained cascades is based on a likelihood fit which maximises the agreement between observation and expectation for the arrival time and intensity of Cherenkov photons assuming a cascade of energy  $E$ , vertex position  $(x,y,z)$ , zenith angle  $\theta$  and azimuth angle  $\phi$ . To understand how well partially-contained cascades can be reconstructed and how well data agrees with simulations, one of the PeV contained cascades detected by IceCube [1] has been selected for a cross-check with simulations. A thousand PeV-cascade events are simulated with vertex positions in a sphere centred at the best-fit value and a radius corresponding to the uncertainty of the vertex position fit. The energy is set to the best-fit energy. For each of the simulated events, the same reconstruction algorithms are applied, and the reconstructed energy and the zenith angle are recorded. Simulations are made using the SpiceLea model for the optical properties of the ice [12], which takes into account the anisotropy of the light propagation and the tilt of the ice layers. The distribution of  $\Delta E/E$ , which is defined as  $(E_{\text{rec}} - E_{\text{MC}})/E_{\text{MC}}$  is shown in Figure 5(b).

In the next step, a wall of strings from the edge of the detector is artificially removed from the reconstruction process for both data and simulations, as illustrated in Figure 5(a). It was found

Config.	removed string count	NPE	$\Delta E/E$ (MC)	$\Delta E/E$ (data)
original	N/A	24830	0.6%	0%
-1 layer	6	24707	0.5%	-0.2%
-2 layers	13	21854	-1.9%	-4.9%
-3 layers	21	8587	30%	25%

**Table 1:** Comparison of the following configurations: the unmodified reconstruction of the measured PeV-event and three modified reconstructions with less layers of strings (see text). The number of photoelectrons (NPE), the difference in reconstructed energy,  $\Delta E/E$  for simulations and data, are given.

that the effect of reconstruction for the real data yields  $(E_{\text{cut1layer}} - E_{\text{nocut}})/E_{\text{nocut}}$  about  $-0.2\%$  and a bias on reconstructed zenith angle of about  $-0.5^\circ$ , which are in good agreement with the simulation.

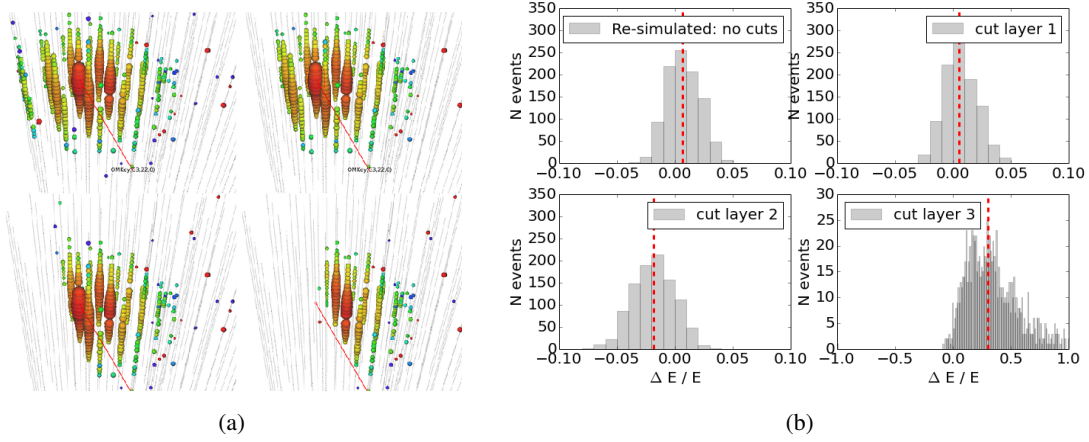


**Figure 5:** (a) Event view of one of the contained PeV events found by IceCube and after one, two and three outer layers of strings have been removed. (b) Reconstruction resolutions of energy for re-simulated PeV events. Each histogram corresponds to 1000 events simulated in one of the scenario in (a) and the dashed lines show the median of each distribution. The reconstructed results from the real data is shown in Table 1.

Further removal of a layer of strings results in  $-5\%$  energy bias and  $+0.35^\circ$  of reconstructed zenith angle for data. With three layers of strings removed, the event is left with 1/3 of total charge, the biases of reconstructed energy and zenith angle are  $+25\%$  and  $+20^\circ$ . All the cases data and simulations agree within allowed uncertainty range. The overestimation of energy in the latter case is due to a wrongly fitted vertex position. The best-fit vertex positions are dragged further outside of the detector, so to compensate the signals the energy of the event needs to be higher. More tests have been carried out such as to remove DOMs on horizontal layers. The same conclusion is reached: when the vertex position is located far outside of the detector and only a fraction of scattered photons are observed, the reconstructed energy can be overestimated. The bias has been observed consistently for both data and simulations. It is planned to do further studies to improve the reconstruction on an event-by-event basis if PeV events are found in the data. For events selected by PEPE, the median error of zenith angle is  $\sim 15^\circ$  and the median error on deposited energy is within 20%.



#### 4. A global fit for a spectral cut-off at PeV energies

A fit of the spectral parameters is performed using a binned Poisson-likelihood method comparing the observed and expected number of events for two bins in zenith angle and five bins per decade in reconstructed energy. Track-like events from the HESE sample are not included in this fit, but only events which can be reconstructed with a single point-like cascade hypothesis are included.

About a factor of two more Glashow resonance events are expected in the PEPE sample when compared to the HESE sample. Similarly the EHE-PeV selection nearly doubles the sensitivity for PeV  $\nu_\mu$  compared to HESE. The combined dataset allows to test the presence of a cut-off and its energy more precisely than with the HESE sample alone. An Asimov-style [13] test has been carried out with the following assumptions: a 1:1:1 flavour mixing ratio,  $\nu_e : \bar{\nu}_e = 1 : 1$  and a neutrino spectrum of  $d\Phi/dE = 2.7 \times (E/100\text{TeV})^{-2.29} e^{-E/2.21\text{PeV}} \times 10^{-18} \text{GeV}^{-1} \text{cm}^{-2} \text{s}^{-1}$ , which is consistent with the best fit result from the global analysis [14]. The profile-likelihood scan on the spectral index  $\gamma$  and the cut-off energy is shown in Figure 6. The contours have been obtained assuming Wilks' theorem applies [15]. No systematic uncertainties are taken into account at this stage.

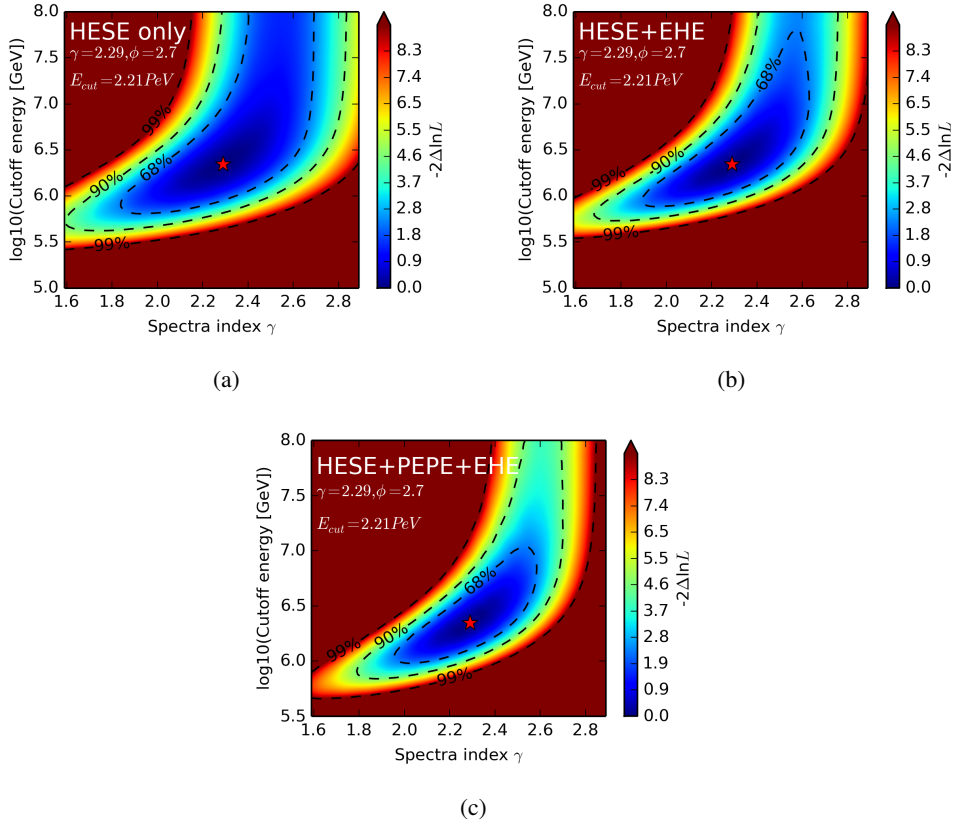


**Figure 6:** Profile likelihood scan on  $\gamma$  and cut-off energy for Asimov test of  $\gamma = -2.29$ , normalisation =  $2.7 \times 10^{-18} \text{GeV}^{-1} \text{cm}^{-2} \text{s}^{-1}$  and  $E_{\text{cut}} = 2.2 \text{ PeV}$  (a) HESE only contour (b) HESE+EHE contour (c) combined HESE+EHE+PEPE.

The prediction of the event rate at the Glashow resonance energy depends greatly on the cut-

off energy. For instance, assuming a hard spectral index  $\gamma = -2.09$ , the number of events expected in 6 years with reconstructed energy above 2.5 PeV ranges from  $\sim 1$  to  $\sim 6$  events when assuming a cut-off energy of 2.2 PeV and 100 PeV, respectively.

## 5. Conclusion and outlook

A new method to search for PeV events using partially-contained cascades has been introduced. It has been optimised to complement the existing search methods. It increases the effective area at the energy of the Glashow resonance by a factor of  $\sim 2$ , where the expected number of events varies strongly depending on the assumption of the spectral shape. Soon 6-years of full data will be unblinded and a global-fit for a cut-off including HESE, EHE-PeV and PEPE samples will be performed. Systematic uncertainties such as the optical properties of ice and hadronic interaction models for atmospheric muon production will be included.

## References

- [1] **IceCube** Collaboration, M. G. Aartsen *et al.*, *Phys. Rev. Lett.* **111** (2013) 021103
- [2] **IceCube** Collaboration, M. G. Aartsen *et al.*, *Science* **342** (2013) 1242856
- [3] **IceCube** Collaboration, M. G. Aartsen *et al.*, *Phys. Rev. Lett.* **113** (2014) 101101
- [4] **IceCube** Collaboration, M. G. Aartsen *et al.*, *Astrophys.J.* **833** (2016) 3
- [5] S. L. Glashow, *Phys. Rev.* **118** (1960) 316
- [6] V. Barger *et al.*, *Phys. Rev. D* **90** (2014) 121301
- [7] **IceCube** Collaboration, M. G. Aartsen *et al.*, *Astropart. Phys.* **92** (2017) 30
- [8] **IceCube** Collaboration, M. G. Aartsen *et al.*, *PoS(ICRC2015)* **1109** (2016)
- [9] Y. Freund and R. E. Schapir, *J. Comput. Syst. Sci.* **55** (1997) 1-119-139
- [10] D. Heck *et al.*, *Technical Report*, Forschungszentrum Karlsruhe GmbH **6019** (1998)
- [11] F. Riehn *et al.*, *PoS(ICRC2015)* **558** (2016)
- [12] **IceCube** Collaboration, M. G. Aartsen *et al.*, *Proceedings of ICRC2013* **0580** (2014)
- [13] G. Cowan *et al.*, *Eur.Phys.J.* **C71** (2001) 1554
- [14] **IceCube** Collaboration, M. G. Aartsen *et al.*, *PoS(ICRC2015)* **1066** (2016)
- [15] S. S. Wilks, *Ann. Math. Statist.* **9** (1938) 1-60-62

# High Energy Astrophysical Neutrino Flux Measurement Using Neutrino-induced Cascades Observed in 4 Years of IceCube Data

---

## The IceCube Collaboration<sup>†</sup>

<sup>†</sup> [http://icecube.wisc.edu/collaboration/authors/icrc17\\_icecube](http://icecube.wisc.edu/collaboration/authors/icrc17_icecube)

E-mail: [hans.niederhausen@stonybrook.edu](mailto:hans.niederhausen@stonybrook.edu), [yiqian.xu@stonybrook.edu](mailto:yiqian.xu@stonybrook.edu)

We report a new measurement of the diffuse flux of high energy extraterrestrial neutrinos from the entire sky with energies of O(1 TeV) and above. We have analyzed four years of IceCube data recorded from 2012-2015 focusing on neutrino-induced particle showers. These cascades stem predominantly from electron and tau neutrino interactions, provide good deposited energy resolution and have a lower rate of atmospheric production than muon neutrinos. A new event selection has been developed combining traditional straight cuts with gradient boosted multi-class decision trees to isolate cascades more efficiently, resulting in the largest cascade sample obtained by IceCube to date. The observed astrophysical component dominates at energies above 20 TeV and is well described by a single, unbroken power-law. The preliminary fit result is a spectral index of  $\gamma = 2.48 \pm 0.08$  with a per-flavor normalization at 100 TeV of  $\phi = (1.57_{-0.22}^{+0.23}) \cdot 10^{-18} \text{ GeV}^{-1} \text{ s}^{-1} \text{ sr}^{-1} \text{ cm}^{-2}$  in agreement with previous IceCube measurements. We investigated the possibility of a spectral hardening at the upper end of the spectrum by allowing a second power-law component to enter our flux model. No evidence for such hardening has been found. In the near future we expect improved results by adding IceCube's existing cascades from the preceding two years (2010-2011) into this analysis thereby enlarging the total live time to six years.

**Corresponding authors:** Hans Niederhausen<sup>\*1</sup>, Yiqian Xu<sup>1</sup>

<sup>1</sup> *Department of Physics and Astronomy, Stony Brook University, Stony Brook, NY 11794-3800*

*35th International Cosmic Ray Conference — ICRC2017  
10–20 July, 2017  
Bexco, Busan, Korea*

---

<sup>\*</sup>Speaker.

## 1. Introduction

IceCube [1] is a cubic-kilometer neutrino detector installed in the glacial ice at the geographic South Pole between depths of 1450 m and 2450 m. IceCube observes neutrinos based on optical measurements of Cherenkov radiation emitted by secondary particles produced in neutrino interactions. Those interaction are dominated by deep-inelastic scattering (DIS) between neutrinos and nucleons in the ice. Events can be distinguished by the pattern of their light deposition mainly into tracks and cascades. Tracks arise primarily from through-going or starting muons while cascades can be produced by charged-current interactions of  $\nu_e$  and  $\nu_\tau$  and by neutral current interactions of any flavor. Most particles triggering IceCube are atmospheric muons produced in cosmic ray induced air showers. The same air showers also generate atmospheric neutrinos. In addition IceCube reported the discovery of high energy neutrinos of extraterrestrial origin [2][3]. Their production is assumed to be associated with particle acceleration at cosmic ray sources. Based on diffusive shock acceleration and neutrino oscillations during propagation one expects the flux to exhibit a power-law spectrum  $E^{-\gamma}$  [4][5] with an approximately equal flavor admixture at earth ( $\nu_e : \nu_\mu : \nu_\tau \approx 1 : 1 : 1$ ) [6]. Several IceCube analyses have measured the spectrum of astrophysical neutrinos [3][7][8][9]. The observed spectral indices range from  $\gamma \sim 2.2$  when muon neutrinos from the Northern Sky are considered, observing astrophysical neutrinos above 119 TeV, to  $\gamma \sim 2.7$  when cascades are studied with sensitivity primarily to electron and tau neutrinos from the entire sky in the several O(10 TeV) energy range. Compared to the track channel, the cascade channel benefits from smaller atmospheric background levels as well as from a superior (deposited) energy resolution of  $\sim 15\%$  ( $E > 10$  TeV). We present new results concerning the spectral behavior of the astrophysical neutrino flux using cascade events observed in four years of IceCube data recorded from 2012-2015. In the future this dataset will be combined with the cascades presented in the previous analysis [9], subsequently referred to as “2yr-cascades”.

## 2. Event Selection

The event selection we present in this paper improves over the 2yr-cascade analysis by enhancing the cascade signal efficiency ( $> 20\%$  for reconstructed energies  $E_{\text{rec}} > 60$  TeV) and lowering the energy threshold from  $E_{\text{rec}} = 10$  TeV down to O(1 TeV) thus reducing systematic uncertainties. The selection criteria were determined by comparing Monte-Carlo simulations for signal and background contributions. The simulations were generated using the same software packages as in the previous work [9], most notably full air shower simulation (CORSIKA) to model cosmic-ray induced muon background. The events that are most difficult to identify as background are single muons that deposit most of their energy in a single cascade like energy loss, thus mimicking a cascade like signature. Following ref. [8] we now rely on a parametrization of the single muon yield derived from CORSIKA [10] to more efficiently predict this background. While the modeling of the conventional atmospheric neutrino component remains unchanged [9] (HKKMS06 [11] with modifications [12]) we altered the prediction for prompt atmospheric neutrinos [13] following the updated calculation described in [14] by the same authors. At high energies ( $E_{\text{rec}} \geq 60$  TeV) we isolate cascade events using straight cuts based on the topology variables described in the previous analysis [9][15] or slight modifications thereof. Cut values were chosen to maximize signal efficiency while suppressing the atmospheric muon background expectation to zero. At lower energies a gradient boosted multi-class decision trees classifier [16] is used to suppress atmospheric muon background and separate the remaining events according to their topology into cascades and starting tracks with the latter being dominated by conventional

atmospheric neutrinos. Each event is assigned three scores: muon score, hybrid score and cascade score measuring the compatibility of the event with a muon, starting track or cascade topology, respectively. Figure 1 (left) shows for one year the deposited energy distribution of events passing all selection criteria of the high energy selection except the final  $E_{\text{rec}} > 60 \text{ TeV}$  cut for one year of data. Also shown is the BDT's cascade score distribution used to define the cascade signal region (center). The simulations agree well with the observed data. The final low (high) energy selection achieves a neutrino purity of  $> 90\%$  ( $100\%$ ). Figure 1 (right) shows the effective areas of the cascade sample for the three different neutrino flavors after combining the low and high energy selections and demonstrates sensitivity primarily to electron and tau flavors. In total 19 events were found with reconstructed energies above  $100 \text{ TeV}$ . The highest energy cascade previously not reported by IceCube, is located at a depth with shorter than average absorption length due to high concentration of dust particles in the ice and has been reconstructed with an energy deposit of  $2 \text{ PeV}$ . Further studies using improved estimates of the absorption length at these depths resulted in a lower, more realistic reconstructed energy of  $800 \text{ TeV}$ . The corresponding systematic uncertainties are still under evaluation.

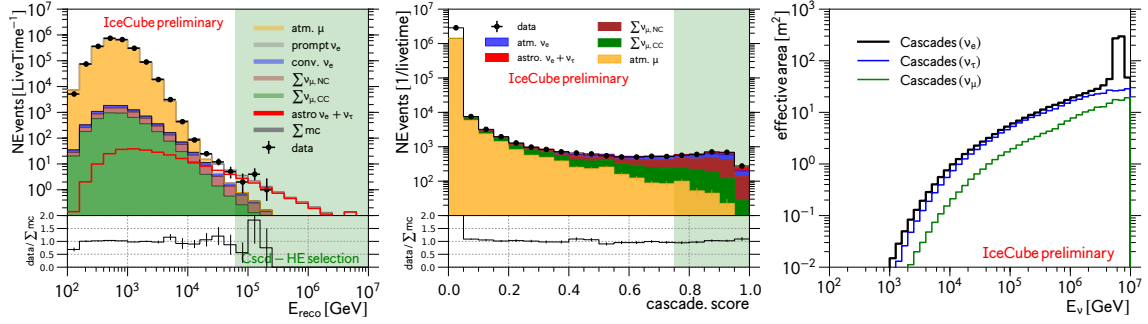


Figure 1: Deposited energy of high energy selection before final energy cut for the year 2015 (left); Distribution of cascade.score (BDT variable) used in low energy selection (center). Signal regions are marked as green shaded bands. Effective areas of the combined cascade samples (low energy  $\cup$  high energy) (right).

### 3. Analysis Method

The measurement of the astrophysical neutrino spectrum is performed by matching the reconstructed energy distribution to the simulation prediction by numerically maximizing a binned poisson likelihood. Similarly, approximate  $100(1 - \alpha)\%$  confidence regions are obtained using the profile-likelihood method in conjunction with Wilks' theorem, as in ref. [9]. If prior information about the parameters of interest is available, we use a Bayesian method and calculate  $100(1 - \alpha)\%$  highest posterior density (HPD) credible regions  $C$  [17] defined by

$$C = \{\theta \in \Theta : \pi(\theta|x) \geq k(\alpha)\} \quad (1)$$

$$1 - \alpha \leq P(C|x) = \int_C \pi(\theta|x) d\theta = \int_C f(x|\theta) \cdot \pi(\theta) d\theta \quad (2)$$

where  $k(\alpha)$  is the largest constant satisfying Eq. (2).  $\pi(\theta)$ ,  $\pi(\theta|x)$  and  $f(x|\theta) \propto L(\theta|x)$  are prior distribution, posterior distribution and likelihood function respectively. The same formalism allows us to check predictions from previous IceCube measurements for any observable quantity  $z$  using

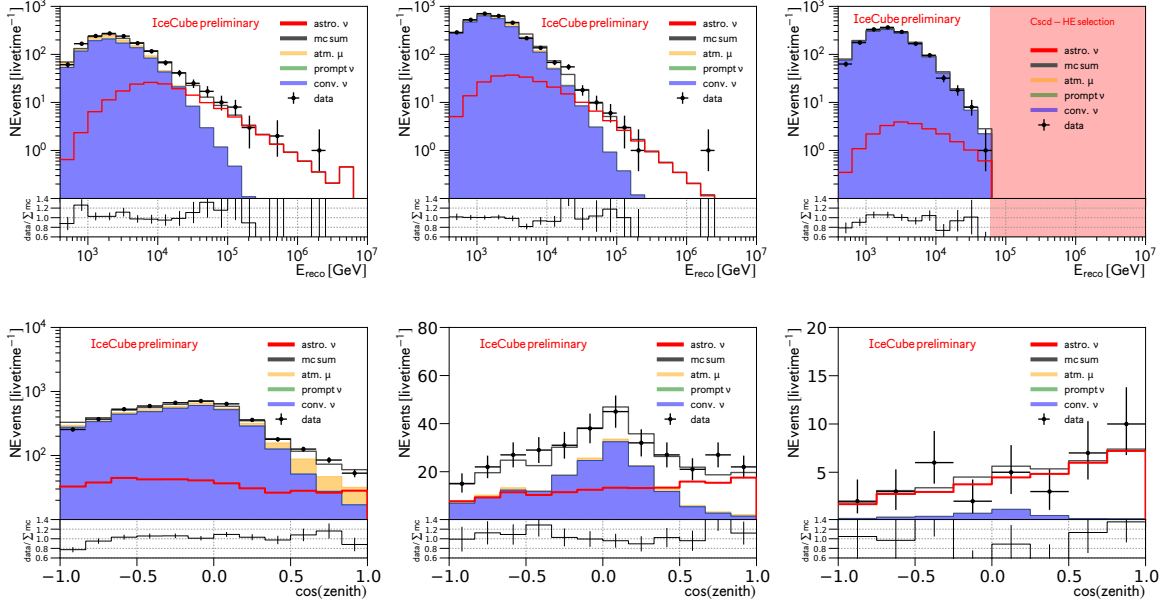


Figure 2: Best fit distributions assuming single power-law model. Top: Energy distributions for cascades (left: Southern sky, center: Northern sky) and starting tracks (right: entire sky). The starting track sample only covers energies up to  $E = 60$  TeV (red band). Bottom: Cascade zenith distributions for all energies (left),  $E > 10$  TeV (center) and  $E > 60$  TeV (right).

predictive densities  $p(z|y)$  [17], where  $y$  refers to data observed in the previous measurement:

$$p(z|y) = \int_{\Theta} g(z|\theta) \pi(\theta|y) d\theta. \quad (3)$$

Tail area probabilities are then defined as  $P(z \geq z_{obs}|y)$  [18], where  $z_{obs}$  is the observed value of  $z$  in this sample and can be obtained from the predictive density  $p(z|y)$  by integration.

We separate the cascade events according to their reconstructed zenith angle  $\Theta_{rec}$  into two groups: 'Northern Sky' ( $\cos \Theta_{rec} < 0$ ) and 'Southern Sky' ( $\cos \Theta_{rec} \geq 0$ ). Neutrinos classified as starting tracks from the whole sky form the third group, a  $\nu_{\mu}$ -CC control group ( $E_{rec} < 60$  TeV). Finally, we require the total sum of predicted events below the cuts ( $E_{rec} < 60$  TeV) to match the total number of observed events in that region (down to  $\text{cascade.score}=0.1$ , see Fig. 1) within uncertainties. Sources of systematic uncertainties remain the same as before and are discussed in more detail in ref. [9]. We revised the treatment and implementation of detector related systematic uncertainties (scattering and absorption of photons in the ice, optical efficiency of the DOMs to photons) into our likelihood function to describe the sensitivity of this analysis to these effects at lower energies ( $E_{rec} < 10$  TeV). Each effect is now treated separately and contributes a nuisance parameter to the fit that adjusts the nominal simulation prediction in each bin by independent, multiplicative efficiency corrections. The relationship between the size of the effect, i.e. the value of the nuisance parameter, and the efficiency correction is treated as linear and has been determined from dedicated simulations. This is done separately for each flux component and each histogram bin.

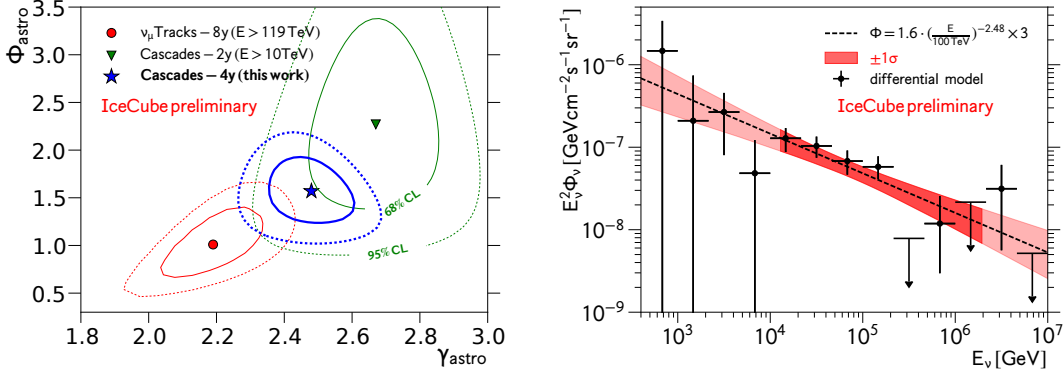


Figure 3: Left: Profile likelihood contours for single power-law parameters; this work (blue), 2-yr cascades (green) and 8-yr diffuse  $\nu_\mu$  (red). Right: Best fit of differential flux model (see text), summed over all three  $\nu$ -flavors assuming  $(\nu_e : \nu_\mu : \nu_\tau) = (1 : 1 : 1)$ . The sensitive energy range (see text) is highlighted in red.

Parameter		Prior	Result
<b>spectral index</b>	$\gamma$	-	<b><math>2.48 \pm 0.08</math></b>
<b>norm astro</b>	$\phi$	-	<b><math>(1.57^{+0.23}_{-0.22})</math> c.u.</b>
norm conv	$\phi_{conv}$	$1.00 \pm 0.30$	$(1.12 \pm 0.10) \cdot \Phi_{HKMS06}$
norm prompt	$\phi_{prompt}$	$0.0^{+1.8}_{-0.0} \cdot \Phi_{BERSS}$	$< X \cdot \Phi_{BERSS}^{(**)}$
norm muon	$\phi_{muon}$	-	$1.40 \pm 0.04$
scattering scale	$\epsilon_{scat}$	$1.00 \pm 0.10^{(*)}$	$1.07 \pm 0.02$
absorption scale	$\epsilon_{abs}$	$1.00 \pm 0.10^{(*)}$	$0.99 \pm 0.03$
dom efficiency	$\epsilon_{eff}$	$0.99 \pm 0.10$	$1.00 \pm 0.06$

Table 1: Single power-law fit results. (1 c.u.  $\equiv 10^{-18} \text{ GeV}^{-1} \text{ s}^{-1} \text{ sr}^{-1} \text{ cm}^{-2}$ ). (\*) This prior uses a bi-variate normal distribution to account for anti-correlation. (\*\*) This upper limit is still under evaluation.

## 4. Results

### 4.1 The Single Power-Law

In this section we assume the astrophysical neutrino flux to follow a single, isotropic, unbroken power-law with equal contributions from all flavors:

$$\Phi_\nu = \phi \times (E_\nu/100 \text{ TeV})^{-\gamma}. \quad (4)$$

with per-flavor normalization  $\phi$  at  $E_\nu = 100 \text{ TeV}$  and spectral index  $\gamma$ . The best-fit flux parameters are  $\phi = (1.57^{+0.23}_{-0.22}) \cdot 10^{-18} \text{ GeV}^{-1} \text{ s}^{-1} \text{ sr}^{-1} \text{ cm}^{-2}$  and  $\gamma = 2.48 \pm 0.08$ . The best-fit values and uncertainties of all other fit parameters can be found in Tab. 1. The flux is measured above the conventional neutrino background in the energy range [7] from 12 TeV to 2.1 PeV. Figure 2 shows good agreement between the corresponding reconstructed energy and zenith distributions predicted from our Monte-Carlo simulations and the observed data. The 68% confidence region (blue) for the astrophysical parameters is shown in Fig. 3 (left) and compared to the result of the previous analysis [9] using 2 years of IceCube data with reconstructed energies larger than 10 TeV (green). Both measurements agree well within uncertainties. Also shown is the result of the most recent IceCube measurement, using muon neutrinos from the Northern Sky, that observed astrophysical neutrinos above  $E_\nu = 119 \text{ TeV}$  (red) [7]. Both measurements are consistent only at the  $p = 0.04$  level as estimated from the two contours. Finally we obtain better constraints on the systematic



uncertainties compared to the 2-year cascades due to the large number of events at low energies ( $E_{\text{rec}} < 10\text{TeV}$ ), which translates into reduced uncertainties especially in the measurement of the astrophysical normalization.

#### 4.2 The Differential Model

While the single power-law appears to be an adequate description of this cascade dataset, we explored a semi-parametric alternative model, the ‘‘differential model‘‘, used in previous IceCube analyses [3][8][9]. See ref. [9] for details. The fit result (black) is shown in Fig. 3 (right) and compares well to the parametric single power-law fit (red). Large uncertainties are observed at low energies  $E_\nu < 10\text{TeV}$ , where conventional background dominates the spectrum, as well as at highest energies  $E_\nu > 200\text{TeV}$ , where only six events were found.

#### 4.3 The High Energy Tail ( $E > 200\text{TeV}$ )

At energies above  $200\text{TeV}$  we expect essentially no atmospheric background in this sample. Figure 4 (left) shows the likelihood function for a restricted high energy  $E_{\text{rec}} > 200\text{TeV}$  fit with all nuisance parameters fixed to their nominal values. Also shown are the results of previous measurements, the 2-year cascades [9] (black) and the 8-year tracks [7] (white). The six high energy events do not provide sufficient information to distinguish between the two past results and appear consistent with both. The highest energy cascade has a deposited energy of  $2\text{PeV}$  and was reported by IceCube before [3]. We studied the compatibility of this observation with predictions from the 2-year cascades [9] and the 8-year tracks [7], by calculating the predictive distributions (Eq. 3) for the maximum cascade energy to be observed in this sample. The result is shown in Fig. 4 (center). Observing a highest energy cascade with a deposited energy of  $2\text{PeV}$  or less is possible for both assumptions:  $P(E_{\text{max}} \leq 2\text{PeV}|y) = 0.40$  with  $y \equiv 2\text{-year cascades}$  ( $0.09$  with  $y \equiv 8\text{-year tracks}$ ). Finally observing only six events or less in total, while interpreted as under-fluctuation, is plausible for both previous results with predicted probabilities of  $P(N_{\text{events}} \leq 6|y) = 0.14$  with  $y \equiv 2\text{-year cascades}$  ( $0.05$  with  $y \equiv 8\text{-year tracks}$ ).

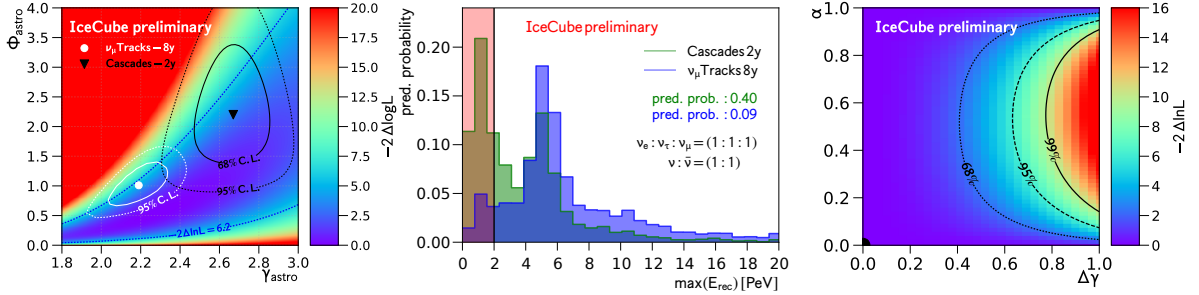


Figure 4: Left: Likelihood function of single power-law model for  $E_{\text{rec}} > 200\text{TeV}$ ; also shown: 2-year cascades (black) and 8-year diffuse  $\nu_\mu$  (white) results. Center: Predicted distribution of maximum observed energy (see text) assuming an unbroken power-law. Right: Profile likelihood scan of parameters describing a possible second power-law component (see text).

#### 4.4 The 2-Component Power-Law

Motivated by the 8-year track measurement observing a harder spectrum at energies above  $E_\nu = 119\text{TeV}$  we studied the possibility of a spectral hardening by adding a second power-law component to the astrophysical neutrino flux model:

$$\Phi(E_\nu) = \Phi_0 \times 10^{-18} \left\{ (1 - \alpha) \left[ \frac{E_\nu}{10^5 \text{GeV}} \right]^{-\gamma_{\text{soft}}} + \alpha \left[ \frac{E_\nu}{10^5 \text{GeV}} \right]^{-\gamma_{\text{soft}} + \Delta\gamma} \right\} \quad (5)$$



with  $0 < \alpha < 1$ ,  $\Delta\gamma \geq 0$ .  $\alpha$  denotes the mixture fraction, the fraction of the total flux at  $E_\nu = 100\text{TeV}$  contributed by the harder of the two components.  $\Delta\gamma$  describes the amount of spectral hardening. The maximum likelihood best-fit values for the new parameters are  $\alpha \rightarrow 0.0$  and  $\Delta\gamma = 0.0$  such that we find no evidence for the existence of a second component. The fit reduces this model to the single power-law. Figure 5 visualizes the profile-likelihood function for the parameters  $\alpha$  and  $\Delta\gamma$ . The constraints on the parameter  $\Delta\gamma$  depend on the mixture fraction  $\alpha$ . The strongest limits are obtained if both components were to contribute equally to the flux at  $E_\nu = 100\text{TeV}$ . In order to interpret this result in the context of the 8y-track measurement, we separately calculate HPD regions for the pairs  $\gamma_{\text{soft}}, \phi_{\text{soft}} = (1 - \alpha)\phi$  and  $\gamma_{\text{hard}} = \gamma_{\text{soft}} - \Delta\gamma, \phi_{\text{hard}} = \alpha \cdot \phi$  using Eq. (2), first assuming uniform prior distributions for all four parameters in Eq. (5). Figure 5 (top) shows the resulting contours for the hard (left) and soft (right) components. In this scenario the constraints on the hard component overlap with the 8-year tracks result (red). It is difficult to constrain both components simultaneously using this sample alone due to a strong anti-correlation between the normalization parameters of both components in absence of evidence for spectral hardening in the likelihood. An improved estimate can be obtained by directly interpreting the track result as prior pdf for the hard component, while keeping the identifiability constraint  $\gamma_{\text{hard}} \leq \gamma_{\text{soft}}$  ( $\Delta\gamma \geq 0$ ) as before. The corresponding HPD regions are shown in Fig. 5 (bottom). The posterior pdf for the hard component (blue) shows substantial overlap with the prior distribution (red) and no strong pull

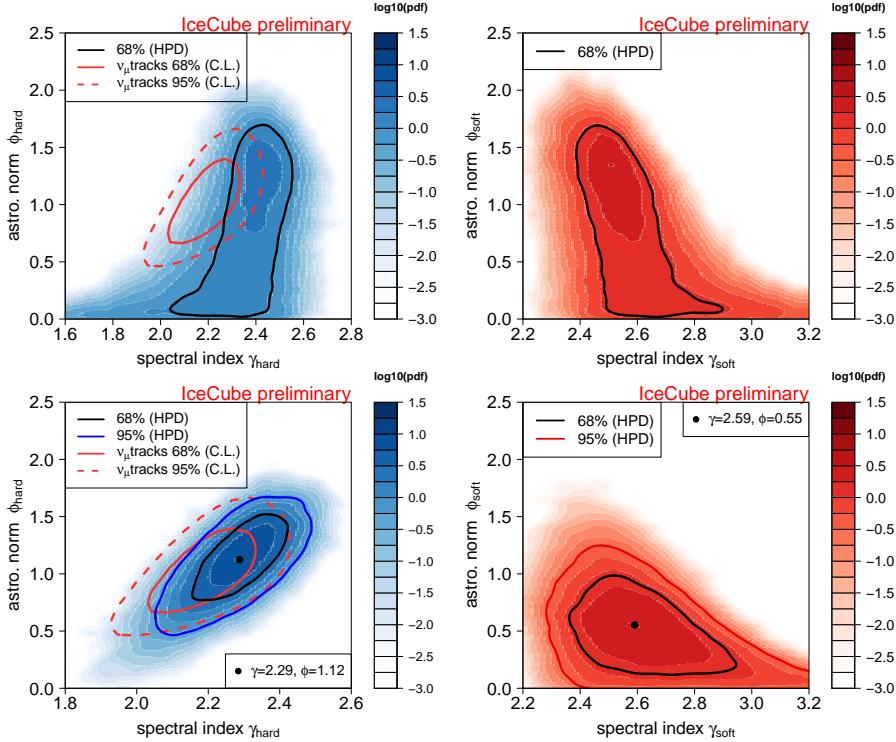


Figure 5: Posterior densities for hard (left) and soft (right) components for different choices of prior distributions (see text): uniform prior distributions (top) and using the result of the 8-year track measurement [7] as prior distribution for the hard component (bottom). Detector related sys. uncertainties are not included.

is observed. In conclusion, while not preferred, the existence of a harder second flux component with properties given by the 8-year track measurement would be consistent with this dataset.

## 5. Summary

We have performed a new measurement of the high energy astrophysical neutrino flux using neutrino induced cascades observed by IceCube in a four year period (2012-2015). According to this analysis the astrophysical component is expected to dominate the observed energy spectrum at energies above 20 TeV and appears well described by a single, unbroken power-law. The preliminary fit result is a spectral index of  $\gamma = 2.48 \pm 0.08$  with a per-flavor normalization at  $E_\nu = 100 \text{ TeV}$  of  $\Phi = (1.57_{-0.22}^{+0.23}) \cdot 10^{-18} \text{ GeV}^{-1} \text{ s}^{-1} \text{ sr}^{-1} \text{ cm}^{-2}$  in agreement with previous IceCube analyses. We investigated the possibility of a spectral hardening of the neutrino flux at highest energies as indicated by a recent analysis of muon neutrinos from the Northern Sky by allowing a second power-law component to enter the flux model. While no evidence for the existence of such a component was found, our results do not exclude it either. We further showed that the highest energy events ( $E_{\text{rec}} > 200 \text{ TeV}$ ) observed in this sample, while being highly informative about the existence of high energy astrophysical neutrinos, due to their small numbers do not provide strong constraints on the spectral behavior of this flux and leave room for interpretation. In the near future we expect improved results from combining this dataset with cascades from the preceding two years as well as from an upcoming fit to all IceCube detection channels [19].

## References

- [1] **IceCube** Collaboration, M. G. Aartsen et al., JINST 12 (2017), P03012
- [2] **IceCube** Collaboration, M. G. Aartsen et al., Science 342, 1242856 (2013)
- [3] **IceCube** Collaboration, M. G. Aartsen et al., Phys. Rev. Lett. 113, 101101 (2014)
- [4] T. K. Gaisser, F. Halzen, and T. Stanev, Physics Reports 258, 173 (1995)
- [5] E. Waxman and J. Bahcall, Phys. Rev. Lett. 78, 2292 (1997); K. Murase, S. Inoue, and S. Nagataki, Astrophys. J 689, L105 (2008); F. W. Stecker, Phys. Rev. D 88, 047301 (2013)
- [6] H. Athar, M. Jezabek and O. Yasuda, Phys. Rev. D 62, 103007 (2000)
- [7] **IceCube** Collaboration, [PoS \(ICRC2017\) 1005](#) (these proceedings)
- [8] **IceCube** Collaboration, M. G. Aartsen et al., Phys. Rev. D 91, 022001 (2015)
- [9] **IceCube** Collaboration, [PoS \(ICRC2015\) 1099](#) (2015)
- [10] D. Heck et al., *CORSIKA*, Tech. Rep. FZKA 6019, Forschungszentrum Karlsruhe (1998)
- [11] M. Honda et al., Phys. Rev. D 75, 043006 (2007)
- [12] M. G. Aartsen et al., Phys. Rev. D 89, 062007 (2014)
- [13] R. Enberg, M. H. Reno and I. Sarcevic, Phys. Rev. D 78, 043005 (2008)
- [14] A. Bhattacharya et al., JHEP 06, 110 (2015)
- [15] **IceCube** Collaboration, Proceedings of the 33rd ICRC, paper 0370 (2013)
- [16] T. Chen and C. Guestrin, Proceedings of the 22nd KDD (2016), arXiv:1603.02754
- [17] J. O. Berger, "Statistical Decision Theory and Bayesian Analysis", Springer, 2nd ed. (1993)
- [18] A. Gelman et al., "Bayesian Data Analysis", Chapman and Hall/CRC, 3rd ed. (2013)
- [19] **IceCube** Collaboration, [PoS \(ICRC2017\) 976](#) (these proceedings)

# A Measurement of the Diffuse Astrophysical Muon Neutrino Flux Using Eight Years of IceCube Data

---

## The IceCube Collaboration<sup>†</sup>

<sup>†</sup> [http://icecube.wisc.edu/collaboration/authors/icrc17\\_icecube](http://icecube.wisc.edu/collaboration/authors/icrc17_icecube)

E-mail: [haack@physik.rwth-aachen.de](mailto:haack@physik.rwth-aachen.de),  
[wiebusch@physik.rwth-aachen.de](mailto:wiebusch@physik.rwth-aachen.de)

Recently the IceCube collaboration confirmed the astrophysical neutrino flux in the muon neutrino channel with high significance using six years of data. This analysis used a likelihood approach with reconstructed muon energy and zenith angle as observables to measure the properties of the astrophysical muon neutrino flux. Additionally constraints on the prompt atmospheric neutrino flux from the decay of charmed mesons were obtained. In this contribution we will present an update to this analysis using eight years of data collected from 2009 through 2017, containing about 500,000 muon neutrino candidates with a negligible contribution of atmospheric muons.

**Corresponding authors:** C. Haack<sup>\*1</sup>, C. Wiebusch<sup>1</sup>

<sup>1</sup> *III. Physikalisches Institut, RWTH Aachen University*

*35th International Cosmic Ray Conference (ICRC2017)  
10-20 July, 2017  
Bexco, Busan, Korea*

---

<sup>\*</sup>Speaker.

## 1. Introduction

The detection and use of high-energy astrophysical neutrinos as cosmic messengers has been an outstanding goal in the field of astroparticle physics. In 2013 the IceCube neutrino observatory [1] reported the first evidence for the existence of a diffuse flux of extraterrestrial neutrinos at high energies [2, 3]. The discovery was based on neutrinos of all flavors above a few 10 TeV that interact within the detector volume (starting events). Shortly after, this signal was confirmed by a complementary measurement utilizing through-going and starting muons from charged-current muon neutrino nucleon interactions close to the detector volume [4, 5]. Both measurements showed a clear excess of high-energy events, that cannot be explained by atmospheric neutrino or muon backgrounds.

The most recent published analysis of through-going muons [5] is based on six years of data, collected from 2009 to 2015. The measurement benefits from the large effective volume and the good directional resolution of track-like events but has a restricted field of view to the Northern hemisphere. Main backgrounds are atmospheric neutrinos and atmospheric muons produced by cosmic ray interactions in Earth's atmosphere. By selecting well reconstructed muon tracks originating from and below the horizon, atmospheric muons can be rejected efficiently. This has resulted in a high-statistics neutrino sample of about 350,000 neutrino events with a purity of 99.7%. Most events are atmospheric neutrinos originating from pion and kaon decays (*conventional atmospheric*). A sub-dominant contribution of events from the decay of charmed mesons (*prompt atmospheric*) is expected. The sensitive energy range above which an extraterrestrial neutrino flux can be detected is about 200 TeV. This is larger than for starting event analysis [6], because of a larger background flux of atmospheric muon neutrino and a poorer energy resolution for uncontained through-going muon events. An evident flux of extraterrestrial neutrinos extending up to several PeV has been observed, including the highest-energy neutrino reported to date, with a median inferred neutrino energy of 7.8 PeV. The flux is well described by an isotropic, unbroken power law  $E^{-\gamma}$ .

Here, we update this analysis to eight years of collected data up to May 10<sup>th</sup> 2017. This corresponds to a sample of almost a half million neutrino events including almost 1000 extraterrestrial neutrinos as estimated by our best fit.

## 2. The IceCube Neutrino Observatory

The IceCube Neutrino Observatory is a cubic-kilometer sized Cherenkov detector embedded in the Antarctic ice at the South Pole [1]. It detects neutrinos by observing Cherenkov radiation emitted by charged secondary particles that are created by neutrino interactions in the ice. A total of 5160 optical sensors instrument 86 cable strings at depths between 1450m and 2450m beneath the surface resulting in an active volume of about one cubic kilometer.

IceCube was completed in December 2010, but it had already been taking data in the years before with the partially completed detector. The analysis presented here uses data from May 2009 to May 2017, taken with the 59-string configuration in the first year, the 79-string configuration in the second year and the 86-string configuration of the completed detector afterwards. The event

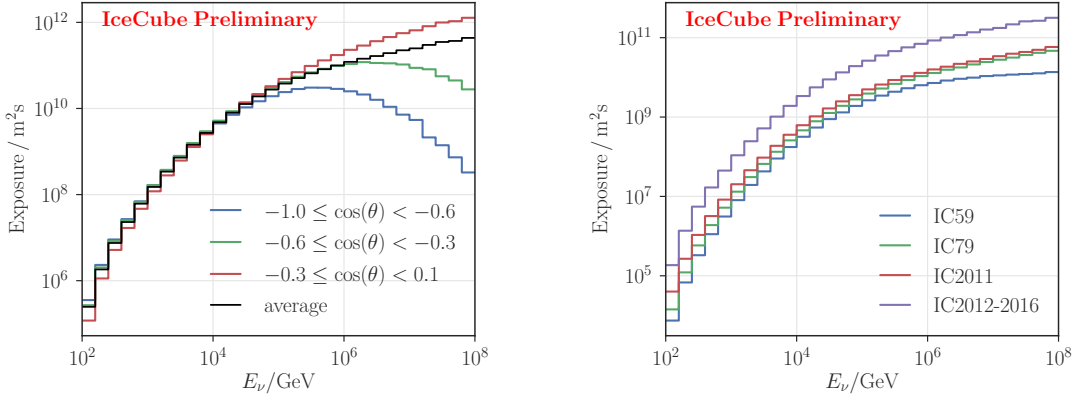


Figure 1 Exposure of the analysis, summed for neutrinos and anti-neutrinos. Left: Averaged exposure for different zenith ranges. Right: Exposure integrated over the field of view for the different detector configurations.

selection for the newly added data is unchanged with respect to [5]. The updated total integrated exposure of the analysis is shown in figure 1.

### 3. Analysis Method

#### 3.1 Flux Models

We include the contribution of three sources of neutrinos in this analysis: Conventional atmospheric neutrinos from the decay of pions and kaons, prompt atmospheric neutrinos from the decay of charmed mesons, and isotropic diffuse astrophysical neutrinos. The conventional neutrino flux is modeled by the prediction of [7], modified to include the effect of different cosmic ray flux models [8, 9] and the cosmic-ray knee [10]. The prompt neutrino flux is modeled by the ERS model [11] with a free normalization. The astrophysical neutrino flux is modeled as an isotropic power-law flux:

$$\frac{d\Phi}{dE} = \Phi_0 \cdot \left( \frac{E_\nu}{100 \text{ TeV}} \right)^{-\gamma_{astro}} \quad (3.1)$$

#### 3.2 Likelihood Description

The analysis is based on comparing the expected flux contributions obtained from Monte-Carlo simulation to experimental data. Thus, the data are binned in two observables: estimated muon energy and reconstructed muon zenith angle. The expectation in each bin of the resulting histograms can be modeled by a modified Poisson likelihood  $L_i$ , which takes into account the limited statistics of the Monte-Carlo simulation [12] as described in [5].

The bin-wise expectation  $\mu_i$  is defined as:

$$\mu_i(\theta, \xi) = \mu_i^{conv.}(\xi) + \mu_i^{prompt}(\Phi_{prompt}, \xi) + \mu_i^{astro}(\Phi_{astro}, \gamma_{astro}, \xi_{det.}), \quad (3.2)$$

where  $\theta$  denotes the signal flux parameters  $\Phi_{astro}, \gamma_{astro}, \Phi_{prompt}$  and  $\xi = \{\xi_{theo.}; \xi_{det.}\}$  denotes the nuisance parameters. The nuisance parameters incorporate systematic uncertainties into the

likelihood function. Systematic uncertainties include uncertainties in theoretical model predictions ( $\xi_{theo.}$ ) and detector effects ( $\xi_{det.}$ ) and are parametrized continuously. A detailed description of the uncertainties and their technical implementation can be found in [5]. The total likelihood is obtained as  $L = \prod_i L_i$ . The best-fit signal and nuisance parameters are obtained by maximizing the total likelihood function. The parameter uncertainties are obtained using the profile-likelihood technique and applying Wilks' theorem [13]. The applicability of Wilks' theorem has been verified using ensemble tests.

### 3.3 Parametric Unfolding

The observed neutrino energy spectrum can be unfolded from the observed experimental events using the posterior probability density function (PDF)  $P(E_\nu|E_{reco}^i)$ , where  $E_{reco}^i$  is the muon energy proxy of event  $i$ . The posterior PDF is constructed by inverting the resolution functions  $P(E_{reco}^i|E_\nu)$  as described in [5]. This procedure, however, depends on the prior assumed for the neutrino energy spectrum, for which we use the best-fit value of this analysis.

## 4. Results

### 4.1 Updated Fit Results

The best fit to the full data-set results in an astrophysical powerlaw flux is given as:

$$\frac{d\Phi_{\nu+\bar{\nu}}}{dE} = (1.01 \pm_{0.23}^{0.26}) \left( \frac{E}{100 \text{ TeV}} \right)^{-2.19 \pm 0.10} \cdot 10^{-18} \text{ GeV}^{-1} \text{ cm}^{-2} \text{ s}^{-1} \text{ sr}^{-1}. \quad (4.1)$$

This result is consistent with the previous result, that was based on six years of data but improves the accuracy. The significance of the astrophysical flux with respect to the atmospheric only hypothesis is increased from  $5.6 \sigma$  to  $6.7 \sigma$ . The central range of neutrino energies that contribute 90% to the total observed likelihood ratio between the best-fit and the conventional atmospheric-only hypothesis in the experimental data is 119 TeV to 4.8 PeV.

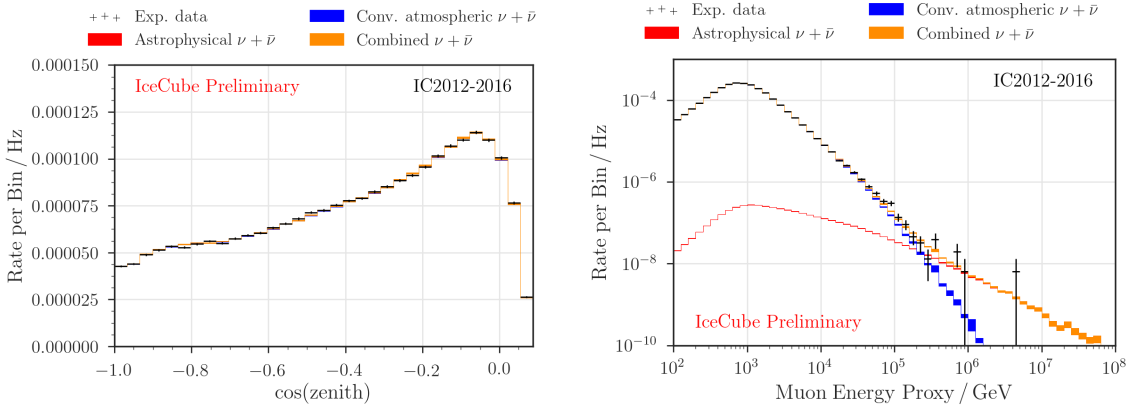


Figure 2 Fitted data distributions for the 2012-2017 detector configuration. Left: Right Projection of zenith. Projection of energy.

Figure 2 shows the comparison of the global best fit with the observation for the most recent detector configuration with two years of added data. The fit results in a good description of the full data-set. No regions of systematic pulls are observed. Visual inspection and other cross checks of these events revealed no indication of any time dependent detector effects. Also the comparison of the earlier detector configurations (2009-2010) remains almost unchanged with respect to [5].

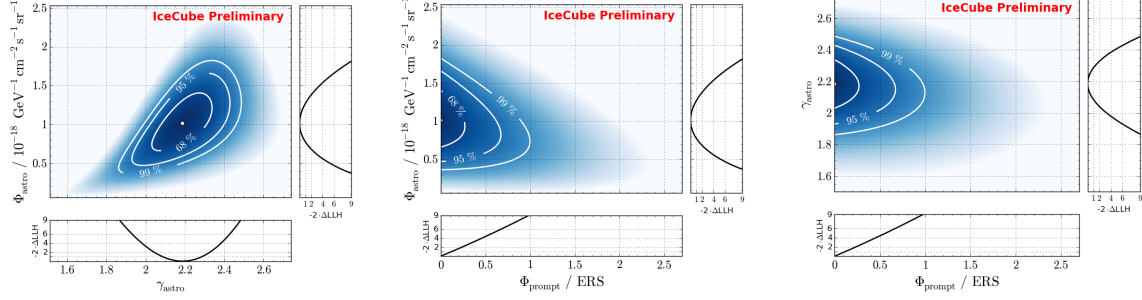


Figure 3 Scans of the profile likelihood for the signal parameters. Note that for each scan point, all other parameters are optimized. Left: Astrophysical normalization versus spectral index. Middle: Astrophysical normalization versus prompt normalization. Right: Astrophysical spectral index versus prompt normalization.

The two-dimensional contours of the profile likelihood as a function of the signal parameters are shown in figure 3. The fitted astrophysical flux normalization is correlated with the astrophysical spectral index, whereas the prompt normalization shows only little correlation to the individual astrophysical flux parameters. Hence, an astrophysical flux with these properties would remain necessary to describe the data even for larger prompt normalizations than the current limit. However, as the prompt flux is sub-dominant to the astrophysical flux, deviations from a pure power-law (as assumed here) would result in large uncertainties for the observation of prompt neutrinos. In particular, the contour lines should not be interpreted as robust limit on the ERS flux.

## 4.2 Astrophysical Flux

The best-fit flux-models and knowledge about the relation between muon energy proxy and true neutrino energy that is derived from simulations can be used to unfold the neutrino energy distribution, as described above. Based on the per-event probability density function  $P(E_\nu | E_i^{reco})$  the median neutrino energy for each event is calculated. Figure 4 (left) shows the distribution of the median neutrino energies for the eight year sample. A clear excess above approximately 100 TeV in neutrino energy is visible and is not compatible with the atmospheric background expectation. Although only a single event with an energy deposition greater than a PeV has been observed, we can estimate from our fit and from the relation between muon energy loss and energy of the parent neutrino that most likely several neutrinos with energies above a PeV are contained in the sample. The updated best-fit astrophysical flux is shown in figure 4 (right) in comparison with the measurements of high-energy starting events [6].

## 4.3 Test for a Spectral Cutoff

In addition to a fit of the baseline astrophysical flux model, we have performed a hypothesis



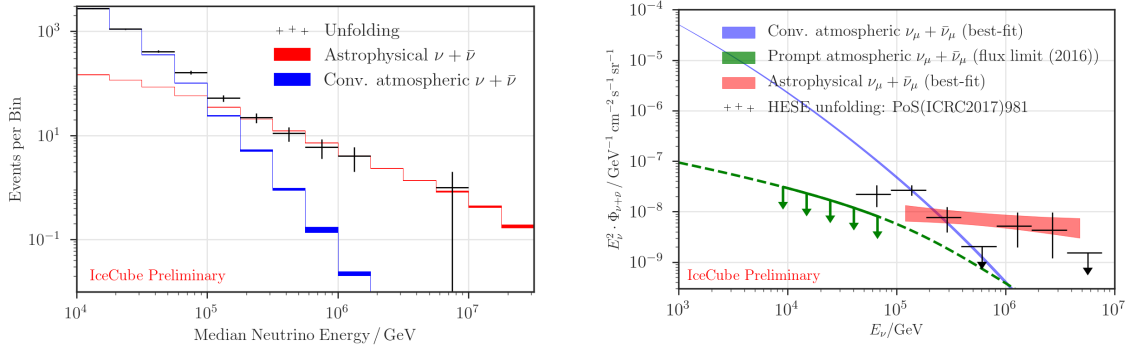


Figure 4 Measured astrophysical flux. Left: Unfolded neutrino energy spectrum in comparison to the best-fit fluxes. Right: Uncertainty range of the observed astro-physical per-flavor flux in comparison with the best fit atmospheric background and the results from the starting event analysis [6].

test for a spectral cutoff implemented as exponential factor in the flux model:

$$\frac{d\Phi_{\nu+\bar{\nu}}}{dE} = \exp\left(-\frac{E}{E_{cut}}\right) \cdot \Phi_{astro} \cdot \left(\frac{E}{100 \text{ TeV}}\right)^{-\gamma_{astro}} \cdot 10^{-18} \text{ GeV}^{-1} \text{ cm}^{-2} \text{ s}^{-1} \text{ sr}^{-1}. \quad (4.2)$$

The cutoff energy  $E_{cut}$  is found to be strongly degenerate with a softer spectral index  $\gamma$ , and both parameters cannot be fitted concurrently. Therefore, the test is performed for two distinct assumptions of the astrophysical flux parameters: (A) The best fit hypothesis with  $\gamma_{astro} = 2.19$  and (B) a benchmark model with  $\gamma_{astro} = 2.0$ . All other parameters are free in the fit.

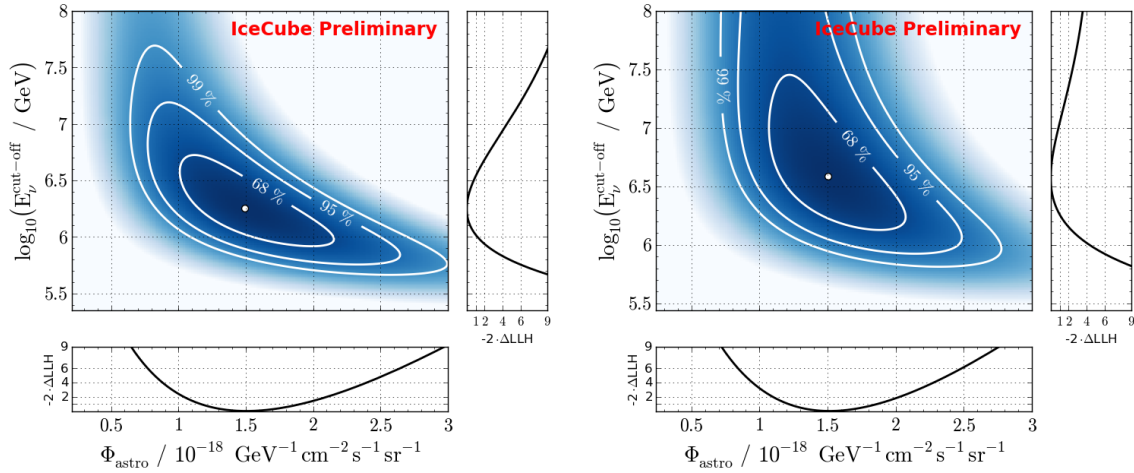


Figure 5 Likelihood scan for the hypothesis test of a spectral cut-off. Left  $\gamma_{astro} = 2.0$ . Right:  $\gamma_{astro} = 2.19$

The results of both fits are shown in figure 5 as 2D profile likelihood scans in  $E_{cut}$  and  $\Phi_{astro}$ . For our best-fit spectrum (A) a cut-off is not significant. However, for an index harder than preferred by our measurement a cut-off would be required. For the benchmark hypothesis (B) of a hard



Table 1 Summary of the highest energy events (above 200 TeV estimated muon energy) in addition to the events reported in [5]. The signalness is defined as the ratio of the astrophysical expectation over the sum of the atmospheric and astrophysical expectations for a given energy proxy and the best-fit spectrum. The angular errors are statistical and do not include systematic uncertainties.

ID	MJD	Signalness	Energy Proxy (TeV)	Decl. (deg)	90% C.L.	R.A. (deg)	90% C.L.
30	57217.9	0.61	300	26.1	+1.68 -1.85	325.5	+1.77 -1.46
31	57246.8	0.69	380	6.0	+0.48 -0.34	328.4	+0.59 -0.75
32	57269.8	0.51	220	28.0	+0.47 -0.47	134.0	+0.39 -0.58
33	57312.7	0.52	230	19.9	+2.82 -2.21	197.6	+2.46 -2.09
34	57340.9	0.86	740	12.6	+0.61 -0.58	76.3	+0.75 -0.74
35	57478.6	0.69	380	15.6	+0.53 -0.60	15.6	+0.45 -0.58
36 <sup>†</sup>	57672.1	0.64	330	26.6	—	9.7	—

<sup>†</sup> Based on preliminary reconstruction methods

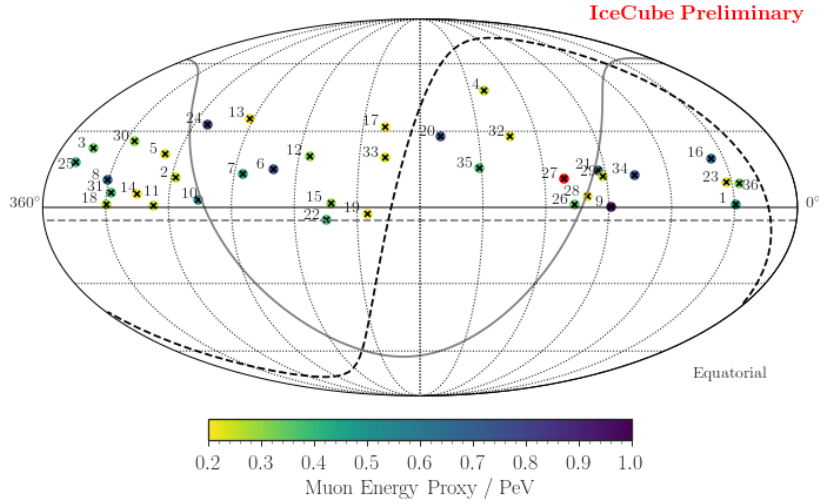


Figure 6 Reconstructed arrival directions of observed events with estimated muon energies above 200 TeV. The color indicates the energy. The number refers to table 1 and the events reported in [5]. The solid gray line indicates the galactic plane and the dashed black line the supergalactic plane.

spectrum ( $\gamma_{astro} = 2$ ), a cutoff at  $\log_{10}(E_\nu) = 6.25$  is preferred at the  $4.1\sigma$  level compared to the benchmark hypothesis without cutoff.

#### 4.4 High Energy Events

Seven new events with estimated muon energies above 200 TeV have been found in the new data. Table 1 shows a summary of the event properties.

The arrival directions of these events are shown in figure 6. Similar to the previous result, no obvious correlation with astrophysical sources has been found. Also, the directions of the new events are not correlated with the directions of previous events.

## 5. Conclusions and Outlook

We have presented the update of the analysis of up-going muon neutrinos, now covering eight years of IceCube operation, including data up to May 2017. The significance of the presence of an isotropic astrophysical muon neutrino flux with respect to a purely atmospheric origin is increased to  $6.7\sigma$ . Despite of not having observed new events of very high energy depositions, the measured flux parameters  $\phi_{astro} = 1.01$   $\gamma_{astro} = 2.19$  are consistent with the previously reported values.

In the previous analysis [5] we have reported an approximately 3 sigma tension in the measured astrophysical spectrum in comparison to a global fit of other IceCube results if a single unbroken power-law is assumed. With the new data reported here this tension remains at the same level. However, this tension is reduced to about 2 sigma, when compared with new data for cascades [14] and starting events [6]. Therefore the possible existence of a spectral feature remains an open question that will be particularly addressed by an update of the global fit [15]. This analysis is also able to constrain the prompt atmospheric neutrino flux. Similar to the previous result [5], no indications of the existence of a prompt flux are observed and limits are expected to further improve. Because the strong astrophysical flux is a background for this search the uncertainties due to the astrophysical flux are difficult to quantify. These studies are still ongoing, and a limit will be presented later.

## References

- [1] **IceCube** Collaboration, M. G. Aartsen et al., *JINST* **12** (2017) P03012.
- [2] **IceCube** Collaboration, M. G. Aartsen et al., *Science* **342** (2013) 1242856.
- [3] **IceCube** Collaboration, M. G. Aartsen et al., *Phys. Rev. Lett.* **113** (2014) 101101.
- [4] **IceCube** Collaboration, M. G. Aartsen et al., *Phys. Rev. Lett.* **115** (2015) 081102.
- [5] **IceCube** Collaboration, M. G. Aartsen et al., *Astrophys. J.* **833** (2016) 3.
- [6] **IceCube** Collaboration, [PoS \(ICRC2017\) 981](#) (these proceedings).
- [7] M. Honda et al., *Phys. Rev.* **D75** (2007) 043006.
- [8] J. R. Hoerandel, *Astropart. Phys.* **19** (2003) 193–220.
- [9] T. K. Gaisser, T. Stanev, and S. Tilav, *Front. Phys.* **8** (2013) 748–758.
- [10] A. Schukraft. PhD thesis, RWTH Aachen University, 2013.
- [11] R. Enberg, M. H. Reno, and I. Sarcevic, *Phys. Rev.* **D78** (2008) 043005.
- [12] D. Chirkin, [arXiv:1304.0735 \[astro-ph.IM\]](#) (2013).
- [13] S. S. Wilks, *Ann. Math. Statist.* **9** (1938) 60–62.
- [14] **IceCube** Collaboration, [PoS \(ICRC2017\) 968](#) (these proceedings).
- [15] **IceCube** Collaboration, [PoS \(ICRC2017\) 976](#) (these proceedings).

## Characterizing the Flux of Atmospheric Neutrinos with IceCube-DeepCore

---

### The IceCube Collaboration<sup>1</sup>

<sup>1</sup> [http://icecube.wisc.edu/collaboration/authors/icrc17\\_icecube](http://icecube.wisc.edu/collaboration/authors/icrc17_icecube)

E-mail: [trwood@ualberta.ca](mailto:trwood@ualberta.ca)

The IceCube Neutrino Observatory instruments more than a cubic-kilometre of the deep glacial ice below South Pole Station, Antarctica, creating the world's largest water Cherenkov detector. With the addition of a low-energy detection array, DeepCore, completed in 2010, the observatory is sensitive to neutrinos with energies between  $\sim 5$  GeV and the EeV-scale. IceCube has now accumulated the world's largest sample of atmospheric neutrinos, providing the ability to perform precision studies of the flux over the full energy range of the detector. We present sensitivities of atmospheric neutrino flux measurements from  $\sim 6$  GeV - 180 GeV with particular attention to the kaon-to-pion ratio. This analysis will fill in the overlapping regions of atmospheric neutrino flux measurements established at low energies by Super-Kamiokande and at higher energies by IceCube, bridging the current experimental results.

**Corresponding author:** Tania Wood

*Department of Physics, University of Alberta, Edmonton, AB, Canada T6G 2G7*

*35th International Cosmic Ray Conference ICRC2017-  
10-20 July, 2017  
Bexco, Busan, Korea*

## 1. Introduction

Precision measurements of atmospheric neutrinos provide an opportunity to study neutrino interactions with world-leading sensitivity. The atmospheric neutrino spectrum provides a sample that has been used to study neutrino oscillations very successfully [1, 2]. In addition, due to the advancement of neutrino detectors, atmospheric neutrino measurements are now capable of providing precision input to cosmic ray and hadronic interaction models. Atmospheric neutrino flux calculations [3, 4] require as minimum input: the cosmic ray spectrum model (which provides the energy spectrum of the incident particles that create the particle shower), the hadronic interaction model (which governs the production of particles as well as their interactions) and the atmospheric density profile model (which provides the atmospheric content, thickness and particle density). The cosmic ray spectrum model and hadronic interaction model represent the largest uncertainties in these predictions [5]; their precision study remains a challenge for the field.

IceCube's DeepCore sub-array [6] measures atmospheric neutrinos in an energy range suited for addressing these questions. The unprecedented statistics of neutrino candidates collected by the DeepCore detector make it possible to study the spectral shape of atmospheric neutrinos, which is closely tied to that of the cosmic rays. Moreover, the detector is sensitive to the crossover region between the dominant meson production in the showers, pions and kaons, which are in turn tied to the hadronic interactions. Here we present an analysis of the atmospheric neutrino spectrum, as well as a sensitivity to the relative contribution of kaons and pions to the neutrino flux using a sample collected by IceCube-DeepCore.

## 2. Detector Description

The IceCube Neutrino Observatory [7] is a large-scale Cherenkov detector that uses the West Antarctic Ice Sheet as the detection medium for charged particles produced in neutrino interactions. The natural deep ice, reaching nearly 3 km thickness at the Amundsen-Scott South Pole Station, is an excellent Cherenkov medium due to its high optical clarity [8]. The IceCube detector array instruments more than a cubic kilometer of the ice, at depths between approximately 1.5 km and 2.5 km. In total, 5160 digital optical modules (DOMs) [7], consisting of a 10-inch photomultiplier tube and full on-board data acquisition contained in a glass pressure housing, are deployed on a hexagonal grid of 86 strings, with 60 DOMS per string.

The primary IceCube array consists of 78 strings with 125 m spacing between strings and DOM-to-DOM spacing of 17 m. In the analysis presented here, this high-energy portion of the detector is used as an active veto region to reject atmospheric muon events [9]. The remaining 8 strings make up the DeepCore sub-array, instrumenting approximately  $10^7 \text{ m}^3$  of the ice in the bottom-center of the IceCube array [6]. This is the deepest, clearest ice of the instrumented region [8] and, with a string spacing between 40 m and 70 m, and a DOM-to-DOM spacing of 7 m, provides a low-energy threshold for neutrino interactions of  $\sim 5 \text{ GeV}$ . The DeepCore data set is the primary source for the analysis presented here, and events typically have a pointing resolution of  $\sim 25^\circ$  at 30 GeV.

### 3. Neutrino Flux Modeling

Cosmic rays incident on the Earth interact with nuclei in the atmosphere, resulting in hadronic showers that produce a multitude of secondary particles [3]. The particles include mesons that then ultimately decay into charged leptons and neutrinos.

The energy spectra and zenith distribution of these leptons contain information about the primary cosmic rays, hadronic interactions and the decay chain leading to their production. Figure 1 shows the relative contributions of meson decays to the atmospheric neutrino flux in the energy regime for the analysis. As shown in Figure 1, the  $\nu_\mu$  flux is dominated by contributions arising from the decay of charged pions ( $\pi^\pm$ ) and kaons ( $K^\pm$ ). Over the energy range of the sample, the dominant contributing mesons are pions at lower energies with kaons becoming dominant above  $\sim 80$  GeV, depending on the zenith angle and choice of hadronic interaction model. For  $\nu_e$ , the flux is dominated by contributions from the decay of muons,  $K_L^0$  and  $K^\pm$ .

The kaon-to-pion ratio ( $K/\pi$ ) is used in parametrizations of the muon neutrino ( $\nu_\mu$ ) flux and is defined as the quotient of the fraction of leptons coming from kaon decay over the fraction of leptons coming from pion decay. It depends on branching ratios and energy distributions of a given decay and is a function of zenith. A good knowledge of these processes is needed to obtain a robust understanding of the spectrum at higher energies and associated uncertainties. This knowledge is critical for atmospheric neutrino studies of fundamental neutrino properties and to determine backgrounds for astrophysical neutrino searches.

As shown in Figure 2, the atmospheric muon neutrino flux produced by  $\pi$  has a notable zenith and energy dependence. This leads to a zenith and energy dependence for the  $K/\pi$  ratio. The zenith angle dependence derives from the variation of the atmosphere traversed by the mesons and the difference in their lifetimes. The angular dependence of the  $\pi$  component creates zenith dependent rate changes observable by IceCube, making this analysis sensitive to the  $K/\pi$  ratio. The sensitivity to the  $K/\pi$  ratio is important as a calibration input to interaction models and for the benchmarking of flux models.

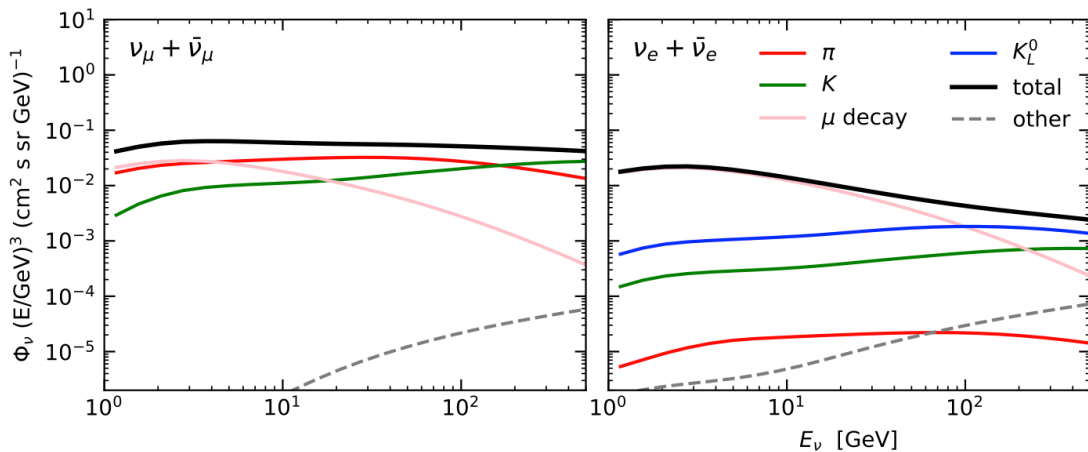


**Figure 1:** Partial contribution of intermediate particles to the flux of atmospheric neutrinos, muon neutrinos (left) and electron neutrinos (right) at zenith angle of  $60^\circ$ . The primary (Cosmic Ray) spectrum is Gaisser-Honda [4] and the interaction model is DPMJET-III [21, 22]. This plot is created with MCEq [10].

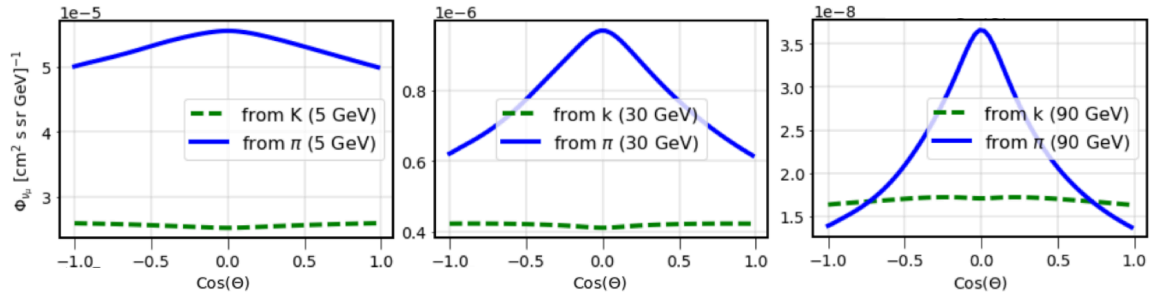


**Figure 2:** Atmospheric muon neutrino flux dependence on zenith-angle and energy, here shown at 5 GeV, 30 GeV and 90 GeV. The zenith angle shown is relative to the IceCube detector coordinate system, where -1 corresponds to ‘upgoing events’.

### 3.1 Current uncertainties on the atmospheric neutrino flux

For neutrinos at GeV energies, the availability of secondary particle production from accelerators and direct cosmic ray flux measurements, results in good model predictions [5]. At higher energies the hadronic and primary flux uncertainties in the absolute neutrino flux increase [5, 11]. As kaons become more relevant as mother meson above approximately  $\sim 70$  GeV neutrino energy, the largest error on the high energy neutrino fluxes comes from the modeling of kaon production. The absence of fixed-target kaon measurements on light nuclear targets results drives the extrapolation errors of hadronic interaction models. For TeV neutrinos, cosmic ray observations in the relevant range become indirect and errors from the primary flux model contribute significantly to the total uncertainty.

The current state of the art characterization of uncertainties is the study of Ref. [5]. The authors assign an uncertainty estimation to each region of the energy-momentum fraction phase-space based on their evaluation of globally available fixed-target data. Due to the steep primary spectrum, the relevant phase-space for inclusive lepton production is  $x_F \gtrsim 0.2$  [16], where  $x_F$  is feynman-x or longitudinal momentum fraction [17]. There are very few measurements of  $x_F \gtrsim 0.2$  as this is the very forward  $p_t$  (transverse momentum) region extremely close to the beam, which accelerator based experiments do not currently measure. There are limited fixed target experiments that do cover some of this region and their integration into these models would be a next step. Atmospheric leptons are largely sensitive to  $x_F \gtrsim 0.2$ , and correspondingly this lack of data in the models leads to large model uncertainties in our region of analysis.

To summarize, current estimates have  $\geq 30\%$  uncertainty in kaon production and  $\geq 15\%$  uncertainty in pion production in the projectile fragmentation region leading to uncertainty in hadronic models in the region that is relevant for the mesons produced in the atmosphere [5]. The  $K/\pi$  ratio measurement outlined could be used to improve and constrain hadronic interaction models in  $x_F \gtrsim 0.2$  and will represent significant improvement over current measurements. This can be seen in the profile likelihood shown in Fig 4, which finds a projected sensitivity of 18% in the  $K/\pi$  ratio at the  $1\sigma$  line (drawn as the horizontal dotted line at 1.0), which one compares to the current best values stated above.

### 3.2 Simulation software

The program Matrix Cascade Equation (MCEq) [10, 18] is a numerical solver of the discrete form of the cascade equation. It facilitates the exploration of the impact from using various models (cosmic ray flux model, hadronic interaction models, atmosphere/density profiles). By testing all possible combinations and varying their input parameters we can explore uncertainties. There, the  $K/\pi$  ratio can be directly computed for a range of physically well motivated possibilities. In our simulation, we calculated the neutrino fluxes specifically for the IceCube detector location, which determines the parameterization of the atmospheric density profile as a function of zenith, averaged over azimuth.

The cosmic ray primary models considered are Gaisser-Honda (GH) [4] and H3a [24]. The static atmosphere employed here is the NRLMSISE-00 model [19]. The hadronic interaction models are SYBILL2.3 [20], EPOS-LHC [23] and DPMJET-III [22, 21].

### 4. Data sample

The data under consideration was collected by IceCube-DeepCore and was prepared with the goal of studying atmospheric neutrino oscillations [9]. The sample, approximately 15,000 events per year, has a 95% neutrino purity with the remainder comprised of cosmic ray muons. The sample is dominated by muon neutrino events and we accept these for all directions (‘full-sky’) in the reconstructed energy range between  $\sim 6$  GeV to 180 GeV, extended from the energy range of  $\sim 6$  GeV to 56 GeV of the original sample. Most notably, this sample uses improved event reconstruction compared to that reported in [2], allowing for events with less direct light and events that are ‘down-going’ to be included in the sample [9]. This improvement in reconstruction was achieved by performing a likelihood-based reconstruction of all events that accounted for both photon scattering and the large-scale variations in the naturally formed glacial ice medium. The inclusion of the down-going events is particularly beneficial since they are primarily unoscillated and therefore help to constrain a source of systematic uncertainty. Backgrounds in the sample from cosmic ray muons are estimated directly from the data, since sufficient simulation is not feasible.

### 5. Analysis Method and Sensitivity Estimates

Data used in the development of this analysis are generated from Monte Carlo (MC) simulation corresponding to the observed events of the described sample from the completed IceCube detector configuration with all high level cuts applied. Sensitivity to a given parameter is explored with Asimov tests using data generated in the same manner. This test data and the MC set are compared using a  $\chi^2$ , described in [9]. The systematic uncertainties related to the flux of neutrinos, as well as those related to the detector, are parameterized and included as nuisance parameters to the fit, with any prior knowledge for a given parameter added to the  $\chi^2$ .

#### 5.1 $K/\pi$ ratio fits

As illustrated in Figure 2, the atmospheric muon neutrino flux is a function of energy and direction. MCEq is used to create tables that contains the expected neutrino flux for each zenith



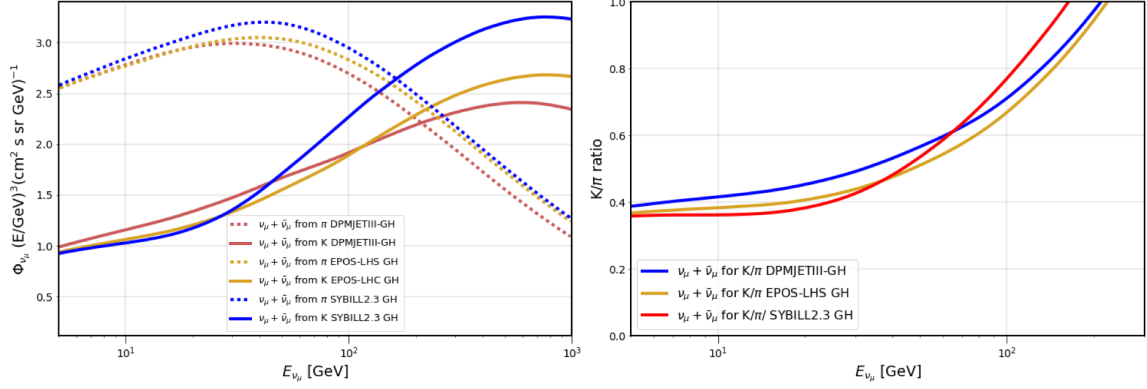


**Figure 3:** Left: The contributions of pions and kaons to the muon neutrino flux integrated over zenith angles are shown separately as a function of neutrino energy. Hadronic interaction models included in the plot are: EPOS-LHC [23], DPMJET-III [21, 22], SYBILL2.3 [20]. Right: Integrated atmospheric  $\nu_\mu$  flux partial contributions, arising from  $\pi$  and K decays. The cosmic ray primary model used was Gaisser-Honda [4] and the atmospheric model is NRLMSISE00 [25]. Plots use [18].

angle and energy. These different tables are then used to weight the available simulation. By comparing the event distributions obtained using different table configurations we estimate of this dataset the sensitivity to the  $K/\pi$  parameter.

In Figure 3 left we see the kaon and pion contributions to the atmospheric muon neutrino flux while changing only the hadronic interaction model. In Figure 3 right we see the muon neutrino flux expected to have kaonic parents over the muon neutrino flux expected to have pionic parents. In this analysis, we keep the template of the atmospheric muon neutrinos decaying from pions fixed and allow the component decaying from kaons to be scaled, and fit this with a  $\chi^2$  method. The scaling of the pion template allows for shifting of the crossover point where kaons begin to

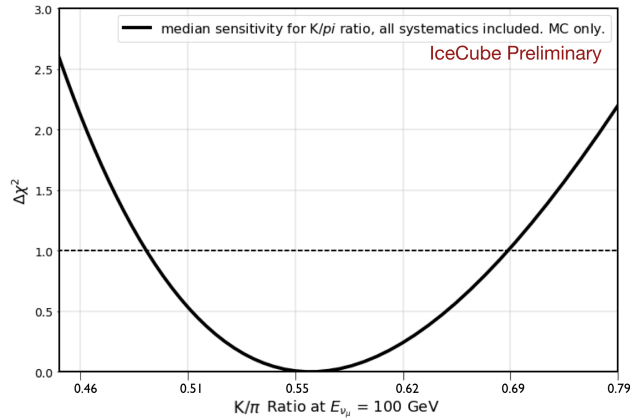


**Figure 4:** Model independent median sensitivity for IceCube DeepCore to the  $K/\pi$  ratio, all systematics included. Note this plot is an Asimov expectation (no statistical fluctuations). It represents the model independent mean expected sensitivity of our segmented energy spectrum fit to the  $K/\pi$  ratio. The x-axis shows the actual ratio predicted by the model used for zenith information, here DPMJET-III with GH, where 0.55 represents  $N_K = 1$  in Figure 3.

dominate as the source for muon neutrinos. The choice of which parent mesons table to fix is arbitrary. The relationship between Figure 3 and Figure 4 can be understood through the following equation:  $\Phi = N(\Phi_\pi + N_K\Phi_k)$ , where  $\Phi$  represents the flux,  $N$  is the overall normalization of the flux and  $N_K$  is the normalization of the kaonic parent template. Figure 4 represents the preferred value of  $N_K$  for a given model and can be used to compute the change in the  $K/\pi$  ratio at all energies. Figure 3 left represents the case where  $N_K = 1$ , *i.e.* the ratio predicted by the model. Figure 4 shows the predicted sensitivity for this analysis to the  $K/\pi$  ratio. The  $1\sigma$  range for the currently expected uncertainties on this parameter are approximately an order of magnitude improvement on current best results [5].

## 5.2 Energy spectrum fit

The fitting of the energy spectrum as seen in Figure 5 is performed with a quasi-model-independent approach. This is performed by fitting a number of distinct spectral segments in energy, which can together approximate the shape of the full spectrum. Each segment is given an energy dependence of  $E^{-3}$ , as this is not too dissimilar from any of the model predictions over the small domain of each segment. The zenith profile of each segment is taken to be the same as the prediction from the DPMJET-III hadronic model. In the fit each segment's normalization is treated as a separate free parameter, preserving the the zenith profile and the  $\nu/\bar{\nu}$  ratio. The  $K/\pi$  ratio is also fit in this process. Each segment consists of a pionic flux template and a kaonic flux template whose zenith profits are taken from DPMJET-III and is normalized as outlined in the previous section. There is one shared scaling factor of the kaonic component. The energy spectrum,

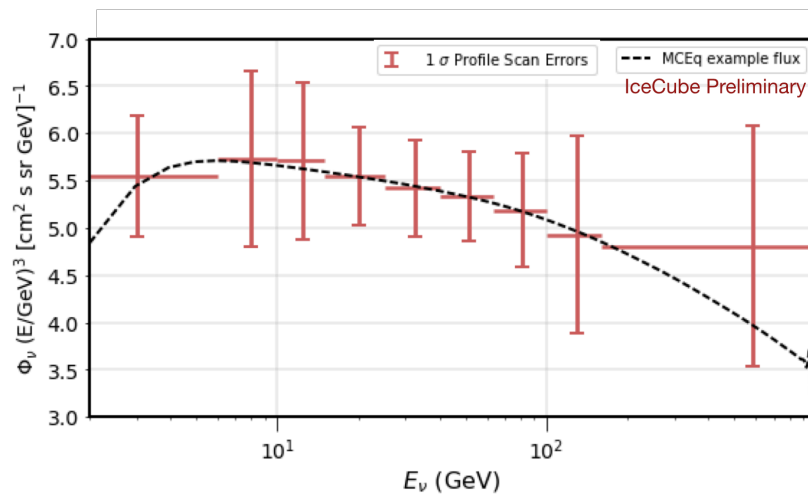


**Figure 5:** Expected atmospheric muon neutrino flux from MC data, including all systematic and statistical uncertainties for  $\nu_e + \nu_\mu$ , as a function of the logarithm of the neutrino energy. No statistical fluctuations are included here. The error bars correspond to the  $1\sigma$  band obtained from a profile scan performed for each point. The dashed line shows the model injected as a test spectrum.

oscillation parameters (fitted as nuisance parameters),  $K/\pi$  ratio, and detector systematics are all fit simultaneously. The flux error per point (or segment) is the  $1\sigma$  of a profile scan evaluated for that segment. Preliminary sensitivity using MC only can be seen in Figure 5.

## 6. Future work

The analysis demonstrates excellent potential for improving our global knowledge on a key energy range and will provide the ability to perform precision studies of the neutrino spectrum over the full energy range of the detector. Going forward, we will split the total atmospheric neutrino energy spectrum into separate  $\nu_\mu$  and  $\nu_e$  flux components. We anticipate a similar precision to what is shown in Figure 5. The  $K/\pi$  ratio analysis demonstrates the potential to reach precision values and contribute to future hadronic interaction model refinement. Further, the advanced atmospheric neutrino flux modeling tools now in place in this analysis will permit continuing improvement of our treatment of the atmospheric neutrino flux uncertainties, leading to improved oscillation results and neutrino property measurements.

## References

- [1] **Super-Kamiokande** collaboration, Y. Fukuda et. al., *PRL* **81**, 1562 (1998).
- [2] **IceCube** Collaboration, M.G. Aartsen et al., *Phys. Rev. D*, **91**, 072004 (2015).
- [3] T. K. Gaisser, R. Engel, and E. Resconi, *Cambridge University Press* (2016).
- [4] T. K. Gaisser and M. Honda, *Ann. Rev. Nucl. Part. Sci.* **52**, 153 (2002).
- [5] G. D. Barr, T. K. Gaisser, S. Robbins and T. Stanev, *Phys. Rev. D* **74** 094009 (2006).
- [6] **IceCube** Collaboration, R. Abbasi et al., *Astropart. Phys.* **35**, 1109.6096 (2012).
- [7] **IceCube** Collaboration, M. G. Aartsen et al., *JINST* **12** P03012 (2017).
- [8] **IceCube** Collaboration, M.G. Aartsen et al., *Journal of Glaciology* **59** (2013).
- [9] J.P.A.M Andre for the **IceCube** Collaboration, *IPA Symposium* (2017).
- [10] A. Fedynitch, R. Engel, T. K. Gaisser, F. Riehn and T. Stanev, *POS (ICRC2015)* 1129 (2016).
- [11] A. Fedynitch, J. Becker Tjus and P. Desiati, *Phys. Rev. D* **86** 114024 (2012).
- [12] **NA49** Collaboration, *Eur. Phys. J. C* **49**, 897 (2007), **73**, 2364 (2013).
- [13] **NA49** Collaboration, C. Alt et al., *Eur. Phys. J. C* **45**, 343 (2006).
- [14] **NA49** Collaboration, T. Anticic et al., *Eur. Phys. J. C* **65** 9 (2010).
- [15] **NA49** Collaboration, T. Anticic et al., *Eur. Phys. J. C* **68**, 1 (2010).
- [16] R. M. Ulrich et al., *POS (ICRC2015)* 407 (2016).
- [17] K. Goulianos, *FERMILAB-Conf-94/266-E* (1996).
- [18] A. Fedynitch, R. Engel, T. K. Gaisser, F. Riehn and T. Stanev, *EPJ Web Conf.* **99**, 08001 (2015).
- [19] J. M. Picone, A. E. Hedin, D. P. Drob, and A. C. Aikin, *J. Geophys. Res.*, **107** (A12), 1468, (2002).
- [20] F. Riehn, R. Engel, A. Fedynitch, T. K. Gaisser and T. Stanev, *POS (ICRC2015)* 558 (2016).
- [21] S. Roesler, R. Engel and J. Ranft, *Monte Carlo* (2000).
- [22] A. Fedynitch and R. Engel, *ICNRM 2014* (2015).
- [23] T. Pierog, I. Karpenko, J. M. Katzy, E. Yatsenko and K. Werner, *Phys. Rev. C* **92**, 034906 (2015).
- [24] T. K. Gaisser, *Astropart. Phys.* **35**, 801 (2012).
- [25] M. Honda et al., *Phys. Rev. D* **92**, 023004 (2015).

# Measurement of High Energy Neutrino–Nucleon Cross Section and Astrophysical Neutrino Flux Anisotropy Study of Cascade Channel with IceCube

---

## The IceCube Collaboration<sup>†</sup>

<sup>†</sup> [http://icecube.wisc.edu/collaboration/authors/icrc17\\_icecube](http://icecube.wisc.edu/collaboration/authors/icrc17_icecube)

E-mail: [yiqian.xu@stonybrook.edu](mailto:yiqian.xu@stonybrook.edu)

We present a novel analysis method and performance studies to determine the neutrino-nucleon deep-inelastic scattering cross section at high energies. The analysis uses atmospheric and extraterrestrial neutrino-induced electromagnetic and hadronic showers (cascades) in the TeV-PeV energy range, and assumes that the extraterrestrial neutrino flux is isotropic. Signal samples are separated into two groups, "down-going" (from the Southern Hemisphere) and "up-going" (from the Northern Hemisphere). Since up-going events may interact and be absorbed by the Earth while down-going event rate remains unaffected, the ratio of down-going events and up-going events for certain energy range is correlated with the cross section value. At the energies in this study, the yields are sensitive to the neutrino-nucleon cross section and nucleon structure in a region of kinematic overlap with HERA and with the LHC. We present the method for the neutrino-nucleon cross section measurement in the TeV-PeV energy range using neutrino induced cascades with the complete IceCube detector. In addition, we will test the hypothesis of a North-South anisotropy in astrophysical neutrino flux, assuming the knowledge of the neutrino-nucleon cross section from the electroweak physics.

**Corresponding authors:** Yiqian Xu<sup>1\*</sup>

<sup>1</sup> *Department of Physics and Astronomy, Stony Brook University, Stony Brook, NY 11794-3800*

*35th International Cosmic Ray Conference ICRC2017-  
10-20 July, 2017  
Bexco, Busan, Korea*

---

\*Speaker

POS (ICRC2017) 978

**Introduction** IceCube is a cubic-kilometer neutrino detector installed in the ice at the geographic South Pole [1] between depths of 1450 m and 2450 m, completed in 2010. It detects all-sky neutrinos of all flavors. Reconstruction of the direction, energy and flavor of the neutrinos relies on the optical detection of Cherenkov radiation emitted by charged particles produced in the interactions of neutrinos in the surrounding ice or the nearby bedrock. IceCube is sensitive to neutrinos above 100 GeV [2], and the energy range of this study is TeV–PeV, which overlaps with the kinematic of HERA [3] and with the LHC [4]. Their actual measurement forms a valuable proof-of-concept towards measurement in the high energy regime, which will provide sensitivity to new physics with unique neutrino probes. Direct neutrino-nucleon cross section measurements done with fixed target experiments cease at neutrino energies 370 GeV. The energy sensitivity of IceCube makes it possible to make measurements beyond the fixed target experiments' energy limit. IceCube has recently made the first measurement of the muon-neutrino-nucleon cross section at neutrino energies above 6 TeV using  $\nu_\mu$  coming from the Northern Sky observed by the IceCube 79-string configuration in 2010 [5]. This analysis proposes a novel method [6] using neutrinos of all flavors from all-sky collected with the 2011–2015 IceCube 86-string configuration to measure the neutrino-nucleon cross section.

**Event Selection** Events observed in IceCube are classified by their topology. Cascade events are induced by  $\nu_e, \nu_\tau$  charge current and neutral current interactions, or  $\nu_\mu$  neutral current interactions. The emitted light forms a shower-like pattern. Track-like events are through-going muons. The source of track-like events can be cosmic ray induced muons from the Southern Sky or muons induced by  $\nu_\mu$  charge current interactions. When  $\nu_\mu$  charge current interactions happen within the detector volume, it creates a hybrid event. A hybrid event is the combination of a hadronic shower and a track left by an out-going muon. At trigger level, the majority of events seen in the detector are cosmic muons. They are the background for this analysis. To better understand detected events and design filters for event classification, Monte Carlo simulations are generated. *MuonGun* software is used to directly generate muons in ice with the composition from [7]. *Neutrino-generator* is used to generate neutrino interactions. Conventional atmospheric neutrino flux is calculated with HKKMS06 [8] and prompt atmospheric neutrino flux is calculated with BERSS [9]. For atmospheric flux, the "self-veto" effect [10] is taken into consideration. Astrophysical neutrino flux modeled with is a single, unbroken power law with the preliminary fit result from the IceCube 4-Year Cascade analysis: normalization:  $(1.5^{+0.23}_{-0.22}) \times 10^{-18} \text{ GeV}^{-1} \text{ s}^{-1} \text{ sr}^{-1} \text{ cm}^{-2}$ , spectrum index:  $-2.48 \pm 0.08$  [11]. The signal for this analysis is contained cascade events. The energy resolution for such events can be as good as 15% of deposited energy [12]. Event selection for this analysis is the same as in Ref. [11]. The selection separates the sample into two parts: the high energy part ( $E_{reco} > 60 \text{ TeV}$ ) and the low energy part ( $E_{reco} \leq 60 \text{ TeV}$ ). The high energy event selection uses a 2D straight cut to select cascade events with high purity, has high efficiency, and is nearly background free. Low energy event selection uses a Boosted Decision Tree to classify events into three categories: cascade sample, muon sample, and starting track sample. Only cascade sample is used in this analysis. The low energy sample which consists 4017 neutrino events has a much higher statistic compare to high energy sample (19 neutrino events), and the background rate is lower than 10%. This analysis aims to use data collected from May, 2011 to May, 2016, 1730 days of livetime in total. To keep the development of the analysis method unbiased, only Monte

Carlo simulation and 10% of the collected data are currently used in this analysis. This 10% of the experimental data consists of data equally spaced throughout the years and is called *burn sample*. Final sample consists of neutrinos of all flavors. The number of events from Southern Sky and Northern Sky in each reconstructed energy bin for data and Monte Carlo is shown in Table 1

Table 1: Number of events (burn sample livetime) in reconstructed energy bins for data & Monte Carlo (numbers in parentheses are statistical uncertainties).

Southern Sky						
$\log_{10}(E_{reco}/GeV)$	$\nu_e$	$\nu_\mu$	$\nu_\tau$	$\mu$	$MC_{sum}$	Data
2.2-2.8	2.56(7)	5.6(5)	0.035(2)	3(1)	11(2)	9
2.8-3.4	17.8(1)	42(1)	0.95(1)	12(4)	73(4)	66
3.4-4.0	17.00(7)	31.8(8)	3.06(1)	6(2)	58(2)	52
4.0-4.6	6.02(1)	6.2(1)	2.484(9)	0.5(1)	15.2(2)	19
4.6-5.2	1.712(4)	0.59(2)	0.937(5)	0	3.24(2)	5
5.2-5.8	0.505(2)	0.082(3)	0.261(2)	0	0.848(4)	1
5.8-6.4	0.140(1)	0.027(2)	0.068(1)	0	0.236(2)	1
6.4-7.0	0.082(2)	0.003(1)	0.008(1)	0	0.093(2)	0
Northern Sky						
$\log_{10}(E_{reco}/GeV)$	$\nu_e$	$\nu_\mu$	$\nu_\tau$	$\mu$	$MC_{sum}$	Data
2.2-2.8	10.8(1)	41(1)	0.342(5)	0	52(1)	51
2.8-3.4	48.2(2)	166(2)	3.77(2)	14(4)	231(4)	242
3.4-4.0	26.87(8)	71(1)	4.76(2)	8(3)	111(3)	93
4.0-4.6	6.15(1)	8.5(1)	2.17(1)	0.6(1)	17.4(2)	17
4.6-5.2	1.252(3)	0.58(2)	0.620(6)	0	2.45(2)	3
5.2-5.8	0.258(1)	0.050(2)	0.135(2)	0	0.443(3)	0
5.8-6.4	0.052(1)	0.013(1)	0.028(1)	0	0.093(1)	0
6.4-7.0	0.015(1)	0.002(1)	0.004(1)	0	0.021(1)	0

### Analysis Method

This analysis follows the theoretical approach from Ref. [6]. In Ice-Cube, neutrinos from Northern Sky travel through the Earth to reach the detector. When traveling through the Earth, a fraction of the neutrinos are absorbed by the Earth. This fraction is a function of cross section [6]. The fraction can be obtained by calculating a ratio of down-going events (Southern Sky) and up-going events (Northern Sky), since neutrinos from Southern Sky are not affected by the Earth absorption effect. The desired relationship is between cross section and neutrino energy, as shown in Fig. 4. The number of down-going events and up-going events in reconstructed energy bins can be experimentally measured, and an unfolding method (discussed later) is applied to get the number of events in neutrino energy bins. The ratio in each neutrino energy bin is the number of down-going events divided by the number of up-going events. With Monte Carlo simulation, we can get the relationship between the Earth absorption effect (which is expressed by the ratio of down-going events and up-going events) and cross section. In this way, the cross section for a certain neutrino energy range can be measured. The relationship between the ratio of down-going events and up-going events and cross section can be obtained by using *neutrino-generator* Monte Carlo simulation. Neutrinos with different interacting cross sections (from  $\sim 10^{-9}$  mb to  $\sim 10^{-4}$  mb) are simulated and propagated towards the detector from all directions. The Earth model used in the simulation is PREM [13]. All neutrinos are forced to interact and are given a proper weight according to cross section. For each cross section bin, events inside are separated

into two parts:  $\cos(\text{Zenith}_{reco}) < 0$  as up-going, and  $\cos(\text{Zenith}_{reco}) \geq 0$  as down-going. The reconstructed zenith( $\theta$ ) distribution is shown in Fig. 1 (Right). The ratio of the number of down-going events over the number of up-going events is plotted for each cross section bin (shown as Fig. 1 (Left)). Both atmospheric neutrino flux and astrophysical neutrino flux are taken into consideration when counting the number of events, since we can't distinguish these two types of neutrinos at lower energy. Due to the existence of *self-veto effect* [10] in atmospheric neutrinos, the detector accepts down-going atmospheric neutrinos at a much lower rate than up-going atmospheric neutrinos due to the accompanied muons in down-going events. Also, the event selection [11] applied shows differences in the down-going and up-going events acceptance rates. With all these factors, the ratio of down-going events and up-going events will contain not only the information of Earth absorption, but also detector acceptance effects. These acceptance effects are neutrino energy dependent and can be factorized. Therefore, it is necessary to apply a correction factor (as shown in Fig. 3 (Right)) once the ratio in neutrino energy bins is obtained. This way, we decouple the acceptance effect and the ratio reflects the Earth absorption effect only. Occasionally, a neutral current interaction happens in the Earth and produces a secondary neutrino that will reach the detector and interact again within. This secondary neutrino will have a lower energy and a smaller cross section for neutrino-to-matter interaction. This will result in more up-going neutrinos in the lower cross section bin. In general, this effect must be corrected with dedicated simulations, however, in this analysis, we ignored the effect because the statistical uncertainties from the observed events are much larger than this effect. The experimental data are separated into down-going events and

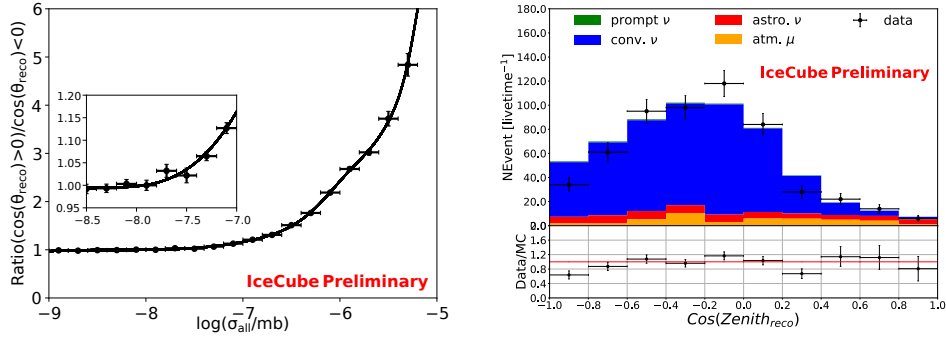


Figure 1: Left: cross section vs ratio of down-going and up-going events. Right: reconstructed zenith distribution for data and Monte Carlo.

up-going events as well. Reconstructed energy histograms are plotted for down-going events and up-going events separately (shown as Fig. 2 (Left column)). What we measure in the experiment is deposited energy, this is not equivalent to neutrino energy, due to out-going neutrinos in neutral current interactions and out-going  $\mu$  carrying away energy in  $\nu_\mu$  charge current interactions. To get the ratio in neutrino energy bins, an unfolding procedure is needed. The unfolding method used here is the matrix method [14]. We define:

$$y_{i,dir} = \sum_j A_{ij,dir} x_{j,dir}, \quad A_{ij,dir} = \frac{N_{ij,dir}^{reco,true}}{N_{i,dir}^{true}}, \quad (1)$$



where  $x_{j,dir}$  is the number of events in neutrino energy bin  $j$  for a certain direction (down-going/up-going according to reconstructed zenith), and  $y_{i,dir}$  is the number of events in reconstructed energy bin  $i$  for a certain direction (down-going/up-going according to reconstructed zenith).  $A_{ij,dir}$  are the elements of the resolution matrix, defined as the number of events in both neutrino energy bin  $j$  and in reconstructed energy bin  $i$  for a certain direction divided by the number of events in neutrino energy bin  $j$  for a certain direction. This matrix is calculated using Monte Carlo simulation. Resolution matrices are calculated for up-going and down-going events respectively. Once we have obtained these resolution matrices, the number of events in neutrino energy bins can be calculated using:

$$x_{j,dir}^{INVERT} = \sum_i (A^{-1})_{ji,dir} (y_{i,dir}^{data} - y_{i,dir}^{bgr}), \quad (2)$$

where  $y_{i,dir}^{bgr}$  is the background expectation from IceCube’s MuonGun simulation in reconstructed energy bin  $i$  for a certain direction, as shown in Fig. 2 (Left column). The uncertainty is defined as  $\delta x_{j,dir}^{INVERT} = \sqrt{V_{jj,dir}}$ , where

$$V_{jk,dir} = \sum_i (A^{-1})_{ji,dir} (\delta (y_{i,dir}^{data} - y_{i,dir}^{bgr}))^2 (A^{-1})_{ki,dir}. \quad (3)$$

The reconstructed energy distributions for up-going and down-going events are shown in Fig. 2 (Left column). After unfolding, neutrino energy distributions for up-going and down-going events are shown in Fig. 2 (Right column). The ratio of down-going events and up-going events for each neutrino energy bin is calculated as  $Ratio_j = \frac{x_{j,down}}{x_{j,up}}$ . After applying the correction factor for acceptance effects (self-veto, efficiency), the result is shown in Fig. 3 (Left).

### Cross Section Result

Figure 3 shows the corresponding ratio for each neutrino energy bin, and Fig. 1 (Left) shows the corresponding cross section value for each ratio. With this information, we can evaluate the cross section in neutrino energy bins. Figure 4 (Left) shows the sensitivity of this measurement with 5 years’ livetime predicted by Monte Carlo simulation. The dark red band and light red band cover 68% and 95% of confidence range respectively (systematic uncertainties are not included). Figure 4 (Right) shows the neutrino-nucleon cross section evaluated with 10% of 5 years of IceCube data (uncertainties are statistical only). The black dots in Fig. 4 represent the CSMS calculations [15]. Here we use the sum of charge current interaction and neutral current interaction cross sections averaged over neutrino and anti-neutrino.

### Astrophysical Neutrino Flux Anisotropy Study

The neutrino-nucleon cross section and the parton distribution functions at the kinematic range where this analysis is sensitive are well understood by the Standard Model and HERA data. In this section, we assume the knowledge of the cross section, and the ratio is sensitive to the (an)isotropy of astrophysical neutrino flux. The approach is to assume the known cross section and calculate the ratio of down-going events and up-going events (separated by reconstructed zenith angle) based on the isotropy model and the anisotropy model respectively. We then compare the ratio from experimental data with the ratios calculated from these two different flux models. For the isotropy model, we assume the neutrino

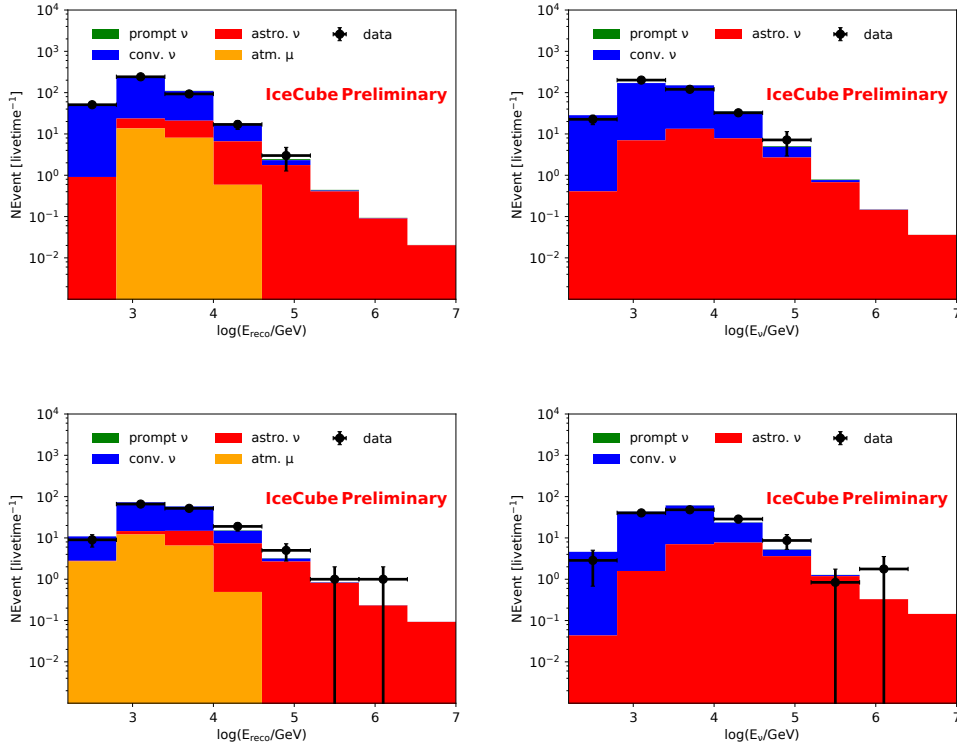


Figure 2: Top Left: reconstructed energy distribution for up-going events. Top Right: neutrino energy distribution for up-going events. Bottom Left: reconstructed energy distribution for down-going events. Bottom Right: neutrino energy distribution for down-going events.

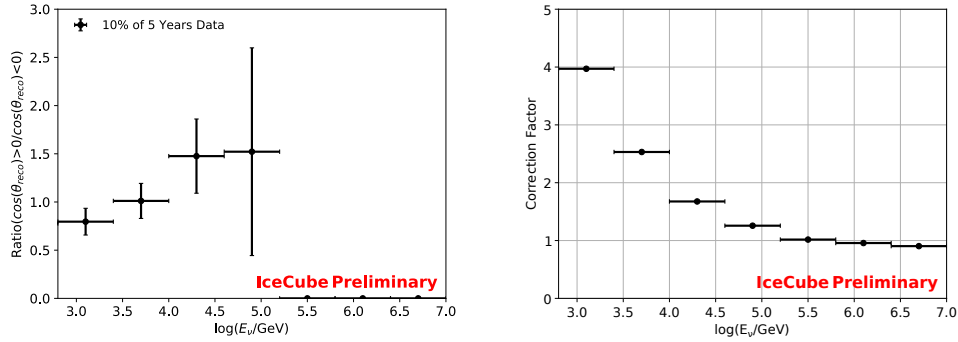


Figure 3: Left: neutrino energy vs ratio of down-going and up-going events for 10% of 5 years data. Uncertainties are statistical only. Right: neutrino energy vs correction factor.

flux is a single power law:

$$\Phi(E_\nu) = \Phi_1 \left( \frac{E_\nu}{E_\nu} \right)^{-\gamma}. \quad (4)$$

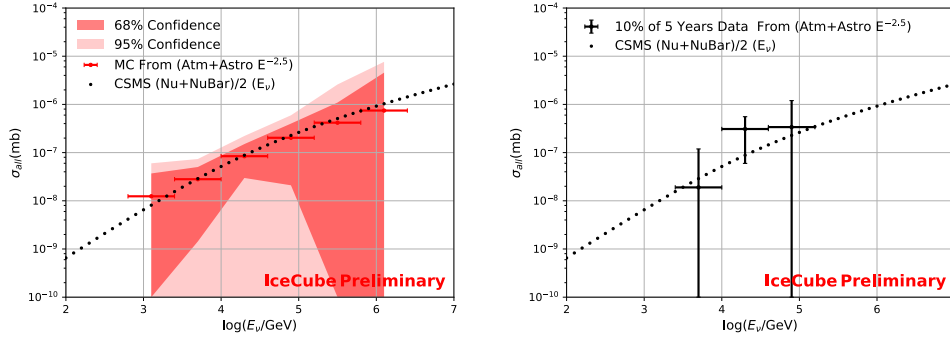


Figure 4: Left: measured neutrino energy vs cross section using Monte Carlo simulation and expected precision with 100% of 5 years of data. Right: measured neutrino energy vs cross section using 10% of 5 years experimental data. Uncertainties are statistical only.

For the anisotropy model, we assume the down-going flux is the same as for the isotropy model and the up-going neutrino flux is:

$$\Phi(E_\nu) = \Phi_1 \left( \frac{\Phi_1}{\Phi_1 + \Phi_2} \left( \frac{E_\nu}{E_0} \right)^{-\gamma_1} + \frac{\Phi_2}{\Phi_1 + \Phi_2} \left( \frac{E_\nu}{E_0} \right)^{-\gamma_2} \right), \quad (5)$$

where  $\Phi_1 = (1.5_{-0.22}^{+0.23}) \times 10^{-18} \text{ GeV}^{-1} \text{ s}^{-1} \text{ sr}^{-1} \text{ cm}^{-2}$ ,  $\gamma_1 = 2.48 \pm 0.08$  are the fit result from the IceCube 4-year cascade analysis [11], and  $\Phi_2 = (1.01_{-0.23}^{+0.26}) \times 10^{-18} \text{ GeV}^{-1} \text{ s}^{-1} \text{ sr}^{-1} \text{ cm}^{-2}$ ,  $\gamma_2 = 2.19 \pm 0.10$  are the fit result from the IceCube 8-year  $\nu_\mu$  analysis [16]. Note that there are many possible anisotropy models, we have tested this one so far to demonstrate how this method works. Figure 5 (Right) shows the ratio of down-going events and up-going events as a function of the (logarithm of) neutrino energy. The bands around the curves are calculated from 68% contours from fit result of [11] and [16] as shown in Fig. 5 (Left). The uncertainty band covers all the ratio values calculated with all the combinations of normalization and index values on the contour. We can see that for the isotropy model the uncertainty band is very narrow, as expected, due to the cancellation of flux in the ratio. The difference in ratio between the two models starts to show at a relative high energy, since in the lower energy range the flux is dominated by atmospheric neutrino component. With 10% of 5 years' statistic, the data doesn't favor one model over another.

### Summary

We have developed a new analysis method [6] to measure the neutrino-nucleon cross section at high energy (TeV–PeV). This method uses the ratio of down-going events and up-going events to probe the effect of Earth absorption in order to get the measurement of cross section. Under the assumption of isotropy of astrophysical neutrino flux the effect of flux is canceled in the ratio, which makes the result of the cross section measurement independent of the flux model. This method has been applied on 10% of 5 years of IceCube data in the cascade channel, and the initial study shows consistency with CSMS [15] cross section calculation. When assuming the standard model cross section, this method can be used to explore the anisotropy of astrophysical neutrino flux. The ratio of down-going events and up-going events for burn sample data is compared with ratios calculated with CSMS calculations for anisotropy

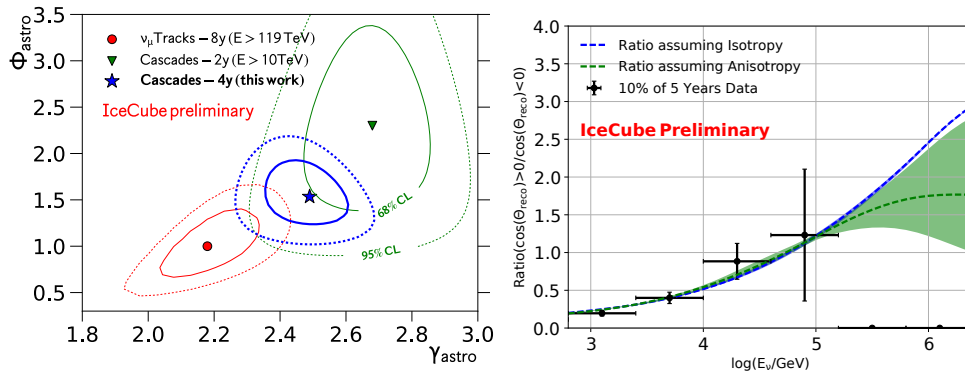


Figure 5: Left: uncertainty contours of IceCube analyses [11]. Right: ratio vs Neutrino Energy for 10% of 5 years' IceCube data.

model and isotropy model. The anisotropy hypothesis studied is single power law flux for Southern Sky and double power law flux for Northern Sky, while the isotropy hypothesis is single power for the whole sky. With 10% of 5 years' statistic, the two hypotheses are indistinguishable. Evaluation of systematic uncertainties is in progress.

## References

- [1] **IceCube** Collaboration, M. G. Aartsen et al., *JINST* **12**, 26, P03012 (2017)
- [2] F. Halzen, S. R. Klein, *Rev. Sci. Instrum.* **81**, 081101 (2010)
- [3] F. D. Aaron et al., *JHEP* **1001** (2010) 109.
- [4] S. Alekhin et al., arXiv:1101.0536 [hep-ph]
- [5] S. Miarecki, PhD Thesis, U.C. Berkeley (2016)
- [6] D. Hooper, *Phys. Rev.* **D65**, 097303 (2002)
- [7] T.K. Gaisser, *Astroparticle Physics* **35**, 801 (2012)
- [8] M. Honda et al., *Phys. Rev.* **D75**, 043006 (2007)
- [9] A. Bhattacharya et al, *JHEP* **06**, 110 (2015)
- [10] T. Gaisser et al., *Phys. Rev.* **D90**, 023009 (2014)
- [11] **IceCube** Collaboration, [PoS \(ICRC2017\) 968](#)
- [12] **IceCube** Collaboration, M. G. Aartsen et al., *JINST* **9**, P03009 (2014)
- [13] A. Dziewonski et al., *Phys. Earth Planet. Inter.* **Vol. 25(4)**: 297-356 (1981)
- [14] V. Blobel, arXiv:hep-ex/0208022
- [15] A. Cooper-Sarkar et al., *JHEP* **08** (2011) 042
- [16] **IceCube** Collaboration, [PoS \(ICRC2017\) 1005](#)

## Observation of Astrophysical Neutrinos in Six Years of IceCube Data

---

### The IceCube Collaboration<sup>†\*</sup>

<sup>†</sup> [http://icecube.wisc.edu/collaboration/authors/icrc17\\_icecube](http://icecube.wisc.edu/collaboration/authors/icrc17_icecube)

E-mail: [analysis@icecube.wisc.edu](mailto:analysis@icecube.wisc.edu)

Cosmic rays arriving at Earth include the most energetic particles ever observed. The mechanism of their acceleration and their sources are, however, still mostly unknown. Observing astrophysical neutrinos can help solve this problem. Because neutrinos are produced in hadronic interactions and are neither absorbed nor deflected, they will point directly back to their source. This contribution covers continued studies of the high-energy astrophysical neutrino flux observed at the IceCube neutrino observatory, extending them from four to six years of data with a focus on energies above 60 TeV. The spectrum and spatial clustering of the observed neutrinos are discussed.

*35th International Cosmic Ray Conference — ICRC2017  
10–20 July, 2017  
Bexco, Busan, Korea*

---

\*Presenter: C. Kopper, University of Alberta

## 1. Introduction

Observation of high-energy neutrinos provides insight into the problem of the origin and acceleration mechanism of high-energy cosmic rays. Cosmic ray protons and nuclei interacting with gas and photons present in the environment of sources and in the interstellar and intergalactic space produce neutrinos through decay of charged pions and kaons. These neutrinos have energies related to the cosmic rays that produced them and point back to their sources since neutrinos are neither affected by magnetic fields nor absorbed by matter opaque to radiation. Large-volume Cherenkov detectors like IceCube [1] observe these neutrinos when they interact in or around the instrumented volume by measuring the light produced by charged particles created in the interaction.

Here we present an update to the IceCube high-energy search for events with interaction vertices inside the detector fiducial volume. This search, previously performed on two [2], three [3] and four [4] years of detector data, led to the discovery of an astrophysical neutrino flux above atmospheric backgrounds [3]. This update extends the data-taking period by two more years to six years from early 2010 to early 2016 for a total livetime of 2078 days.

## 2. Event Selection

Neutrinos in IceCube are detected by observing the Cherenkov light in the glacial ice from secondary particles created by the interaction of high-energy neutrinos. We observe two main event classes: track-like events from charged-current interactions of muon neutrinos (and from a minority of tau neutrino interactions) and shower-like events from all other interactions (neutral-current interactions and charged-current interactions of electron and tau neutrinos). Note that tau neutrino interactions at the highest energies (above a few hundred TeV) can lead to different event shapes such as two cascades separated by a short tau track, which are included in the simulation but are not explicitly reconstructed beyond a classification into tracks and cascades<sup>1</sup>. We determine the event direction and deposited energy in the detector based on the time sequence of the Cherenkov photons and total recorded light. Energy is reconstructed as electromagnetic-equivalent energy (the energy deposited by the events assuming all light was created in electromagnetic showers). Although deposited energy resolution is similar for all events, shower-like events have a typical directional resolution of around 15 degrees, mostly dominated by the uncertainty in the modelling of the glacial ice, whereas track-like events have resolutions of much better than 1 degree.

In the analysis presented here (“high-energy starting events (HESE)”), signal events are selected by requiring the neutrino interaction vertex to be located inside the IceCube fiducial detector volume. We achieve this by means of a simple anti-coincidence veto method [2], requiring that fewer than 3 of the first 250 detected photoelectrons (p.e.) be on the outer detector boundary. In order to ensure a large enough number of photons are detected, we also require at least 6000 p.e. in total charge for each event, corresponding to a soft threshold of about 30 TeV in deposited energy in the detector.

## 3. Atmospheric Backgrounds

Backgrounds to astrophysical neutrinos are entirely due to cosmic ray air showers. Muons produced in these showers, mainly from  $\pi$  and K decays enter the detector from above. Due to the

---

<sup>1</sup>An analysis using the sample discussed here and adding an explicit tau identifier can be found in [5].

stochasticity of the muon energy loss, in very rare cases muons can pass through the outer veto layer undetected and appear as starting events, especially close to the charge threshold of 6000 p.e. A data-driven method is used to estimate this background by tagging such muons in one layer of the detector and using an equivalent second layer to estimate their passing probability. This procedure yields a total atmospheric muon background of  $25.2 \pm 7.3$  events in six years of data.

The same cosmic ray air showers also produce neutrinos from  $\pi$  and K decays. The spectrum of these muon-neutrino dominated atmospheric neutrinos is typically one power steeper than the original cosmic ray spectrum. This is due to the increasing lifetime of the parent mesons, making it more and more likely for them to interact before decaying. At energies above around 100 TeV, an analogous flux of muons and neutrinos from charm-containing mesons is expected to dominate. The shorter lifetime of these particles allows them to avoid interactions before their decay, leading to a harder spectral slope of this component. Until now, this “prompt” component has not been observed, but limits from data have been placed by previous IceCube analyses [6, 7, 8]. As in previous iterations of this analysis, we use the limit set by an analysis of upgoing muons from muon neutrinos in the 59-string configuration of IceCube [6] for purposes of background estimation. Newer limits are available and will be used in future IceCube analyses of this data sample and extensions of it. Note that some of the down-going atmospheric neutrino background will be vetoed because of accompanying muons from the same air shower. This reduces the background from atmospheric neutrinos in the Southern Sky. This analysis uses the veto probabilities as described in [7]. The total number of expected background events from atmospheric neutrinos in six years of data is  $15.6_{-3.9}^{+11.4}$  (accounting for an unknown “prompt” component at or below the upper limit measured in [6]).

#### 4. Diffuse Flux Fit

In the full 2078-day sample, we detect 82 events (Fig. 1); 20 of them are observed in the fifth and 8 in the sixth year, respectively (see table 1). Event number 32, observed in the third year and event number 55 in the fifth year were produced by a coincident pair of background muons from unrelated cosmic ray air showers and have been excluded from the analysis.

In order to describe the data, we perform a likelihood fit of all expected components (atmospheric muons, atmospheric neutrinos from  $\pi$ /K decay, atmospheric neutrinos from charm decay and an astrophysical flux assuming a 1:1:1 flavor ratio). The fit is performed in the energy range of  $60 \text{ TeV} < E_{\text{dep}} < 10 \text{ PeV}$ , which is an extended range compared to [4] to include the Glashow resonance in the prediction. Due to the non-observation of events in this extended energy range the effect on the fit result is negligible. The neutrino interaction model was updated from previous iterations of this analysis by using corrected charged- and neutral-current cross-sections [9], resulting in an approximately 25% decrease in best-fit normalization.

As in previous iterations of this analysis, we fit an unbroken power-law spectrum with a variable spectral index,  $E^{-\gamma}$ . The best fit yields a spectral index of  $-2.92_{-0.29}^{+0.33}$ . We note that all of the events in the recent two years have energies below 200 TeV, resulting in a softening of the spectrum compared to previous results [2, 3, 4]. However, due to the large uncertainties these results are still compatible within  $2\sigma$ . Furthermore, this result remains compatible with other IceCube results such as the high-energy upgoing muon neutrino sample [10], from here on called  $\nu_{\mu,up}$ , because of their limited energy range starting at a neutrino energy of around 120 TeV. This is illustrated in Fig-



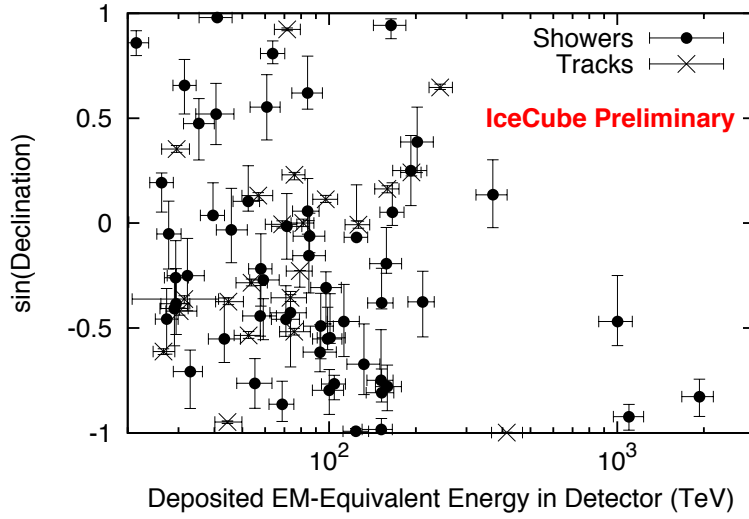


Figure 1: Arrival angles and electromagnetic-equivalent deposited energies of the events. Track-like events are indicated with crosses whereas shower-like events are shown as filled circles. The error bars show 68% confidence intervals including statistical and systematic errors. Deposited energy as shown here is always a lower limit on the primary neutrino energy.

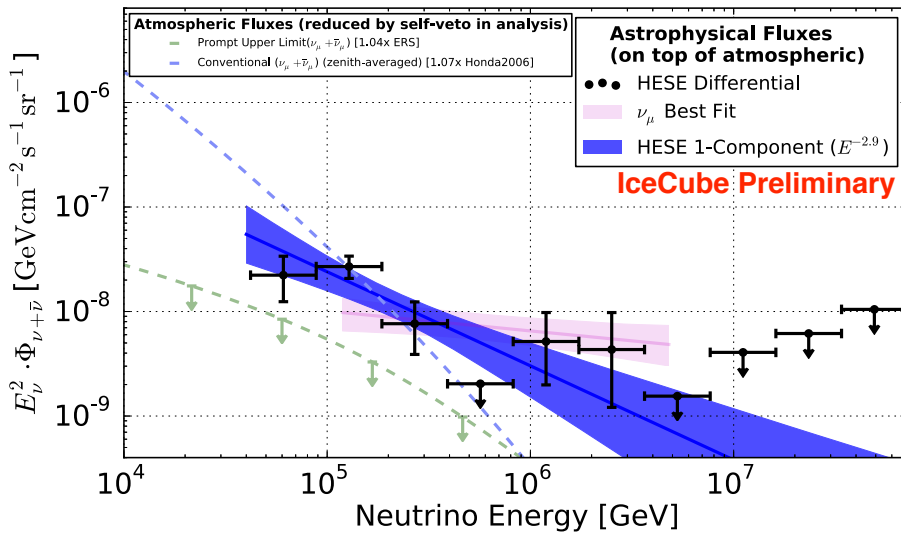


Figure 2: Best-fit per-flavor neutrino flux results (combined neutrino and anti-neutrino) as a function of energy. The black points with  $1\sigma$  uncertainties are extracted from a combined likelihood fit of all background components together with an astrophysical flux component with an independent normalization in each energy band (assuming an  $E^{-2}$  spectrum within each band). The atmospheric neutrino and muon fluxes are already subtracted. The best-fit conventional flux and the best-fit upper limit on “prompt” neutrinos are shown separately, not taking into account the effect of the atmospheric self-veto, which will significantly reduce their contribution. The blue band shows the  $1\sigma$  uncertainties on the result of a single power-law fit to the HESE data. The pink band shows the  $\nu_{\mu,up}$  best fit [10] with  $1\sigma$  uncertainties. Its length indicates the approximate sensitive energy range of the  $\nu_{\mu,up}$  analysis.

Table 1: Properties of the events observed in the fifth and sixth year. A list of events 1-37 can be found in [3], and events 38-54 in [4], respectively. The  $E_{\text{dep}}$  column shows the electromagnetic-equivalent deposited energy of each event. ‘‘Ang. Err.’’ shows the median angular error including systematic uncertainties.

ID	$E_{\text{dep}}$ (TeV)	Time (MJD)	Decl. (deg.)	R.A. (deg.)	Ang. Err. (deg.)	Topology
55	---	56798.73029	---	---	---	Coincident
56	$104.2^{+9.7}_{-10.0}$	56817.38958	-50.1	280.5	6.5	Shower
57	$132.1^{+18.1}_{-16.8}$	56830.52665	-42.2	123.0	14.4	Shower
58	$52.6^{+5.2}_{-5.7}$	56859.75882	-32.4	102.1	<1.3	Track
59	$124.6^{+11.6}_{-11.7}$	56922.58530	-3.9	63.3	8.8	Shower
60	$93.0^{+12.9}_{-11.7}$	56931.93110	-37.9	32.7	13.3	Shower
61	$53.8^{+7.2}_{-6.3}$	56970.20736	-16.5	55.6	<1.2	Track
62	$75.8^{+6.7}_{-7.1}$	56987.77219	13.3	187.9	<1.3	Track
63	$97.4^{+9.6}_{-9.6}$	57000.14311	6.5	160.0	<1.2	Track
64	$70.8^{+8.1}_{-7.7}$	57036.74378	-27.3	144.5	10.6	Shower
65	$43.3^{+5.9}_{-5.2}$	57051.66378	-33.5	72.8	17.5	Shower
66	$84.2^{+10.7}_{-9.9}$	57053.12727	38.3	128.7	18.3	Shower
67	$165.7^{+16.5}_{-15.5}$	57079.96532	3.0	335.7	7.0	Shower
68	$59.1^{+8.0}_{-6.0}$	57081.53526	-15.7	294.3	11.7	Shower
69	$18.0^{+2.2}_{-2.0}$	57133.79007	0.3	236.2	15.7	Shower
70	$98.8^{+12.0}_{-11.1}$	57134.39812	-33.5	93.9	12.3	Shower
71	$73.5^{+10.0}_{-10.5}$	57140.47276	-20.8	80.7	<1.2	Track
72	$35.3^{+4.6}_{-4.1}$	57144.29607	28.3	203.2	19.5	Shower
73	$26.2^{+2.6}_{-2.3}$	57154.83679	11.1	278.4	6.9	Shower
74	$71.3^{+9.1}_{-8.1}$	57157.00077	-0.9	341.0	12.7	Shower
75	$164.0^{+20.7}_{-21.4}$	57168.40450	70.5	259.0	13.1	Shower
76	$126.3^{+12.0}_{-12.7}$	57276.56530	-0.4	240.2	<1.2	Track
77	$39.5^{+3.8}_{-3.7}$	57285.01732	2.1	278.4	7.2	Shower
78	$56.7^{+7.0}_{-6.9}$	57363.44233	7.5	0.4	<1.2	Track
79	$158.2^{+20.3}_{-19.8}$	57365.75249	-11.1	24.6	14.6	Shower
80	$85.6^{+11.1}_{-10.6}$	57386.35877	-3.6	146.6	16.1	Shower
81	$151.8^{+13.9}_{-21.6}$	57480.64736	-79.4	45.0	13.5	Shower
82	$159.3^{+15.5}_{-15.3}$	57505.24482	9.4	240.9	<1.2	Track

ure 2 where we compare the  $\nu_{\mu,up}$  best-fit in its approximate sensitive energy range with the HESE data. The seemingly large differences in the best-fit slopes could suggest a break in the power-law spectrum arising from, e.g., a second harder astrophysical component. This possibility has been previously investigated using 4 years of HESE data [12]. Here, we performed a fit to the HESE 6-year dataset introducing a second astrophysical component, described by a power-law with an independent spectral index. A likelihood-ratio test comparing the single power-law fit with the two power-law fit gives a p-value of 37%. Thus, the HESE sample is not sufficient to distinguish between these models. In a second step, we used the mostly independent<sup>2</sup>  $\nu_{\mu,up}$  best-fit astrophysical flux with  $1\sigma$  uncertainties (contour in spectral index and normalization) as a prior for the

<sup>2</sup>There is some overlap between the two samples in that some of the track-like HESE events also appear in the  $\nu_{\mu,up}$  selection.

high-energy (“hard”) component of the HESE two power-law fit. The results are shown in Fig. 3, together with the single power-law fit. A non-zero second component with a softer spectrum is then preferred by the likelihood fit. Due to the large uncertainties on this low-energy (“soft”) component it is compatible with zero within about  $2\sigma$  in which case the fit reduces to a single astrophysical component. A corresponding likelihood ratio test comparing the single power-law fit with the two power-law fit using the independent  $\nu_{\mu,\nu\tau}$  measurement as a prior yields a p-value of 1.5%. Despite the strong prior, there is no clear evidence for a break in the astrophysical spectrum in the HESE data. Future IceCube analyses to be presented later this year, using samples extending to lower

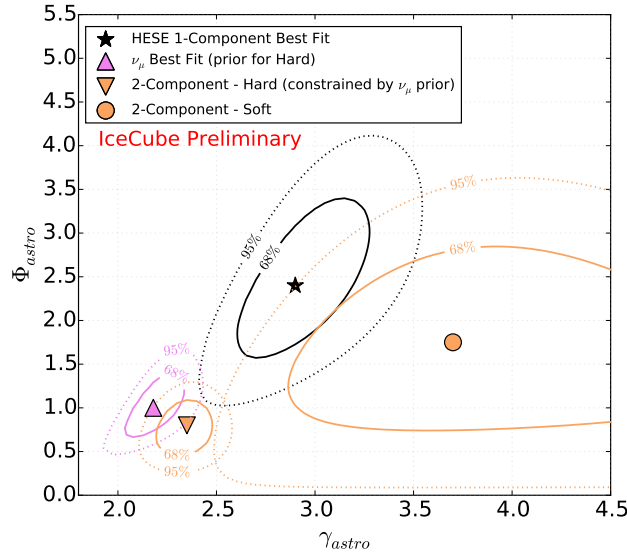


Figure 3: Contour plot of the best-fit astrophysical spectral index  $\gamma_{\text{astro}}$  vs. best-fit per-flavor normalization at 100TeV,  $\Phi_{\text{astro}}$ . Shown is the single power-law fit in black (“1-Component”), where the best-fit point is marked with a black star. The best-fit power law is  $E^2\phi(E) = 2.46 \pm 0.8 \times 10^{-8} (E/100\text{TeV})^{-0.92} \text{GeVcm}^{-2}\text{s}^{-1}\text{sr}^{-1}$ . The orange contours show the best-fit components assuming a two power-law hypothesis with the  $\nu_{\mu,\nu\tau}$  best fit [10], shown in pink, as a prior for the hard component. Due to the large uncertainties on the soft component it is compatible with zero within  $\approx 2\sigma$ , in which case the fit reduces to a single astrophysical component.

energies and incorporating multiple channels, will have improved sensitivity to a possible break in the astrophysical spectrum. Distributions of the HESE data events compared to background and best-fit signal expectations for the above described single and two power-law model fits as functions of deposited energy and declination can be found in figures 4a and 4b, respectively.

## 5. Spatial Clustering

A maximum-likelihood clustering method [3] was used to look for any neutrino point source in the sample. The test statistic (TS) was defined as the logarithm of the ratio between the maximal likelihood including a point source component and the likelihood for the isotropic null hypothesis. The significance of our observed TS was determined by comparing to maps scrambled in right ascension. As before, the analysis was run twice, once with all events and once with only shower-

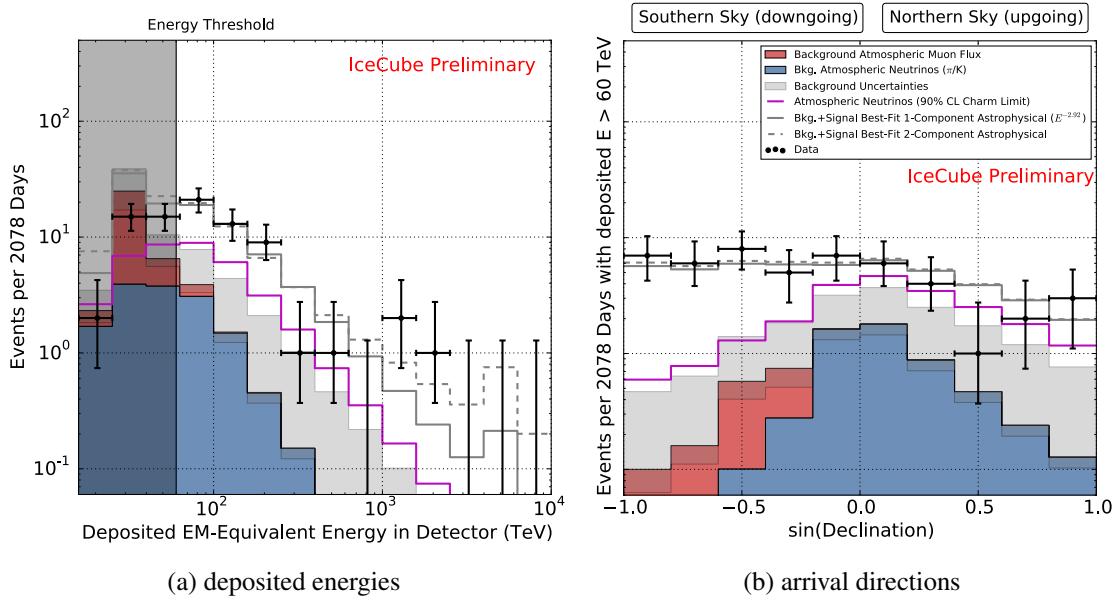


Figure 4: Deposited energies and arrival directions of the observed events and expected contributions from backgrounds and astrophysical neutrinos. Atmospheric muon backgrounds (estimated from data) are shown in red. Atmospheric neutrino backgrounds are shown in blue with  $1\sigma$  uncertainties on the prediction shown as a gray band. For scale, the 90% CL upper bound on the charm component of atmospheric neutrinos is shown as a magenta line. The best-fit astrophysical spectra (assuming an unbroken power-law model) are shown in gray. The solid line assumes a single power-law model, whereas the dashed line assumes a two power-law model, using the spectrum derived in [10] as a prior for the high-energy component. Only events above 60 TeV are considered in the fit.

like events in the sample. We removed events 32 and 55 (two coincident muons from unrelated air showers) and 28 (event with sub-threshold hits in the IceTop array) for purposes of all clustering analyses. This test (see Fig. 5) did not yield significant evidence of clustering with p-values of 44% and 77% for the shower-only and the all-events tests, respectively. We also performed a galactic plane clustering test using a fixed width of  $2.5^\circ$  around the plane (p-value 23.4%) and using a variable-width scan (p-value 17.4%). All above p-values are corrected for trials.

## 6. Future Plans

Modified analysis strategies in IceCube have managed to reduce the energy threshold for a selection of starting events even further in order to be better able to describe the observed flux and its properties [7], but at this time they have only been applied to the first two years of data used for this study. Corresponding lower-threshold datasets, using the full set of data collected by IceCube will become available soon [11]. In addition, combined fits of this dataset and others like the through-going muon channel [10] are currently in preparation [11].

Due to the simplicity and robustness of this search with respect to systematics when compared to more detailed searches, it is well suited towards triggering and providing input for follow-up

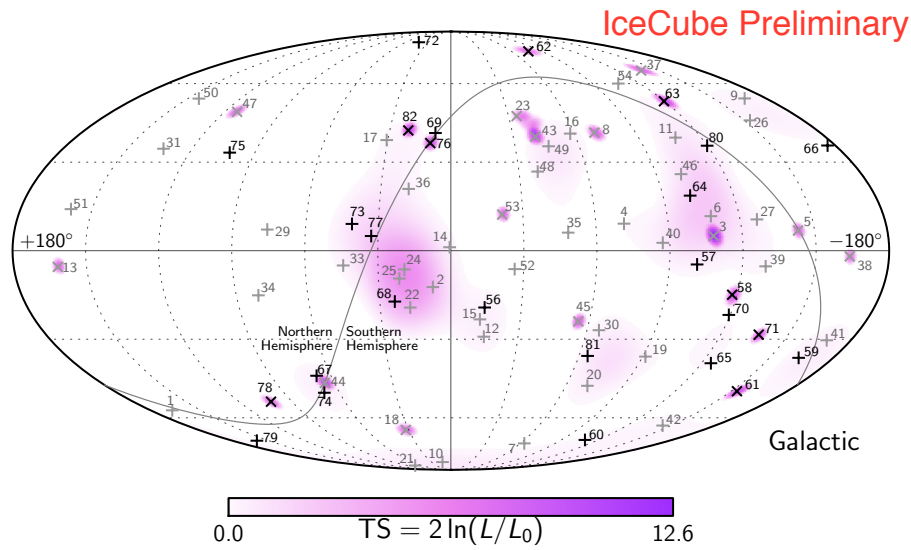


Figure 5: Arrival directions of the events in galactic coordinates. Shower-like events are marked with a + and those containing tracks with a ×. The new events of table 1 are shown in black. Colors show the test statistics (TS) for the point-source clustering test at each location. No significant clustering was found.

observations by other experiments. IceCube is already sending public alerts using the HESE channel for track-like events [13] with the plan to extend this to the full HESE selection including cascade-like events soon.

## References

- [1] **IceCube** Collaboration, M. G. Aartsen et al., *JINST* **12** (2017) P03012
- [2] **IceCube** Collaboration, M. G. Aartsen et al., *Science* **342**, 1242856 (2013)
- [3] **IceCube** Collaboration, M. G. Aartsen et al., *PRL* **113** (2014) 101101
- [4] **IceCube** Collaboration, *PoS (ICRC2015)* 1081 (2016)
- [5] **IceCube** Collaboration, *PoS (ICRC2017)* 974 (these proceedings)
- [6] **IceCube** Collaboration, M. G. Aartsen et al., *PRD* **89** (2014) 062007
- [7] **IceCube** Collaboration, M. G. Aartsen et al., *PRD* **91** (2015) 022001
- [8] **IceCube** Collaboration, M. G. Aartsen et al., *ApJ* **833** (2016) 1
- [9] A. Cooper-Sarkar, P. Mertsch & S. Sarkar, *JHEP* **08** (2011)042
- [10] **IceCube** Collaboration, *PoS (ICRC2017)* 1005 (these proceedings)
- [11] **IceCube** Collaboration, *PoS (ICRC2017)* 976 (these proceedings)
- [12] A. C. Vincent, S. Palomares-Ruiz, O. Mena, *PRD* **94** (2016) 023009
- [13] **IceCube** Collaboration, M. G. Aartsen et al., *Astropart. Phys.* **92** (2017) 30-41

# 1 All-flavor Multi-Channel Analysis of the 2 Astrophysical Neutrino Spectrum with IceCube

---

## The IceCube Collaboration<sup>†</sup>

<sup>†</sup> [http://icecube.wisc.edu/collaboration/authors/icrc17\\_icecube](http://icecube.wisc.edu/collaboration/authors/icrc17_icecube)

E-mail: [cweaver@icecube.wisc.edu](mailto:cweaver@icecube.wisc.edu), [nwandkowsky@icecube.wisc.edu](mailto:nwandkowsky@icecube.wisc.edu)

The spectral shape and flavor composition of the high-energy astrophysical neutrino flux can contain important information about the sources and processes which produce it. The IceCube Neutrino Observatory has previously demonstrated the ability to observe neutrinos of all flavors by selecting events which interact within the detector volume. Sensitivity to charged current muon neutrino interactions in or close to the detector has also been shown by selecting muon track events whose directions indicate passage through the Earth. We present an updated analysis of starting events using 6 years of IceCube data taken from 2010–2016 focusing on energies from the PeV region down to 1 TeV, far below the threshold of the original data sample used in the initial discovery of the astrophysical flux. Astrophysical neutrinos remain the dominant component in the southern sky down to 10 TeV. We then also perform a unified analysis of the flavor and spectrum implications of this sample when combined with the recently published data on  $\nu_\mu$  induced muon tracks as well as recent work to identify candidate  $\nu_\tau$  events.

**Corresponding authors:** N. Wandkowsky<sup>1</sup>, C. Weaver<sup>\*2</sup>

<sup>1</sup>*Dept. of Physics and Wisconsin IceCube Particle Astrophysics Center, University of Wisconsin, Madison, WI 53706, USA*

<sup>2</sup>*Dept. of Physics, University of Alberta, Edmonton, Alberta, Canada T6G 2E1*

*35th International Cosmic Ray Conference – ICRC217-  
10-20 July, 2017  
Bexco, Busan, Korea*

---

\*Speaker.

## 3 1. Introduction

4 Neutrinos have the potential to provide important information for understanding the mecha-  
5 nisms of energetic astrophysical objects and their relationship to cosmic rays. With the successful  
6 observation of a diffuse flux of astrophysical neutrinos, both in the form of events starting within  
7 a fiducial volume of a detector [2, 5] and events with Earth-crossing directions [3], a major goal is  
8 now to determine the properties of this flux in the greatest possible detail. This can be pursued both  
9 by extending the selection of neutrino candidate events to capture as many astrophysical neutrinos  
10 as possible, including substantial numbers of atmospheric neutrinos to ensure that backgrounds are  
11 well understood, and by combining different selection techniques into more thoroughly integrated  
12 analyses of the total spectrum. Here, we discuss both improvement of the selection of starting  
13 events in the IceCube detector and a new iteration of a global analysis of the neutrino flux utilizing  
14 the latest high statistics datasets and event observables.

## 15 2. Starting Event Selection

16 Identifying of neutrino candidate events in IceCube by utilizing a division of the detector into  
17 an internal fiducial volume and a surrounding veto layer has proven highly successful in obtaining  
18 a high purity sample of neutrinos. Additionally, a large fraction of these neutrinos are expected to  
19 be of astrophysical origin. Because the development of this technique was spurred by the observa-  
20 tion of events in the PeV range of energy [1], the initial focus was on these high energies. Lower  
21 energies, where backgrounds produced by cosmic ray air showers pose a greater challenge, were  
22 left unexplored. Subsequently, the veto technique has been extended, using additional event recon-  
23 struction information and dynamic scaling of the boundary between the fiducial and veto volumes.  
24 This lowers the selection threshold to events depositing around 1 TeV of energy [5], but thus far  
25 this enhanced technique has been applied to only two years of IceCube data. This new version of  
26 the selection further optimizes this technique to maximize efficiency. A splitting algorithm, using  
27 a form of agglomerative hierarchical clustering, is applied to each recorded event to attempt to  
28 separate unrelated, coincident events in the detector, with a success rate of about 75%. The ‘outer  
29 layer’ veto criterion as in [1] is then applied, rejecting all events which are observed to have more  
30 than three detected photons in the veto region. The splitting reduces the fraction of events falsely  
31 vetoed due to coincident events and makes this selection a superset of the selection of [1] for events  
32 which yield at least 6000 photoelectrons detected.

33 To provide efficient background rejection for lower energy events, following the technique of  
34 [5], a more sensitive veto for incoming particle tracks is then applied, relying on the reconstruction  
35 of the location of the interaction vertex (or a major energy deposition within the event) followed  
36 by a search over downward directions for detected photons whose timing is consistent with an in-  
37 coming particle. Any event with more than two such veto photons is discarded. This same veto  
38 method is also applied in reverse to detect tracks directed outward and upward from the recon-  
39 structed event vertex, as such a track is a strong indication that the event is a charged-current  $\nu_\mu$   
40 interaction. Events with at least 10 photoelectrons consistent with an upward track are immediately  
41 preserved. Finally, events which produce lower observed numbers of photons are subjected to a  
42 volume cut, more stringent with decreasing energy, increasing the amount of veto path length which



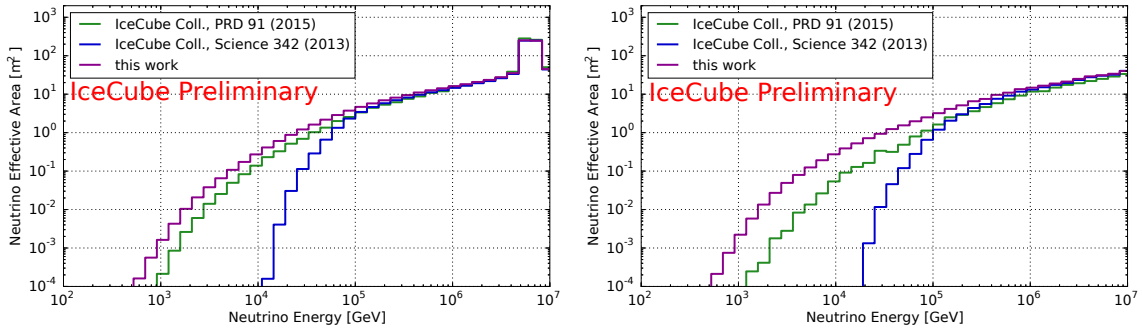


**Figure 1:** Effective area of the starting event selection for  $\nu_e$  (left panel) and  $\nu_\mu$  (right panel) is shown in purple, compared to the effective areas from [1] in blue and [5] in green. All effective areas are averaged over neutrinos and antineutrinos. The effective area for  $\nu_\tau$  is quite similar to that for  $\nu_e$  except for the lack of the resonance feature at several PeV.

43 a background muon would have to traverse unseen. An important change with respect to [5] is that  
 44 to avoid discrimination against starting charged-current  $\nu_\mu$  interactions that produce more clearly  
 45 track-like events, a broader selection using data from IceCube’s first-level ‘online’ filters gives a  
 46 considerable increase in the efficiency with which these events are selected. Fig. 1 shows the result-  
 47 ing effective area for this selection compared to the previous veto-based selections. This selection  
 48 delivers higher efficiency for all event topologies, particularly a factor  $\sim 2$  for  $\nu_\mu$  at around 100  
 49 TeV to a factor of  $\sim 8$  at around 10 TeV. Further, it is intended that this selection will be applied to  
 50 the same six years of IceCube data as in [4], three times the data-taking period covered by [5], and  
 51 it is anticipated that this will continue to be extended in future as new data become available.

52 As this selection collects events of both track-like and cascade-like topologies, it is useful to  
 53 distinguish between the two. Events with 10 photoelectrons of out-going light attributable to an  
 54 up-going track are naturally classified as track-like. Otherwise, each event is reconstructed using  
 55 both track and cascade hypotheses, and the average distance of the modules which observed light  
 56 to the best fit particles is computed. This provides a useful observable because true track events  
 57 tend to have light at large distances from the best fit cascade hypothesis. Finally, an unfolding  
 58 of the probable energy depositions within each event is performed, using both a single, point-like  
 59 deposition hypothesis, representing a cascade, and a hypothesis of a linear collection of deposi-  
 60 tions, representing a muon. For bright events with more than 6000 photoelectrons detected, if the  
 61 linear unfolding has non-negligible depositions located more than 500 meters apart, the event is  
 62 considered track-like. Likewise, bright events for which the observed charge associated with the  
 63 linear unfolding is larger than the observed charge associated with the single point unfolding are  
 64 classified as tracks; other bright events are classified as cascades. For dimmer events, if at least 1.5  
 65 photoelectrons of out-going charge are detected the event is classified as track-like, and otherwise  
 66 it is considered cascade-like. Based on Monte-Carlo simulations, more than 98% of truly cascade-  
 67 like events are correctly classified as such. Figure 2 shows the success rate for classification of  
 68 true  $\nu_\mu$  charged-current events, which is above 80% when averaged over energy and position for  
 69 an astrophysical spectrum  $\propto E^{-2.5}$ . Misclassified  $\nu_\mu$  charged-current events are expected to make  
 70 up 30% of the cascade-like category from a conventional atmospheric spectrum, but only 5% from  
 71 a spectrum  $\propto E^{-2.5}$ .

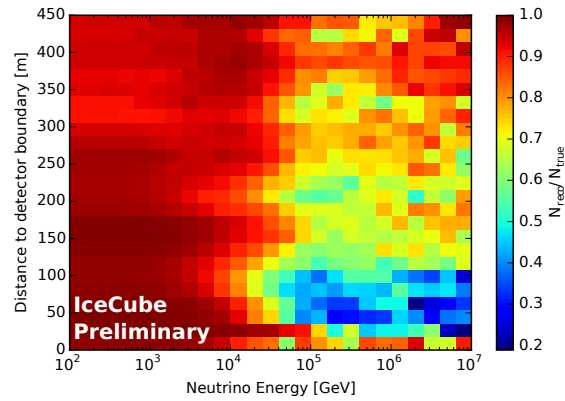


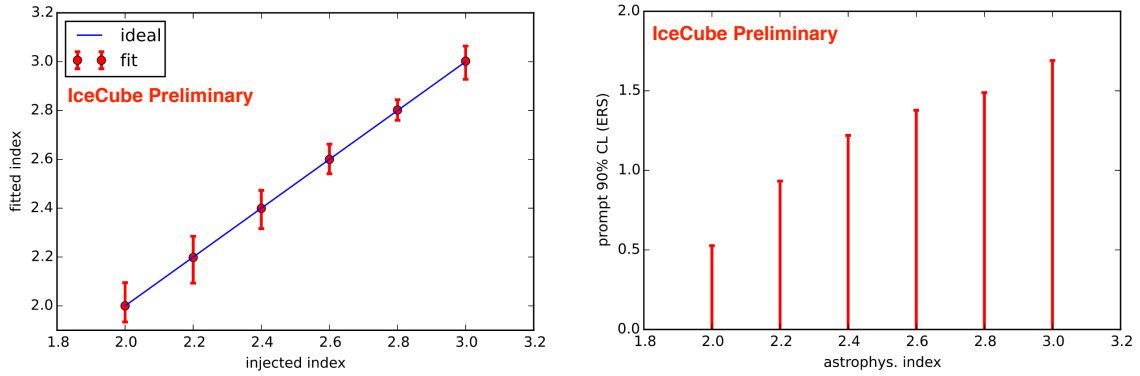
**Figure 2:** Probability that starting  $\nu_\mu$  charged-current events are correctly classified as track-like. Since the selection requires lower energy events to start deeper inside the detector, these are more likely to be correctly classified due to having an observation of the out-going track.

### 72 3. Starting Event Analysis

73 A new sample of starting neutrino events provides opportunities for studying the diffuse neu-  
 74 trino flux. These data will be analyzed using a binned, forward-folding maximum likelihood fit to a  
 75 set of parameterized models, as in many previous analyses. Three observables are used in the likeli-  
 76 hood fit. The reconstructed event energy gives access to spectral shape information. Reconstructed  
 77 event direction (zenith angle in detector coordinates) carries information about atmospheric origin  
 78 due to non-uniform production of atmospheric neutrinos from light meson decays (‘conventional’  
 79 atmospheric neutrinos) and the self-veto effect of muons produced in the same air showers. Last,  
 80 the assessed event topology gives the analysis a degree of flavor sensitivity. In terms of the model  
 81 which will be used to fit the data, four spectral components will be included: the conventional atmo-  
 82 spheric neutrinos, ‘prompt’ atmospheric neutrinos (from short-lived particle decays), penetrating  
 83 muons from cosmic ray air showers, and a diffuse, astrophysical flux of neutrinos.

84 The three atmospheric components are each allowed to vary in normalization. No prior is  
 85 placed on the normalization of the conventional component as it is expected to be well constrained  
 86 by the data, the prompt component is given a gaussian prior centered at zero with a width of 2.3  
 87 times the ERS model normalization [6] following the result obtained in [7], and the penetrating  
 88 muons are given a prior centered at the rate estimated from a tagged sample of experimental back-  
 89 ground events with a width of 50% [2]. These priors are expected to have only weak influence on  
 90 the final result. In addition, to treat systematic uncertainties arising from the primary cosmic ray  
 91 flux and from the modeling of hadronic interactions in air showers, parameters will be included for  
 92 variation in the effective cosmic ray spectral index and the relative production rates of kaons with  
 93 respect to pions in air showers. Systematic treatment of uncertainties in the response of the detector  
 94 itself will also be addressed, specifically the absolute optical efficiency of the detector, the optical  
 95 properties of the ice surrounding the modules, and the scattering of the ice which was melted and  
 96 refrozen during installation of the instrumentation.

97 For the purposes of this study, the astrophysical neutrinos are assumed to be isotropic and  
 98 have equal contributions from all neutrino flavors. The base model to be tested will be a single



(a) 68% sensitivity to spectral index of a single astrophysical power law flux

(b) 90% sensitivity to a prompt atmospheric neutrino flux assuming the spectrum of ERS [6] relative to the normalization of that model

**Figure 3:** Median projected sensitivity of the starting event analysis to model parameters assuming 6 years of data. A variety of spectral indices are considered to ensure that the analysis performs well for any possible input.

99 power law with variable normalization and spectral index. Additionally, a set of more advanced  
 100 astrophysical models will be tested, including an exponential spectral cutoff, a second power law  
 101 component, and the combination of both of these additions. Finally, the flavor composition of the  
 102 astrophysical flux will be tested by allowing the normalization associated with each neutrino flavor  
 103 to float independently in the fit, although all three flavors will be assumed to have the same spectral  
 104 shape. Fig. 3 shows the expected median sensitivity of this analysis for two of the parameters  
 105 considered over a variety of possible true astrophysical fluxes with different spectral indices and  
 106 normalizations chosen to be consistent with the observations of [2]. This analysis is expected to  
 107 have good resolution of the spectral index of a single astrophysical power law component, but the  
 108 sensitivity to a prompt atmospheric component is expected to be limited by the strength (and also  
 109 uncertainty) of the astrophysical flux, particularly if that flux is relatively soft.

#### 110 4. Global Flavor Analysis

111 Beyond analyzing the more complete dataset of starting events, it is desirable to unify the  
 112 analysis of all types of neutrino data observed by IceCube. This type of analysis has been per-  
 113 formed previously [8]; the purpose of this new iteration is to use newer datasets and observables  
 114 which have become available. Particularly complementary to the starting event sample is the high  
 115 statistics sample of muons from Earth crossing neutrinos analyzed previously [3], and continues  
 116 to be extended to newer data [10]. While the starting event selection is most sensitive to the as-  
 117 trophysical neutrino flux in the southern portion of the sky, as this is the angular region in which  
 118 atmospheric neutrinos are most strongly self-vetoed, the Earth-crossing neutrinos are most sen-  
 119 sitive to high energy events near the horizon. Consisting almost entirely of  $\nu_\mu$  charged-current  
 120 events, the Earth-crossing sample has essentially no flavor sensitivity on its own, but provides a  
 121 strong constraint on the  $\nu_\mu$  portion of the astrophysical flux. The starting event sample constrains  
 122 the combined flux of  $\nu_e$  and  $\nu_\tau$  in addition to contributing to the  $\nu_\mu$  measurement. In fact, it is

123 possible to do better than treating  $\nu_e$  and  $\nu_\tau$  as equivalent cascade-like events by using specialized  
124 reconstruction for double cascade events resulting from  $\nu_\tau$  charged-current interactions as detailed  
125 in [9]. Some care must be taken when combining these three datasets to avoid double counting  
126 events. Since the  $\nu_\tau$  component is the least well constrained, the  $\tau$  observables only function well  
127 for high energy events, and the starting event and  $\nu_\tau$  analysis samples are nearly equivalent at the  
128 energies where they overlap, the  $\nu_\tau$  optimized sample is given the highest priority. Events passing  
129 the  $\nu_\tau$  optimized selection are treated using its topology classification scheme: For events classified  
130 as single cascades and tracks, deposited energy and zenith angle are used as observables, while for  
131 those classified as double cascades, tau length and decay energy observables are used. It would be  
132 desirable to use the total deposited energy and direction observables for the double cascade events,  
133 but it appears that doing so would involve dividing the data into too many bins for the amount of  
134 simulated data currently available to provide precise model expectations in all bins. The remaining  
135 events of the new, high statistics starting event sample are then included using the same observables  
136 as in the analysis of that sample alone. Finally, the Earth-crossing muons are included in the fit,  
137 omitting those starting muon events which were already selected by the starting sample. Muon  
138 zenith angles and reconstructed muon energies are used for fitting, as in [3]. After de-duplication  
139 of the input data, events are classified by topology: Single cascade, double cascade, starting track,  
140 or through-going track, depending on either the topology classification of the source dataset, or by  
141 treating the entire dataset as a topology category in the case of the through-going muons remaining  
142 in the Earth-crossing dataset after the starting events are removed. The topology categories do not  
143 all map to single neutrino flavor, nor are the classifications always correct. These limitations are  
144 encompassed by the Monte Carlo simulated data, which include all neutrino flavors and interac-  
145 tion process relevant in the energy range of the analysis, and which are processed and classified  
146 in exactly the same manner as the observed experimental data. Furthermore, a new feature of this  
147 analysis is use of a consistent set of simulated data for fitting all observations, ensuring that sys-  
148 tematic effects will be accounted for in a consistent manner. This is planned to coincide with a  
149 reprocessing of IceCube data over the time period to be used which will bring old data up to the  
150 same standard as the most recent data-taking periods, eliminating season to season variations from  
151 software changes, removing the need for complex treatment to fit these differences out.

152 The analysis fit will be performed using the same method as the starting event only analysis,  
153 and as such the same model parameters will be included. However, as the primary goal of this  
154 combined analysis is the flavor composition, all fits will be performed with the three flavor com-  
155 ponents of the astrophysical flux allowed to float to distinct normalizations. Additionally, allowing  
156 the fitted fraction of neutrinos to vary with respect to the fraction of anti-neutrinos has been ex-  
157 plored using Monte-Carlo studies. While this analysis would have some ability to constrain such a  
158 parameter, due to resonant  $W^-$  production by high energy  $\bar{\nu}_e$  interacting with electrons in the Earth  
159 (the Glashow resonance) and small changes to the absorption of the flux in the Earth due to the dif-  
160 ference between neutrino and antineutrino cross sections, the sensitivity does not appear to be great  
161 enough to be useful at this time, and it seems preferable to continue with the assumption of a flux  
162 with equal parts neutrinos and antineutrinos and keep this degree of freedom out of the fit. Fig. 4  
163 shows the projected sensitivity of this analysis using the three samples outlined above. Overall, the  
164 result is similar to the expectation for the  $\nu_\tau$  analysis of [9], but the inclusion of the Earth-crossing  
165 muons considerably reduces uncertainty on the  $\nu_\mu$  fraction. Fig. 5 shows the ability of this analysis

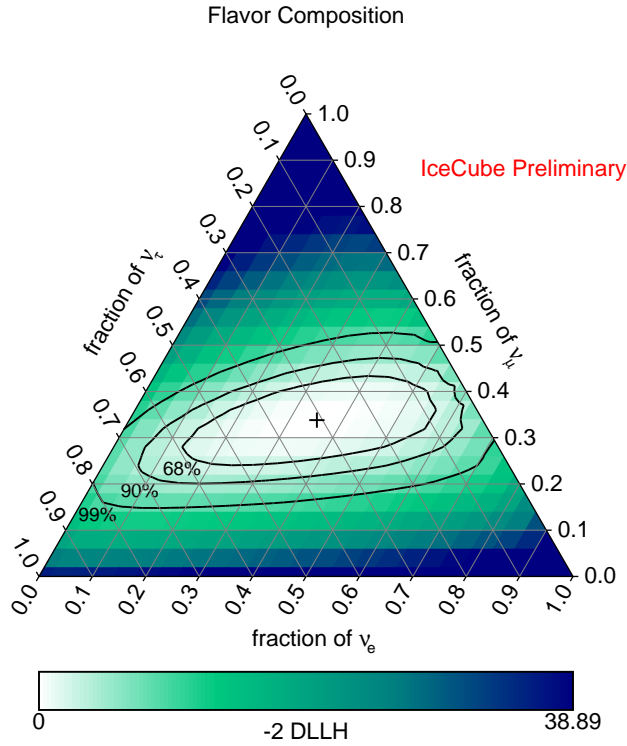


**Figure 4:** Median sensitivity of the global analysis to an astrophysical neutrino flux of  $\Phi(E_\nu) = 1.5 \times 10^{-18} \text{ GeV}^{-1} \text{ cm}^{-2} \text{ sr}^{-1} \text{ s}^{-1} (E_\nu/100 \text{ TeV})^{-2.3}$  per flavor. This plot shows the profile likelihood space for the flavor composition with the total flux normalization allowed to float freely. The sensitivity does not change substantially for other spectra which are statistically consistent with previous observations.

166 to constrain an exponential cutoff in the astrophysical spectrum under various scenarios. A cutoff  
 167 can be constrained, except for soft spectra where it becomes impossible to distinguish due to the  
 168 expected number of high energy events being very small whether the cutoff is present or not.

## 169 5. Future Extensions

170 Besides the three samples currently integrated into the combined fit, several other data sets are  
 171 complete or nearing completion which can enhance the sensitivity of this analysis. The cascade  
 172 selection of [11] uses different techniques to select starting events and demonstrated to have a large  
 173 fraction of events which do not appear in the starting sample offers the opportunity to substantially  
 174 increase the statistics for cascade events. In addition, the selection for cascade event which are not  
 175 fully contained within the detector [12] will add events not included in either of the contained event  
 176 selections. Similar gains may be possible for  $\nu_\tau$  candidate events; [13] represents a completely dif-  
 177 ferent paradigm for identifying double cascades, which is expected to have very different strengths  
 178 and weaknesses, and is therefore likely to be a good complement to [9]. Finally, new veto-based  
 179 techniques for selecting additional starting track events [14] may further enhance the number of  
 180 astrophysical neutrinos which can be collected with highly down-going directions. As many of  
 181 these data sets as possible are planned to be included to form a truly global analysis, along with

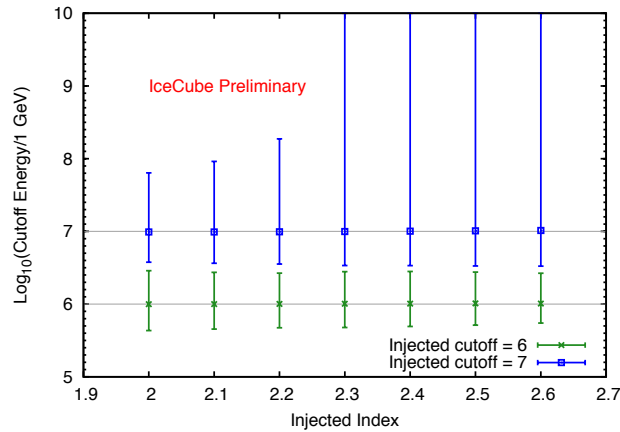


**Figure 5:** Median sensitivity of the global analysis to the energy of an exponential cutoff in the astrophysical neutrino spectrum. Error bars show 68% uncertainty intervals for the fitted cutoff. The extension of these intervals to energies far larger than any event expected to be observed in data for soft spectra indicates an inability to distinguish the injected cutoff from a case with no cutoff.

182 any other new selections and observables which may become available in the near future. Further-  
 183 more, this type of analysis will benefit from improved calibration which will become possible with  
 184 IceCube-Gen2.

## 185 References

- 186 [1] M.G. Aartsen et al., *Science* **342**, 1242856 (2013)  
 187 [2] R. Abbasi et al., *Phy. Rev. Lett.* **111** 021103 (2013)  
 188 [3] M. G. Aartsen et al., *ApJ* **833**, 1 (2016)  
 189 [4] **IceCube** Collaboration, *PoS (ICRC2017)* 981 (2017).  
 190 [5] M. G. Aartsen et al., *Phys. Rev. D* **91**, 022001 (2015)  
 191 [6] R. Enberg, M. H. Reno, and I. Sarcevic, *Phys. Rev. D* **78** 043005 (2008)  
 192 [7] M. G. Aartsen et al., *Phys. Rev. D* **89**, 062007 (2014)  
 193 [8] M. G. Aartsen et al., *ApJ* **809**, 1 (2015)  
 194 [9] **IceCube** Collaboration, *PoS (ICRC2017)* 974 (2017).  
 195 [10] **IceCube** Collaboration, *PoS (ICRC2017)* 1005 (2017).  
 196 [11] **IceCube** Collaboration, *PoS (ICRC2017)* 968 (2017).  
 197 [12] **IceCube** Collaboration, *PoS (ICRC2017)* 1002 (2017).  
 198 [13] **IceCube** Collaboration, *PoS (ICRC2017)* 1009 (2017).  
 199 [14] K. Jero, "Enhanced Starting Track Event Selection," Presentation at IPA Conference, May 8-10, 2017,  
 200 Madison, WI, USA

# Differential limit on an EHE neutrino flux component in the presence of astrophysical background from nine years of IceCube data

---

## The IceCube collaboration<sup>†</sup>

<sup>†</sup> [http://icecube.wisc.edu/collaboration/authors/icrc17\\_icecube](http://icecube.wisc.edu/collaboration/authors/icrc17_icecube)

E-mail: [syoshida@hepburn.s.chiba-u.ac.jp](mailto:syoshida@hepburn.s.chiba-u.ac.jp),

[aya@hepburn.s.chiba-u.ac.jp](mailto:aya@hepburn.s.chiba-u.ac.jp)

We report the quasi-differential upper limits of extremely high energy (EHE) neutrino flux above 10 PeV based on the analysis of nine years of IceCube data. A complete frequentist approach to calculate the differential limit using the Poisson binned likelihood is developed. It enables the limit to be set in the presence of unknown astrophysical neutrino flux. An event with deposited energy clearly above 1 PeV was detected in addition to one event found in the previous EHE neutrino search. They are consistent with the astrophysical neutrino flux of a power-law-like spectrum but incompatible with predictions of cosmogenic neutrino fluxes with spectrum peaks at energies well above the PeV range. Thus, they are considered as the bulk of background events in setting the limits on EHE neutrino fluxes. The resultant differential upper limit is the most stringent to date in the energy range between  $5 \times 10^6$  and  $5 \times 10^{10}$  GeV. This result indicates that cosmogenic neutrino models that predict a three-flavor neutrino flux of  $E_{\nu}^2 \phi_{\nu_e + \nu_{\mu} + \nu_{\tau}} \simeq 2 \times 10^{-8}$  GeV/cm<sup>2</sup> sec sr at  $10^9$  GeV are constrained, bounding a significant parameter space on EHE neutrino models, which assumes a composition of proton-dominated ultra-high-energy cosmic rays.

**Corresponding authors:** Shigeru Yoshida\*, Aya Ishihara

*Department of Physics, Graduate School of Science, Chiba University, Chiba 263-8522, Japan*

*35th International Cosmic Ray Conference — ICRC2017*

*10–20 July, 2017*

*Bexco, Busan, Korea*

---

\*Speaker.



## 1. Introduction

The upper limits of cosmic neutrino fluxes depend on their energy spectrum. The spectral shape of the neutrino flux is often assumed to follow a power-law form, that is,  $\phi_\nu \propto E_\nu^{-\alpha}$ . However, in the extremely high energy (EHE) region above 10 PeV, many neutrino models predict energy spectra that do not follow a simple power law. A cosmogenic Greisen–Zatsepin–Kuzmin (GZK) neutrino spectrum [1], for example, represents a non-power-law structure mostly determined by unknown physical parameters, such as cosmological source evolution, the spectrum and evolution function of extragalactic background light, and the energy spectrum of primary ultra-high-energy cosmic ray (UHECR) nucleons [2]. Variations in the spectral shapes present difficulties for setting a generic upper limit for neutrino fluxes in the EHE region. Thus, we present model-dependent constraints for a few representative models [3].

An approach to set a generic, model-independent limit on UHECR source models with EHE neutrino observations is to calculate the *differential* upper limit of the EHE neutrino flux. This idea was originally proposed by Anchordoqui et al. [4]. For null detection with the  $4\pi$ -averaged neutrino effective area  $A_i^\nu$  for a neutrino flavor  $i$ , this limit is calculated analytically by:

$$\phi_{\nu_e+\nu_\mu+\nu_\tau}^{\text{UL}}(E_\nu) = 3 \frac{N_{90}}{4\pi E_\nu T \text{Ln}10 \sum_{i=\nu_e, \nu_\mu, \nu_\tau} A_i^\nu(E_\nu)}, \quad (1.1)$$

where  $T$  is the observation time and  $N_{90}$  is a 90% CL upper limit on the number of events.  $N_{90} = 2.4$  with the Feldman–Cousins method [5] in the case of negligible background. An equal flavor ratio of neutrino fluxes:  $\nu_e : \nu_\mu : \nu_\tau = 1 : 1 : 1$  at the Earth is assumed. This formula is derived from the expected number of events in an energy bin with a width of one decade, where

$$\Delta N = \frac{1}{3} \phi_{\nu_e+\nu_\mu+\nu_\tau} 4\pi E_\nu T \text{Ln}10 \sum_{i=\nu_e, \nu_\mu, \nu_\tau} A_i^\nu(E_\nu). \quad (1.2)$$

This observation implies that the upper limit of Eq. (1.1) is equivalent to the limit on the normalization of the neutrino fluxes following  $E_\nu^{-1}$  with an interval of one decade.

In the case where neutrino event candidates are detected, this formula needs to be modified. However, the approach to incorporate detected events in the calculation of the differential limit is not obvious. This lack of clarity arises because the probability density function (PDF) of the primary neutrino energy for the measured energy of a given event is broadly distributed. In particular, only a small portion of the parent neutrino energy is deposited in the detector for a neutrino-induced muon track event. This PDF depends on the unknown true neutrino spectrum.

In this report, we present a complete frequentist approach to calculate the flux limits and update the constraints using a collection of IceCube data taken over nine years from April 2008 to May 2017. This data sample contains two years of the newest data in addition to that on which the previous analysis [3] was based. All signal selection criteria are the same as in the previous publication. Three events that passed the EHE neutrino search criteria were found in the final sample. Energy proxies and reconstructed zenith angles of these events are consistent with the astrophysical origin that IceCube has been detecting in the TeV to PeV energy region[6], but not with the GZK-like EeV-energy neutrinos. Thus, they are considered as *astrophysical* background in searches for cosmogenic neutrinos. The new approach using a nuisance parameter to represent

the unknown astrophysical background is described and the p-value calculations are carried out by a test statistic using the Poisson-binned likelihood ratio. The model-independent differential limits are presented. Lastly, the implications of the derived limits for explaining the origin of UHECRs are discussed.

## 2. Data and Simulation

IceCube is a cubic-kilometer neutrino detector installed in the ice at the geographic South Pole between depths of 1450 and 2450 m, forming a three-dimensional array of digital optical modules (DOMs)[7]. To form the detector, cable assemblies called strings were lowered into holes drilled downwards into the glacier ice with a horizontal spacing of approximately 125 m. The detector construction was completed in December 2010 and the observatory has been in full operation with 86 strings (IC86) since May 2011. During the construction period, it was partially operated with 40, 59, and 79 strings, in 2008-2009, 2009-2010, and 2010-2011, respectively. The analysis described here is based on data taken from April 2008 to May 2017. The effective live time of the sample was 3126 days. The newest two-year worth of data gives approximately 30% more exposure to the sample compared to that used in the previous EHE neutrino search [3].

There are two classes of atmospheric background events: atmospheric muon bundles, and events generated by atmospheric neutrinos. They were simulated using the CORSIKA [8] package with the SIBYLL hadronic interaction model [9], and by the IceCube neutrino-generator program based on the ANIS code [10], respectively. The EHE neutrino-induced events were simulated by the JULiE package [11]. This package provides the GZK cosmogenic signal simulation sample as well as simulations of the *astrophysical* background events, whose spectrum is assumed to be described by an unbroken power law in the relevant energy region. The detailed simulation procedure used in this work is described in Ref. [12].

The EHE signal selection criteria is the same as in the previous analysis [3]. They are designed to find any events yielding Cherenkov light bright enough to be distinguishable from the atmospheric background, regardless of event topology recorded by the array of DOMs. The expected number of atmospheric background events in the data sample passing the selection criteria is  $0.085^{+0.031}_{-0.051}$ . The expected event rate from the GZK cosmogenic model following the source evolution of the star formation rate (SFR) [15] is  $4.80^{+0.71}_{-1.05}$ . The astrophysical neutrino flux [6], possibly extending to the EHE region, may yield astrophysical background with rates of  $\lesssim 6$  events in the the present analysis sample, depending on its spectral shape.

## 3. Poisson-binned likelihood method

The Monte Carlo simulation events of the the IceCube EHE signals passing the final selection criteria of analysis [3] are filled into a histogram with bins of reconstructed zenith angle  $\theta$  and energy proxy  $E_{proxy}$ . The energy proxy used in this analysis was optimized to reconstruct the energy deposited by EHE muon tracks [13]. Although it does not give the best possible estimate for cascade events, it provides an unified analysis scheme in the EHE region regardless of event topologies.  $\theta$  is the result of reconstruction using a so-called single photoelectron log-likelihood (llh) fitting on the detector signals based on a track hypothesis [14]. For the events such as cascades,

in which direction is not well reconstructed, only the energy proxy information is used in the present analysis. Events with llh values inconsistent with tracks are categorized in this *non-track-like* category.

The event-number distributions on the plane of  $E_{proxy}$  and  $\cos(\theta)$  (energy-zenith plane) are obtained for different cosmic neutrino models. Similarly, the event-number distributions on the energy-zenith plane for atmospheric neutrino and muon background are obtained. To test a given cosmic neutrino model hypothesis, the expected number of signal and atmospheric background events in the  $i_{th}$  and  $j_{th}$  bins,  $\mu_{i,j}^{SIG}$  and  $\mu_{i,j}^{BG}$  are compared, respectively, with the observed number of events  $n_{i,j}$  via the Poisson probability function  $f_p(n_{i,j}, \mu_{i,j}^{SIG} + \mu_{i,j}^{BG})$ , where  $i$  is the index of the cosine of zenith angle and  $j$  of the energy proxy.

The product of the Poisson probabilities over all zenith and energy bins gives the binned Poisson likelihood:

$$L(\lambda) = \prod_{i,j} f_p(n_{i,j}, \lambda \mu_{i,j}^{SIG} + \mu_{i,j}^{BG}), \quad (3.1)$$

where  $\lambda$  is the multiplier for a signal model.  $\lambda = 1$  represents the signal model prediction.

A model test is performed by comparing the model hypothesis of  $\lambda = 1$  against the alternative hypothesis  $\lambda \neq 1$ . A test statistic is the log-likelihood ratio:

$$\Lambda = \log \frac{L(\hat{\lambda})}{L(\lambda = 1)}, \quad (3.2)$$

where  $\hat{\lambda}$  is the multiplier to maximize the Poisson likelihood  $L$ . An ensemble of pseudo experiments under the model hypothesis gives a PDF of the test statistic  $\Lambda$ . The p-value for a given model of cosmic neutrinos is subsequently calculated from the PDF by the frequency in which  $\Lambda$  is larger than the value obtained from the number of events in each bin, on the energy-zenith plane from the real data.

A test of the background-only hypothesis is also conducted using this scheme. The null hypothesis is represented by  $\lambda = 0$  in this case.

### 3.1 Model compatibility calculation

One of the important questions is whether the observed data is consistent with the expectations from the GZK cosmogenic model or more compatible with a softer power-law flux, such as  $E_\nu^{-2}$ , which is expected from astrophysical neutrinos. To test this hypothesis, a scheme similar to as one described in the previous section is used. In this case, the binned Poisson likelihood is introduced for both a GZK cosmogenic model and a power-law model:

$$\begin{aligned} L_{GZK}(\lambda_{GZK}) &= \prod_{i,j} f_p(n_{i,j}, \lambda_{GZK} \mu_{i,j}^{GZK} + \mu_{i,j}^{BG}), \\ L_{E_\nu^{-\alpha}}(\lambda_\alpha) &= \prod_{i,j} f_p(n_{i,j}, \lambda_\alpha \mu_{i,j}^\alpha + \mu_{i,j}^{BG}), \end{aligned} \quad (3.3)$$

where  $\mu_{i,j}^{GZK}$  is the number of events in a bin of the energy-zenith plane predicted by the GZK model, and  $\mu_{i,j}^\alpha$  is the value attributable to a generic astrophysical  $E_\nu^{-\alpha}$  power-law flux. The test statistic is:

$$\Lambda = \log \frac{L_{E_\nu^{-\alpha}}(\hat{\lambda}_\alpha)}{L_{GZK}(\hat{\lambda}_{GZK})}. \quad (3.4)$$

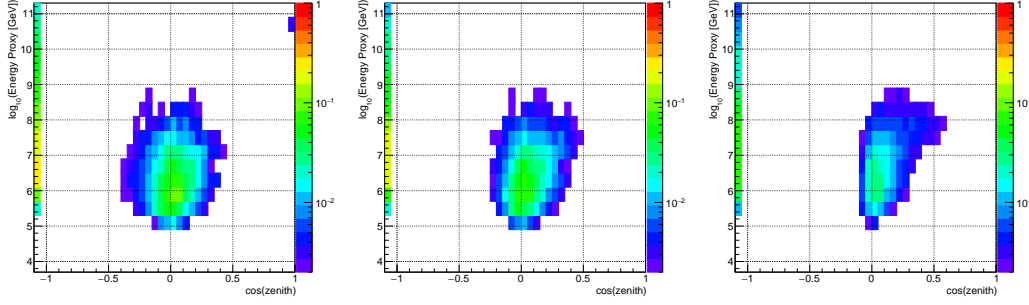


**Figure 1:** Expected event distributions on the plane of the energy proxy and cosine of the reconstructed zenith angle for the flux  $\phi_{\text{Diff}} = \kappa_E E_V^{-1}$ , spanning a one-decade energy interval centered at  $E_V^c$ . The event distributions are the sum of all three neutrino flavors. Events classified as the non-track-like category are plotted in the bins of  $\cos\theta = -1.1$ . From left to right, the distributions for  $\log_{10}(E_V^c/\text{GeV}) = 7.6, 8.0,$  and  $9.0$  are shown. Note that the energy proxy is not the best estimated deposited energy which can be obtained by dedicated energy reconstructions optimized for a given event topology. For display purposes, the normalization  $\kappa_E$  is set here so that the energy flux  $E_V^2 \phi_{\text{Diff}} = 1.0 \times 10^{-8} \text{ GeV}/\text{cm}^2 \text{ sec sr}$ , at an energy of  $E_V^c$ .

The multiplier with  $\hat{\phantom{x}}$  is the value needed to maximize the likelihood function.

### 3.2 Nuisance parameter to represent the astrophysical neutrino flux

As the EHE IceCube data sample is expected to contain events consistent with contributions from a generic astrophysical power-law flux [3], a test of any GZK cosmogenic neutrino model must incorporate the existence of a power-law flux forming astrophysical backgrounds. We account for this likelihood by introducing a nuisance flux in the form  $\phi_\alpha = \kappa_\alpha E_V^{-\alpha}$ , where  $\kappa_\alpha$  is an arbitrarily chosen normalization. A small modification of equation (3.3) gives:

$$L_{\text{GZK}}(\lambda_{\text{GZK}}, \lambda_\alpha) = \prod_{i,j} f_p(n_{i,j}, \lambda_{\text{GZK}} \mu_{i,j}^{\text{GZK}} + \lambda_\alpha \mu_{i,j}^\alpha + \mu_{i,j}^{\text{BG}}), \quad (3.5)$$

where  $\mu_{i,j}^\alpha$  is the number of events in a bin from the power-law flux with normalization  $\kappa_\alpha$ . Taking  $\lambda_\alpha$  as a nuisance parameter, the likelihood ratio is constructed using the profile likelihood:

$$\Lambda(\lambda_{\text{GZK}}) = \log \frac{L_{\text{GZK}}(\widehat{\lambda}_{\text{GZK}}, \widehat{\lambda}_\alpha)}{L_{\text{GZK}}(\lambda_{\text{GZK}}, \widehat{\lambda}_\alpha(\lambda_{\text{GZK}}))}, \quad (3.6)$$

where the double-hat notation indicates the profiled value of the nuisance parameter  $\lambda_\alpha$ , defined as the value that maximizes  $L_{\text{GZK}}$  for the specified  $\lambda_{\text{GZK}}$ . This likelihood ratio, in which  $\lambda_{\text{GZK}} = 1$ , is the test statistic for a given GZK cosmogenic model. The baseline model of the nuisance flux is built with  $\alpha = 2$ . We confirm that the impact of different power-law indices are negligible when constraints are placed in the EHE region. The p-values and the upper limits of the selected GZK models, which appear in our latest publication [3], were obtained using this procedure.

### 3.3 Differential limit calculation

As described in Section 1 with Eqs. (1.1–1.2), the differential limit at a neutrino energy of  $E_V^c$  is essentially the upper limit for the flux of  $\phi_{\text{Diff}} = \kappa_E E_V^{-1}$  ranging over an interval of one

decade  $[\log_{10}(E_\nu^c/\text{GeV}) - 0.5, \log_{10}(E_\nu^c/\text{GeV}) + 0.5]$ . The corresponding likelihood is obtained from equation (3.5) by replacing the number of events from a GZK flux with the number obtained from  $\phi_{\text{Diff}}$ , so that:

$$L_{\text{Diff}}(\lambda_{\text{Diff}}, \lambda_\alpha) = \prod_{i,j} f_p(n_{i,j}, \lambda_{\text{Diff}} \mu_{i,j}^{\text{Diff}}(E_\nu^c) + \lambda_\alpha \mu_{i,j}^\alpha + \mu_{i,j}^{\text{BG}}), \quad (3.7)$$

where  $\mu^{\text{Diff}}$  represents contributions from the flux  $\phi_{\text{Diff}}$  with the one-decade energy centered at  $E_\nu^c$ . Thus, this expression is a function of  $E_\nu^c$ . Figure 1 shows the distribution of  $\mu_{i,j}^{\text{Diff}}$  on the energy-zenith angle plane.

The test statistic is constructed as:

$$\Lambda(\lambda_{\text{Diff}}, E_\nu^c) = \log \frac{L_{\text{Diff}}(\widehat{\lambda_{\text{Diff}}}(E_\nu^c), \widehat{\lambda_\alpha})}{L_{\text{Diff}}(\lambda_{\text{Diff}}(E_\nu^c), \widehat{\lambda_\alpha}(\lambda_{\text{Diff}}(E_\nu^c)))}. \quad (3.8)$$

An ensemble of pseudo experiments to construct the PDF of  $\Lambda(\lambda_{\text{Diff}}, E_\nu^c)$  gives the upper limit of  $\lambda_{\text{Diff}}$  with a given confidence level, at an energy of  $E_\nu^c$ . By repeating the same procedure with varying  $E_\nu^c$ , the differential upper limit as a function of neutrino energy is produced.

For the previously published differential EHE limit [3], no nuisance parameter was used to account for an astrophysical background flux. It was found that the PDF of the test static  $\Lambda$ , given by Eq.(3.8), depends on the astrophysical normalization  $\kappa_\alpha$ . In the present analysis, a value of  $\lambda_\alpha = 0$  is used in pseudo-experiments for the PDF calculation since it results in the most conservative limit.

#### 4. Results and discussion

Two events passing the final selection criteria were observed. One event among them were found in the previous analysis and reported [3]<sup>1</sup>. The newly found event was detected in December 2016. It appears an uncontained shower event. The energy proxy of this event used in the present analysis ( $E_{\text{proxy}}$ ) is 2.72 PeV. Note that the best estimated energy of this uncontained shower event is different from the energy proxy value. Detail on its energy scale and the event topology classifications are not yet conclusive and are currently under investigation. We in particular study the possibility that it was produced by a prompt atmospheric muon from a decay of a charmed meson.

The hypothesis that they are backgrounds from atmospheric neutrinos and conventional atmospheric muons was tested by the likelihood ratio test statistic of Eq. (3.2) with  $\lambda = 0$  and rejected with a p-value of 0.024% ( $3.5\sigma$ ). They are compatible with a generic astrophysical  $E^{-2}$  power-law flux with a p-value of 78.8% while they are inconsistent with the GZK cosmogenic hypothesis with a p-value of 2.5% ( $2.0\sigma$ ), calculated using the test statistic of Eq. (3.6). They exhibit signatures of astrophysical neutrinos originating in the spectrum, extending from TeV to PeV energies rather than in a GZK spectrum peaking at energies in the EeV range, and are considered astrophysical backgrounds.

Figure 2 presents the derived all-flavor-sum differential upper limit using the current method based on the nine-year set of IceCube data. The three observed events weaken the limit below

<sup>1</sup>Of the two background events published in Ref. [3], one was discovered to be a detector artifact and has been removed.

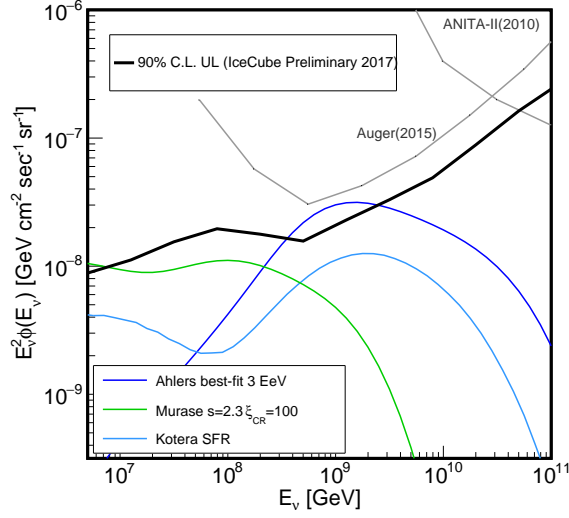


**Figure 2:** All-flavor-sum differential 90% CL upper limit based on the nine-year collection of IceCube data. Cosmogenic neutrino model predictions (assuming primary protons) by Kotera et al. [15], Ahlers et al. [16], and an astrophysical neutrino model by Murase et al. [17] are shown for comparison.

$4 \times 10^8$  GeV. The limit displays the constraints of the EHE cosmic neutrino flux on top of the power-law flux of astrophysical neutrinos inferred by the present data sample. Any departure from  $\alpha = 2$  in the nuisance  $\phi_\alpha$  model has a very minimal impact on the obtained limit, especially at energies of 300 PeV or higher, which is the main energy region of interest in this study. It was also confirmed that the present limit is insensitive to systematic uncertainties in the energy proxy and topology of the detected events.

The presented differential upper limit in the energy region between  $5 \times 10^6$  and  $5 \times 10^{10}$  GeV is the most significant model-independent upper limit currently reported. It indicates that models predicting a flux of  $E_\nu^2 \phi_{\nu_e + \nu_\mu + \nu_\tau} \simeq 2 \times 10^{-8}$  GeV/cm<sup>2</sup> sec sr at  $10^9$  GeV are disfavored by the current IceCube observation.

The present limit constrains a significant parameter space in EHE neutrino models that assume a proton-dominated UHECR composition. This constraint arises because the energy flux of UHECRs at 10 EeV,  $\sim 2 \times 10^{-8}$  GeV/cm<sup>2</sup> sec sr, is comparable to the present neutrino differential limit. The UHECR flux contributes only to the local universe at a radius of  $R_{\text{GZK}} \sim 100$  Mpc because of the energy attenuation of UHECR protons colliding with the cosmic microwave background. However, neutrinos are able to travel cosmological distances of  $O(c/H_0) \sim 4$  Gpc. Thus, UHECR sources within a sphere of  $\sim c/H_0$  contribute to the expected neutrino flux. This volume effect generally increases the neutrino flux relative to the UHECR flux by a factor of  $\sim c/H_0/R_{\text{GZK}} \sim O(10)$ . This balances the energy conversion factor from a UHECR proton to its daughter neutrino ( $5 \sim 10\%$ ), leading to an amount of neutrino energy flux comparable to the energy flux of UHECRs, if the observed UHECRs are protons, independent of the details of the neutrino production model.

## 5. Summary

We have introduced a new method that employs the binned Poisson likelihood method for deriving the quasi-differential upper limits of neutrino flux using a nine-year IceCube data set. A method using a nuisance parameter to represent astrophysical background determined by the observation data is presented. The differential upper limit based on nine years of IceCube data is obtained. The limit is the most stringent recorded to date in the energy range between  $5 \times 10^6$  and  $5 \times 10^{10}$  GeV. It indicates that any cosmic neutrino model that predicts a three-flavor neutrino flux of  $E_V^2 \phi_{\nu_e + \nu_\mu + \nu_\tau} \simeq 2 \times 10^{-8}$  GeV/cm<sup>2</sup> sec sr at  $10^9$  GeV is constrained.

## References

- [1] V. S. Berezinsky and G. T. Zatsepin, *Phys. Lett.* **28B** (1969) 423.
- [2] S. Yoshida and A. Ishihara, *Phys. Rev. D* **85** (2012) 063002.
- [3] M. G. Aartsen et al., (IceCube Collaboration), *Phys. Rev. Lett.* **117** (2016) 241101.
- [4] L. A. Anchordoqui et al., *Phys. Rev. D* **66** (2002) 103002.
- [5] G. J. Feldman and R. D. Cousins, *Phys. Rev. D* **57** (1998) 3873.
- [6] M. G. Aartsen et al., (IceCube Collaboration), *Phys. Rev. Lett.* **113** (2014) 101101; M. G. Aartsen et al., (IceCube Collaboration), *Astrophys.J.* **833** (2016) no.1, 3.
- [7] M. G. Aartsen et al., (IceCube Collaboration), *Journal of Instrumentation*, **12** (2017) P03012.
- [8] D. Heck et al., *Report FZKA* 6019 (1998);
- [9] E. J. Ahn, R. Engel, T. K. Gaisser, P. Lipari and T. Stanev, *Phys. Rev. D* **80** (2009) 094003.
- [10] A. Gazizov and M. P. Kowalski, *Comput. Phys. Commun.* **172** (2005) 203.
- [11] S. Yoshida et al., *Phys. Rev. D* **69** (2004) 103004.
- [12] M. G. Aartsen et al., (IceCube Collaboration), *Phys. Rev. D* **88** (2013) 112008.
- [13] M. G. Aarsten et al., (IceCube Collaboration) *J. Instrum.* **9** (2014) P03009.
- [14] J. Ahrens et al. (AMANDA Collaboration), *Nucl. Instrum. Methods Phys. Res., Sect. A* **524** (2004) 169.
- [15] K. Kotera, D. Allard, and A. Olinto, *J. Cosmol. Astropart. Phys.* **2010** (2010) 013.
- [16] M. Ahlers et al., *Astropart. Phys.* **34** (2010) 106.
- [17] K. Murase, Y. Inoue, and C. D. Dermer, *Phys. Rev. D* **90** (2014) 023007.



## Improving Future High-Energy Tau Neutrino Searches in IceCube

---

### The IceCube Collaboration<sup>†</sup>

<sup>†</sup> [http://icecube.wisc.edu/collaboration/authors/icrc17\\_icecube](http://icecube.wisc.edu/collaboration/authors/icrc17_icecube)

E-mail: [juliana.stachurska@icecube.wisc.edu](mailto:juliana.stachurska@icecube.wisc.edu)

One of the prime goals of the IceCube Neutrino Observatory is to identify tau neutrinos in the astrophysical neutrino flux. The most recent tau neutrino search is based on the high-energy starting event (HESE) sample and has not found any events that could be classified as tau neutrinos. However, this sample rejects all events in the outer detector region to suppress atmospheric background. Given the low expected number of identifiable tau neutrino events it is desirable to combine different suitable event selections in future searches. Here we present an approach where we use an event selection based on a shower-like event signature rather than a fiducial volume veto. This retains events in the outer parts of the detector while greatly reducing background from track-like events. We identify tau neutrino events by means of direct reconstruction of the double cascade topology. Based on Monte Carlo studies, combining this sample and the HESE sample will enhance the number of identifiable tau neutrino events by  $\sim 20\text{--}45\%$  for a given observation time at a similar background level.

**Corresponding authors:** J.Stachurska, M. Usner\*

*DESY, Platanenallee 6, D-15738 Zeuthen, Germany*

*35th International Cosmic Ray Conference — ICRC217*

*10–20 July, 2017*

*Bexco, Busan, Korea*

---

\*Speaker.

## 1. Introduction

The IceCube Neutrino Observatory is a km<sup>3</sup> Cherenkov detector at the South Pole [1]. It discovered an astrophysical flux of high energy neutrinos in 2012 [2]. The highest energies deposited in the detector by neutrino interactions are well above 1 PeV, meaning that the neutrinos responsible cannot have been produced locally in the Earth's atmosphere and must be of cosmic origin. If the dominant production mechanism is  $\pi^\pm$  decay resulting in a flavor ratio of  $\nu_e : \nu_\mu : \nu_\tau$  of 1 : 2 : 0 at the source, the expected flavor ratio on Earth is  $\nu_e : \nu_\mu : \nu_\tau \approx 1 : 1 : 1$  due to neutrino mixing [3]. Therefore, we expect one third of the astrophysical flux measured with IceCube to be caused by  $\nu_\tau$  interactions. With a negligible atmospheric  $\nu_\tau$  content [4, 5], identifying  $\nu_\tau$  interactions in the IceCube data would be yet another smoking gun signature of the cosmic origin of the highest-energy neutrino flux. However, to this day no  $\nu_\tau$  event has been identified with IceCube [6, 7].

There are three event topologies in IceCube to be distinguished. Track-like events stem from charged current  $\nu_\mu$  interactions and atmospheric muons, as well as charged current  $\nu_\tau$  interactions where the  $\tau$  lepton decays muonically (branching ratio of  $\sim 17\%$ ). Cascade-like events come from  $\nu_e$  or neutral current interactions, and from charged current  $\nu_\tau$  interactions where the  $\tau$  lepton decays too quickly to be resolved.

Only charged current  $\nu_\tau$  interactions can create a double cascade [8], where the first cascade comes from the neutrino interaction and  $\tau$  production, and the second from the  $\tau$  decaying electromagnetically or hadronically (branching ratio of  $\sim 83\%$ ). However, the  $\tau$  lepton has a mean decay length of  $\langle L_\tau \rangle \sim 50 \text{ m} \cdot E_\tau [\text{PeV}]$ , where  $E_\tau$  is the  $\tau$  energy. Therefore, charged current  $\nu_\tau$  interactions become distinguishable from  $\nu_e$  or neutral current interactions only at energies  $\gtrsim 100 \text{ TeV}$ . More details on these event topologies can be found in [7]. So far, two dedicated  $\nu_\tau$  analyses have been presented using different event selections. While [6] looked for double pulse signatures in the waveform of individual digital optical modules (DOMs) in 3 years of IceCube data, [7] searched for double cascades using direct reconstruction in 6 years of IceCube data. At neutrino energies  $\gtrsim 100 \text{ TeV}$ , where the  $\tau$  lepton can live long enough to create a resolvable double cascade signature in the detector, the measured neutrino flux is rather low. Here we present an approach to increase the event sample used for the double cascade search by combining different selections of high-energy neutrino events.

## 2. Data Samples

### 2.1 High-Energy Starting Events (HESE)

The HESE sample is based on the event selection described in [2]. A veto layer is used to suppress incoming atmospheric background, resulting in a decreased effective volume. All events are thereby required to start inside the detector. It is an all-flavor event selection, with events classified as cascade-like or track-like. As the HESE event selection does not discriminate event shapes, it retains a similarly high efficiency for  $\nu_\tau$  events at all tau decay lengths.

In the years 2012-2016, four cascade-like events with energies above 100 TeV were seen in HESE, but not in the cascade sample described below, as they did not fulfill all of the cascade-selection criteria. The currently available HESE sample contains 49 events with a deposited energy above 60 TeV in the years 2010-2016, with an estimated background of 9 atmospheric neutrino

events and 2 atmospheric muons [9]. This is the event selection used in [7], where the third event-topology of a double cascade has been introduced.

## 2.2 Contained Cascade Events

The contained cascade event selection makes use of almost the entire instrumented volume and uses topological criteria like the sphericity of the Cherenkov light pattern to select cascade-like events and reject track-like events [10, 11]. Therefore, the efficiency of the cascade event selection to  $\nu_\tau$  events is highest for events with short tau decay lengths that have spherical light patterns and decreases with increasing tau decay lengths.

The sample consists of six years (2010-2016) of cascades, of which the high- and medium-energy part above  $\sim 10$  TeV deposited energy will be used. In the time period between 2012 and 2016 there are 19 events with energies above 100 TeV, ten of which are not in the HESE sample. This includes one event originating from an interaction in a layer of ice where light is strongly attenuated due to a high concentration of dust particles. There is no contamination from atmospheric muons expected above 60 TeV deposited energy.

Due to the steeply falling spectrum of the astrophysical neutrino flux, most of the identifiable double cascade signal is expected to have tau decay lengths close to the resolution threshold. Therefore, the high-energy part of the cascade sample provides an excellent addition for a search for  $\nu_\tau$  interactions. The work presented here is the first study aimed at identifying  $\nu_\tau$  events in the contained cascade sample.

## 2.3 Uncontained Cascade Events

The outer parts of the detector are used as a veto region to varying degrees in both event selections described above. As shown in [10, 12], this area of the detector allows a reasonably good separation between astrophysical neutrino signal and atmospheric muon background. Events in the uncontained cascade sample have interaction vertices reconstructed at the rim of the detector, either close to the outer strings or below the instrumented volume. To suppress background from atmospheric muons, events with vertices at the corners of the detector are discarded and only high-energy events are kept. The event selection is designed to provide a sample that is statistically independent from the contained cascades sample. So far, it has been applied to two years (2010-2011) of data, but efforts are underway to extend the event selection to all currently available data. While this sample offers a gain in the number of identifiable  $\nu_\tau$  events, it is more difficult to reconstruct events not contained inside the detector with the presently used algorithms. Therefore, the addition of the uncontained cascade event sample for a  $\nu_\tau$  search is desirable, but challenging. This sample has not yet been used for follow-up  $\nu_\tau$  searches, either.

The event numbers for the published samples are summarized in Table 1, showing the number of events with reconstructed energies  $> 100$  TeV for all topologies (cascades and tracks), cascades only and cascades found only in that event selection. The effective areas for tau neutrinos for the three described event selections are shown in Figure 1. Note that the uncontained cascade event selection has only been applied to two years of data, and efforts are presently ongoing to extend the event selection; its effective area might therefore change.

event numbers (> 100 TeV)	all topologies	cascades	unique cascades
HESE 6-year	27	22	7
contained cascades 6-year	26	26	14
uncontained cascades 2-year	9	9	8

**Table 1:** Number of events with > 100 TeV reconstructed energy observed in the three samples considered. The number of events for all topologies, cascades, and the number of cascades found only in the given sample are shown. Note that the published uncontained cascade sample covers two years only.

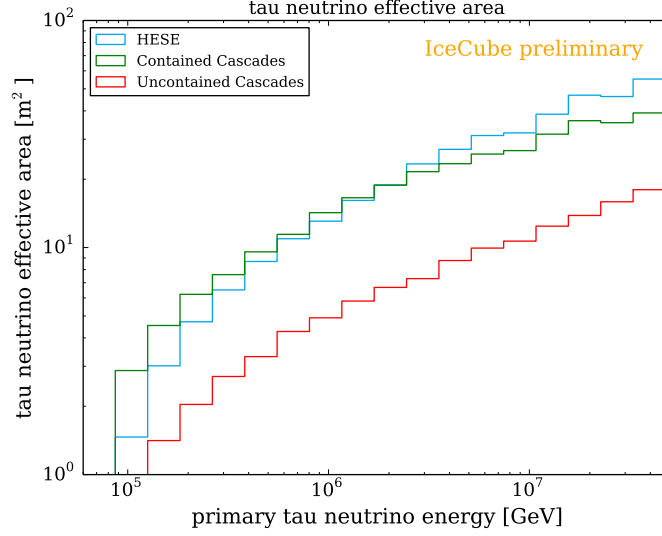


**Figure 1:** Effective areas for tau neutrino interactions using the HESE, contained cascade, and uncontained cascade event selections. Note that the uncontained cascade event selection is currently studied and might change.

### 3. Observables sensitive for tau neutrino identification

This study is done using a reconstruction where an algorithm maximizes the likelihood of the given event's light deposition using the double cascade hypothesis [7, 13]. Out of the nine fit parameters, three are used to identify double cascades: the energy of the first (hadronic) cascade creating a  $\tau$  lepton, the length the  $\tau$  lepton travels before it decays, and the energy of the second (hadronic or electromagnetic) cascade of the  $\tau$  decay. Figure 2 shows the simulated survival rate of astrophysical tau neutrinos with deposited energies above 60 TeV producing a double cascade as a function of tau decay length in the HESE, combined HESE + contained cascades, and combined HESE + contained cascades + uncontained cascades samples. Assuming an astrophysical flux of  $\Phi_{\nu_\tau} = 1.0 \cdot 10^{-18} \left(\frac{E}{100\text{TeV}}\right)^{-2} \text{ GeV}^{-1} \text{ cm}^{-2} \text{ s}^{-1} \text{ sr}^{-1}$ , 3.65 tau neutrino double cascade events per year are expected in the combined sample, but only 1.36 (0.86) of these have a resolvable tau decay length of > 10 m (> 20 m). The gain from including the contained cascade sample reaches  $\sim 50\%$  for the lowest resolvable lengths of  $\sim 10$  m as compared to the HESE sample alone, and  $\sim 80\%$  if both contained and uncontained cascades are included. The challenge is to resolve as many of the events with short decay lengths as possible.

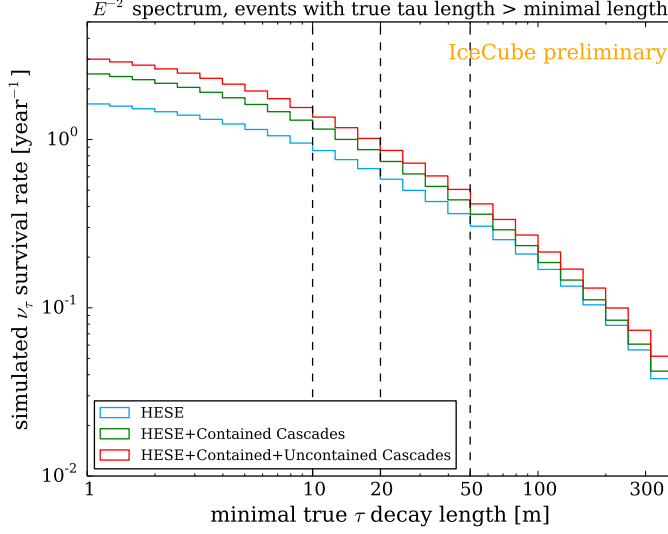


**Figure 2:** Simulated survival rates of astrophysical tau neutrino interactions with deposited energies above 60 TeV producing a double cascade as a function of tau decay length in the HESE, combined HESE + contained cascades, and combined HESE + contained cascades + uncontained cascades samples, assuming an astrophysical flux of  $\Phi_{\nu_\tau} = 1.0 \cdot 10^{-18} \left(\frac{E}{100\text{TeV}}\right)^{-2} \text{ GeV}^{-1} \text{ cm}^{-2} \text{ s}^{-1} \text{ sr}^{-1}$ .

The main goal of this study is then separating signal from background events based on the observables of the fit and classifying them as either double cascade, single cascade, or track in order to obtain signal and background rates for the combined data sample. Please note that the separation criteria here are not identical to the ones used in [7], and that we introduce a new variable in this work, the likelihood ratio, which we describe below. Only charged current  $\nu_\tau$  interactions can create a true double cascade. However, the shorter the tau decay length is, the more does the light pattern resemble that of a single cascade. Large stochastic energy losses along a muon track can mimic a double cascade.

A useful observable is the tau decay length  $L_\tau$ , where the algorithm gives a good resolution above 10 m. Single cascades tend to be reconstructed as either double cascades having small (below 10 m) separation lengths, or with an arbitrary separation length and one of the cascades having almost no energy. The latter is easily explained by a random noise hit somewhere in the detector far away from the neutrino interaction. For its removal the energy asymmetry  $A_E := \frac{E_1 - E_2}{E_1 + E_2}$  is used, with  $E_1$  ( $E_2$ ) being the reconstructed energy of the first (second) cascade. For single cascades, the values for  $A_E$  peak at  $\pm 1$ . Thus, events with high positive or negative energy asymmetries are classified as single cascades. In this work, we introduce a new parameter to distinguish double cascades from single cascades. We fix the tau decay length to 0 m and use the reconstruction algorithm to fit both cascades at the same point, thus making it a single cascade. The likelihood values are compared to the free minimization, and the event is only classified as a double cascade if the test statistics  $-2 \log \frac{\mathcal{L}(0\text{m})}{\mathcal{L}(\text{bestfit})} > 1$  is fulfilled. This is a powerful tool to distinguish between single and double cascades, as quite naturally, the single cascade hypothesis describes a real single cascade better.

Looking at track-like background, the energy asymmetry does not have a strong separation

power. There is, however, a physical correlation between the mean tau decay length and its energy: as mentioned above,  $\langle L_\tau \rangle \sim 50 \text{ m} \cdot E_\tau [\text{PeV}]$ , albeit with a large spread about the average value. This can be used to define a signal region in  $L_\tau$ -vs.- $E_2$  space, classifying events with  $L_\tau < 500 \text{ m} \cdot E_2 [\text{PeV}]$  as signal-like, and events with  $L_\tau \geq 500 \text{ m} \cdot E_2 [\text{PeV}]$  as track-like (this concept is illustrated in Figure 2 of [7]). These cuts allow for a 90% double cascade purity in the signal sample selected from contained cascades.

To get the same purity in the sample containing the additional HESE events, one more variable has to be used in addition to the cuts developed for the contained cascade sample as a final step to reduce the remaining track-like background. We use the energy confinement, i.e. the fraction of the total energy that is deposited in the vicinity of the reconstructed cascade vertices. Only events with a confined energy fraction close to 1.0 remain in the double cascade sample.

As the reconstruction algorithms used for this study have only been tested for events contained inside the detector volume, the study initially focused on double cascades with both vertices reconstructed inside the detector. This restriction poses a major challenge when aiming to extend the search for  $\nu_\tau$  interaction to events that do not have both vertices contained inside the detector. Currently the performance of the algorithm and cuts for events that are outside the detector boundaries is being studied.

#### 4. Results from the combined sample

The expected signal and background rates are investigated for the contained cascade and the HESE sample separately, as well as for the combination of both samples. Note that the contained cascade sample has significant overlap with the HESE selection;  $\sim 50\%$  of the events in the combined sample pass both event selections. While there is no overlap between contained and uncontained cascades by construction, there is some overlap between the HESE and uncontained cascades

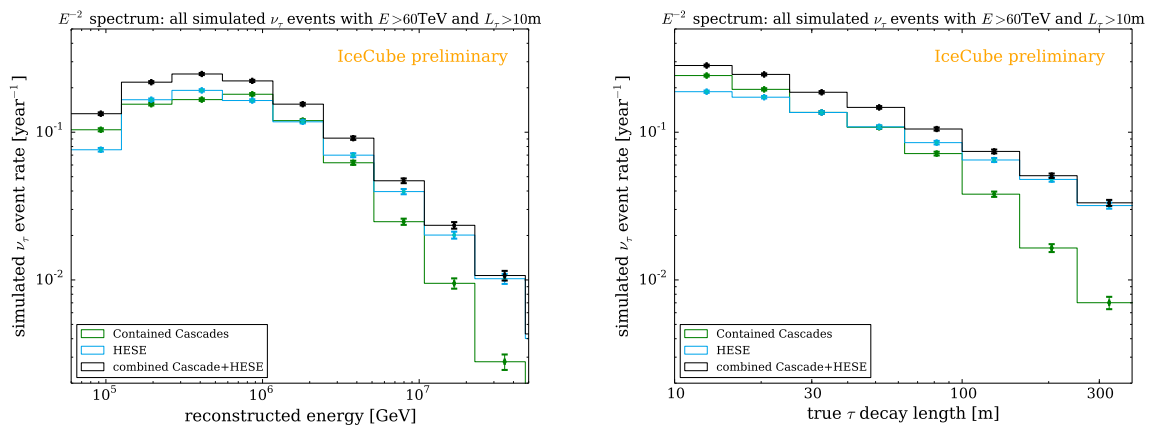


**Figure 3:** Simulated passing rates of astrophysical tau neutrino interactions with deposited energies above 60 TeV producing a double cascade with separation  $> 10 \text{ m}$  in the contained cascades and HESE event selection, and the combined sample for the same flux as in Figure 2. **Left:** Passing rate as a function of energy. **Right:** Passing rate as a function of tau decay length.

samples from events at the bottom of the detector. This has been taken into account properly when combining the samples.

Figure 3 shows the passing rates of astrophysical tau neutrino interactions in the contained cascades and HESE samples, as well as in the combined sample. Given the nature of the event selections considered here, it is not surprising that the cascade sample retains many  $\nu_\tau$  events with low tau decay lengths, while the HESE sample has a much higher efficiency for  $\nu_\tau$  events with tau decay lengths above  $\sim 100$  m, as the contained cascades event selection selects shower-like topologies and rejects events with elongated or track-like light patterns. Combining both samples for a search for  $\nu_\tau$ -interactions is thus desirable.

Our results are shown in Figure 4. For reconstructed tau decay lengths  $> 20$  m, the combined sample will lead to an increase in identifiable tau neutrino events by  $\sim 30\%$  as compared to the HESE selection alone assuming a hard spectrum with a spectral index of  $\gamma = -2$ . The expected gain in the 10-20 m separation length region is even higher at  $\sim 50\%$ . With this spectrum,  $\sim 3$  signal events with separation lengths above 20 m are expected in the combined sample with eight years of data, at a background level of 10 %. With a measured spectral index of  $\gamma - 2.48 \pm 0.08$  in the cascade sample [11], the number of very high-energy events is expected to be lower. Therefore, it is even more important to extend the  $\nu_\tau$  search to the cascade sample, as it has a larger effective area than HESE at lower energies and separation lengths. For the softer spectral index of  $-2.48$ ,  $\sim 2$  events are expected in the combined sample for eight years of data, for separation lengths  $> 20$  m. The gain from including the cascade sample is shown in Table 2 for both spectra.

The uncontained event selection provides additional events not seen in either of the other samples. However, the performance of the double cascade reconstruction algorithm on uncontained events needs to be studied further. Assuming that a similar efficiency as for contained events can

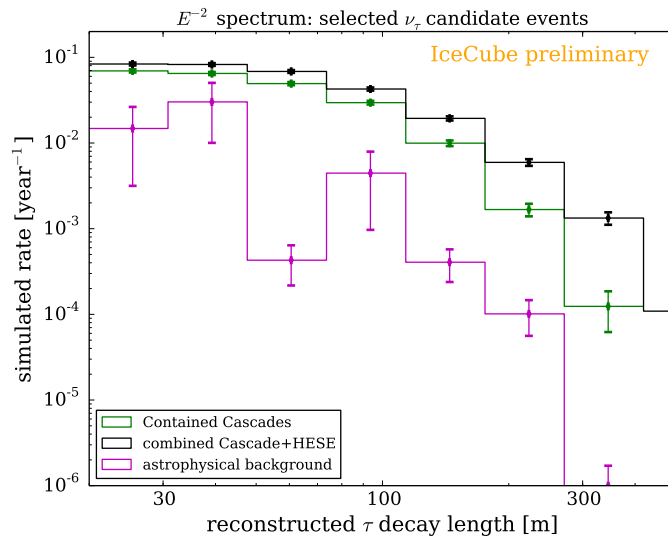


**Figure 4:** Simulated rates of identifiable astrophysical tau neutrino interactions with a reconstructed double cascade with separation  $> 20$  m in the contained cascades and the contained cascades + HESE combined sample after cuts have been applied, assuming the same flux as in Figure 2.



energy spectrum tau decay length	$E^{-2}$		$E^{-2.48}$	
	10 – 20 m	> 20 m	10 – 20 m	> 20 m
gain from including cascades	~ 50 %	~ 30 %	~ 65 %	~ 35 %
	~ 40 %		~ 50 %	

**Table 2:** Gain in the observable number of events with  $> 60$  TeV deposited energy from combining the contained cascade sample with the HESE sample. The  $E^{-2}$  spectral index denotes the flux used in Figure 2, the  $E^{-2.48}$  spectral index denotes the flux observed in [11].

be achieved, an additional  $\sim 15\%$  identifiable tau neutrino events can be added to the combined HESE and contained cascades sample.

## 5. Summary and Outlook

Six years of IceCube data have not yet revealed astrophysical  $\nu_\tau$  interactions. However, the most promising search to date has been based on only the HESE sample, with an expectation of  $\sim 2$  identifiable  $\nu_\tau$  events [7]. Combining this effort with the high-energy part of the contained cascade sample increases the expected number of identifiable  $\nu_\tau$  events by  $\sim 30\%$  in the almost background free region of separation lengths  $\geq 20$  m and by  $\sim 50\%$  for separation lengths of 10-20 m. For a softer spectrum, the importance of combining the two samples is even higher, and the gain from incorporating the cascade sample is  $\sim 65\%$  for separation lengths of 10-20m.

Another not yet incorporated sample is given by the uncontained cascades. While the reconstruction algorithms used have been developed for events that are contained within the fiducial volume, a study of their efficiency on not fully contained events is underway. If a good separation between double cascades and background can be achieved, another  $\sim 15\%$  gain in  $\nu_\tau$  events (compared to the combined sample of contained cascades and HESE) is possible.

## References

- [1] **IceCube** Collaboration, M. G. Aartsen et al., *JINST* **12** (2017) P03012.
- [2] **IceCube** Collaboration, M. G. Aartsen et al., *Science* **342** (2013).
- [3] M. Bustamante, J. F. Beacom, and W. Winter, *Phys. Rev. Lett.* **115** (2015) 161302.
- [4] M. Honda, T. Kajita, K. Kasahara, S. Midorikawa and T. Sanuki, *Phys. Rev. D* **75** (2007) 043006.
- [5] R. Enberg, M. H. Reno, and I. Sarcevic, *Phys. Rev. D* **78** (2008) 043005.
- [6] **IceCube** Collaboration, M. G. Aartsen et al., *Phys. Rev.* **D93** (2016) 022001.
- [7] **IceCube** Collaboration, [PoS \(ICRC2017\) 974](#) (these proceedings).
- [8] J. G. Learned and S. Pakvasa, *Astropart. Phys.* **3** (1995) 267–274.
- [9] **IceCube** Collaboration, [PoS \(ICRC2017\) 981](#) (these proceedings).
- [10] **IceCube** Collaboration, [PoS \(ICRC2015\) 1109](#) (2016).
- [11] **IceCube** Collaboration, [PoS \(ICRC2017\) 968](#) (these proceedings).
- [12] Stoessl, A., *PhD thesis* (2015).
- [13] **IceCube** Collaboration, M. G. Aartsen et al., *JINST* **9** (2014) P03009.

## Search for Astrophysical Tau Neutrinos with the IceCube Waveforms

---

### The IceCube Collaboration

[http://icecube.wisc.edu/collaboration/authors/icrc17\\_icecube](http://icecube.wisc.edu/collaboration/authors/icrc17_icecube)

*E-mail:* [lwille@icecube.wisc.edu](mailto:lwille@icecube.wisc.edu)

The IceCube Neutrino Observatory has detected a diffuse astrophysical neutrino flux which is expected to have a close to equal ratio of neutrino flavors due to thorough mixing over astronomical baselines. However, IceCube has yet to detect astrophysical tau neutrinos. A tau neutrino undergoing charged current interaction will have two subsequent energy losses, the first from the neutrino interaction and the second from the decay of the secondary tau lepton. At PeV neutrino energies, IceCube can resolve these depositions as two separated cascades. At energies near hundreds of TeV the cascades are not well separated but can be observed as a double pulse waveform in individual IceCube sensors. Here we will present three techniques to improve tau double pulse waveform identification. One technique utilizes neighboring IceCube light sensors to observe a double pulse event, another incorporates machine learning algorithms to boost detection of double pulses, and the third explores the possibility of stacking waveforms to increase the double pulse signal. The first two approaches show a promising increase of signal rates by at least 50% while keeping similar or lower backgrounds at the double pulse waveform identification stage.

**Corresponding authors:** Sandro Kopper<sup>1</sup>, Maximilian Meier<sup>2</sup>, Logan Wille<sup>\*3</sup>, and Donglian Xu<sup>3</sup>

<sup>1</sup> *Department of Physics and Astronomy, University of Alabama, Tuscaloosa, AL 35487, USA*

<sup>2</sup> *Lehrstuhl für Experimentelle Physik V, Technische Universität Dortmund, 44227 Dortmund, Germany*

<sup>3</sup> *Wisconsin IceCube Particle Astrophysics Center and Department of Physics, University of Wisconsin, Madison, WI 53703, USA*

*35th International Cosmic Ray Conference - ICRC217 -  
10-20 July, 2017  
Bexco, Busan, Korea*

---

<sup>\*</sup>Speaker.

## 1. Introduction

IceCube has discovered a flux of high energy neutrinos which is currently consistent with an origin of unknown astrophysical sources [1]. These astrophysical neutrinos stream to IceCube from extragalactic and galactic sources, covering astronomical distances during which they oscillate flavors. Regardless of the flavor composition at production, the neutrino flux oscillates to a nearly equal 1:1:1 flavor composition [2] assuming standard neutrino oscillations. The direct observation of a  $\nu_\tau$  will be an additional confirmation of astrophysical origin of high energy neutrinos observed by IceCube due to a substantially smaller atmospheric background [3]. A recent global analysis from IceCube found the flavor ratio to be consistent with 1:1:1 but with large uncertainties [4, 5]. This is partly due to IceCube not yet identifying a  $\nu_\tau$  [6, 7], which is consistent with expectations. A precise flavor ratio measurement will help constrain new physics in previously unconstrained neutrino oscillation sectors [2, 8]. We will present three improved techniques to identify  $\nu_\tau$  interacting inside of IceCube.

IceCube is a cubic kilometer detector at the geographic South Pole designed to detect GeV-PeV neutrinos. The detector consists of 86 strings, 78 spaced at 125 m and 8 strings in the center with closer spacing, each holding 60 digital optical modules (DOMs). The 78 strings spaced at 125 m hold the DOMs equally spaced at depths between 1450 m to 2450 m below the surface and the 8 closer spaced strings hold 50 DOMs between 2100 m to 2450 m and 10 DOMs between 1900 m to 2000 m [9]. This array of DOMs encompasses 1 gigaton of ultra-transparent glacial ice, making the largest calorimetric detector in the world. Each DOM consists of a 10 inch PMT connected to digitizing electronics. The waveforms collected by the PMTs are digitized before being sent to the surface. There are two types of waveform digitization, the Analog Transient Waveform Digitizer (ATWD) and the Fast Analog to Digital Converter (FADC). Two of the techniques presented here use the ATWD digitization which provides the most detailed description of the photon arrival time available. The ATWD uses three gain factors, 16, 2, 0.25, over a nominal gain of  $10^7$ . During digitization the highest gain without saturation is used to capture the finest details of the waveform. The ATWD captures the waveform in 3.3 ns bins with 128 samples.

## 2. Tau Neutrinos in IceCube

IceCube observes the Cherenkov light produced by the secondary particles created in the interaction of the neutrino with the ice nuclei. A  $\nu_\tau$  undergoing a charged-current interaction can have a unique topology in IceCube. The interaction produces a  $\tau$  lepton which travels a distance about 50 m per PeV of the  $\tau$  lepton energy away from the interaction vertex and subsequently decays. If the  $\tau$  decays to hadrons or an electron there will be exactly two high energy depositions following the neutrino interaction as shown in Fig. 1 (left). However, IceCube can only distinguish the two depositions if the  $\tau$  has a sufficiently long life time, which corresponds roughly to a  $\tau$  that has traveled 5 m and above. If the tau decay length is long enough ( $>50$  m), the two depositions can be resolved and reconstructed separately. This topology is referred to as a double bang [6, 10]. At more intermediate lengths (5-50 m) the two losses cannot be well separated, but may create two pulses in an optical module waveform, referred to as a double pulse. A search for these double pulse events in 3 years of IceCube was conducted and found zero double pulse events which was

consistent with the expectation [7]. In these proceedings we present three techniques that improve the algorithm previously used to identify double pulses in waveforms and remove single cascade event backgrounds, Fig. 1 (right) shows exemplary signal and background waveforms. Not discussed in these proceedings is the necessary separation of track-like background events generated by  $\nu_\mu$  charged current interactions and atmospheric muons. These track-like events can create a double pulse signal due to subsequent stochastic losses near DOMs but are straight forward to remove due to their event shape.

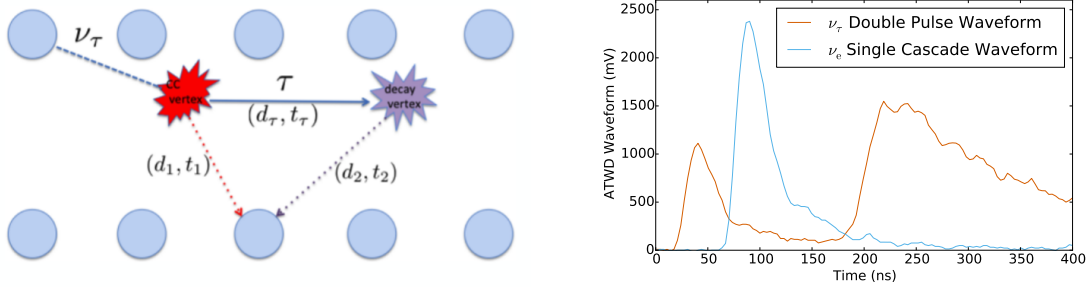


Figure 1: Left: Diagram (not to scale) showing a  $\nu_\tau$  undergoing a charged current interaction inside of IceCube. The blue spheres depict IceCube DOMs not drawn to scale. The two energy depositions of the charged current interaction and subsequent  $\tau$  decay can be observed by a single DOM which creates a double pulse waveform. Right: Simulated ATWD waveforms recorded by individual DOMs. While a charged current  $\nu_\tau$  interaction creates a double pulse, a  $\nu_e$  charged current interaction is observed as a single pulse. The goal of the double pulse identification is to separate these two types of waveforms.

### 3. Double Pulse Waveform Identification Techniques

#### 3.1 Local Coincident Double Pulse Waveforms

Double pulse events are only observable in energetic, bright events, and in DOMs near the interaction vertex. Therefore, events with less than 2000 detected photoelectrons (PE) are rejected, and only the ATWD waveforms of individual DOMs which detected at least 432 PE are analyzed for a double pulse waveform. The original double pulse identification (DPI) was designed to find double pulse waveforms in individual DOMs while rejecting single pulse waveforms. The necessary features to identify a double pulse are the rising and falling edge of the first pulse and the rising edge of the second pulse. A second pulse falling edge is not necessary to search for as it is a guaranteed feature and offers no discriminating power. First a sliding time window is used to find the start of the waveform pulse. Then the rising and falling edges are found by calculating the time derivative of the waveform smoothed over 4 ATWD time bins, a 13.2 ns period. Once the necessary edges are found, their duration and steepness are determined and used to decide if the waveform is a double pulse. High thresholds for the rising and falling edges were necessary to reduce the single cascade background waveforms which can have additional structure due to scattering light and statistically varying light. These high thresholds also reduce the signal rate of  $\nu_\tau$  events.

Table 1: Comparison of the threshold values from the improved local coincidence method to the method used in the previous analysis. These are threshold values for declaring a waveform with two rising edges and a falling edge a double pulse.

	LC Method	PRD 93.022001
1st Rising Edge Steepness	>1 mV/ns	>10 mV/ns
1st Rising Edge Duration	>13.2 ns	>26.4 ns
Falling Edge Steepness	<-0.5 mV/ns	<-17 mV/ns
Falling Edge Duration	>26.4 ns	>26.4 ns
2nd Rising Edge Steepness	>12 mV/ns	>18 mV/ns
2nd Rising Edge Duration	>39.6 ns	>39.6 ns

The improved method, referred to as Local Coincidence (LC) method, adds a requirement for the double pulse waveform to be observed in pairs of nearest or next-to-nearest DOMs. A single cascade event tends to not create irregular waveforms in multiple DOMs while a double cascade tends to create double pulses in multiple DOMs. This allows a lower threshold widths and steepness of the rising and falling edges of the double pulse waveform without increasing the background rate. The threshold values of the original DPI and the LC modification are shown in Table 1. These thresholds were found by scanning over the six parameters and picking the set with the highest signal rate while keeping a 10:1 signal to single cascade background rate. One notable difference between the two thresholds is the significantly smaller rising edge threshold of the LC method. A first rising edge is a feature in both single cascade and double cascade events and so is not a good discriminator between background and signal. However, in the original method the first rising edge threshold was large to reduce prepulsing single cascade events. In the improved method this background is not a concern because prepulsing is a random process and rarely occurring in multiple DOMs in an event.

$\nu_\tau$  interactions tend to have low inelasticity because of mass threshold effects of  $\tau$  production, which manifests in IceCube as a small first energy deposition and more energetic second deposition. Decreasing the first pulse threshold makes this low inelastic phase space observable. Additionally the overall decrease in the double pulse thresholds makes lower energy  $\nu_\tau$  events observable. Both of these effects increase the effective area, as shown in Fig. 2. Overall the LC technique has a 50% increase in signal rate over the previous technique while maintaining a similar signal purity. A Monte Carlo event that passes the improved selection that would have been previously rejected is shown in Fig. 2.

### 3.2 Machine Learning Based Double Pulse Selection

A further next improvement under consideration is to employ multivariate machine learning algorithms. The event selection used in this approach consists of two major steps. First, quality cuts identical to those discussed in section 3.1 are applied. Following the quality cuts, samples of signal waveforms and background waveforms are selected which are used to train a Random Forest [11]. As in the LC method, the goal is to reject waveforms from events with single cascade topologies while retaining as many double pulse waveforms as possible.

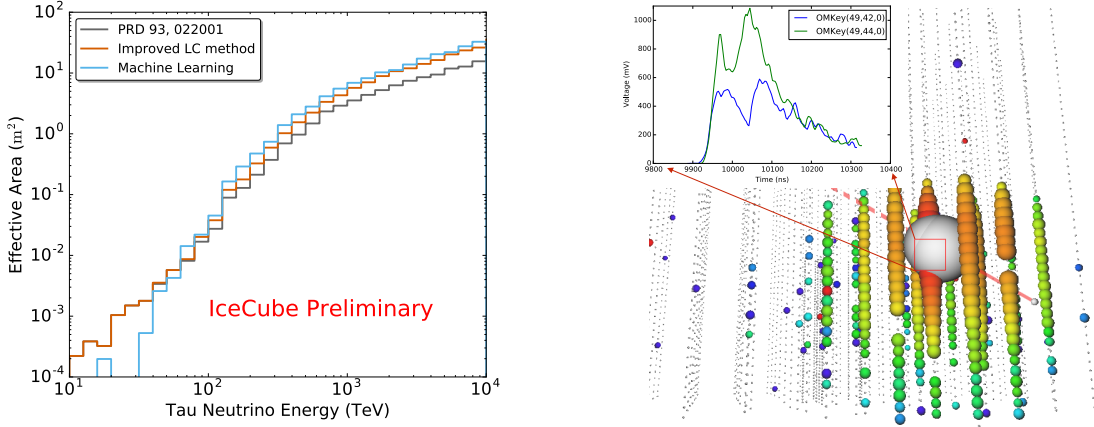


Figure 2: Left: Effective areas for the previous 3 year analysis, denoted by PRD 93.022001, the improved local coincident method discussed in section 3.1, and the machine learning technique discussed in section 3.2. Right: Monte Carlo event that passes the re-optimized LC double pulse algorithm that would have been rejected by the previous analysis. This is a simulated down-going  $\nu_\tau$  event with  $E_\nu = 385$  TeV undergoing CC interaction in the detector. The two overlapping spheres in grey indicate the interaction and decay vertices with deposited energies of 111 TeV and 273 TeV respectively. The tau decay length is 12 m.

All waveforms that pass the quality cuts, are characterized by the same features calculated on their derivative as explained in section 3.1. Here, feature denotes an observable quantity of a particular waveform. Signal waveforms for training the Random Forest are selected by a set of cuts on these features which is described in [12]. These cuts were optimized to retain as many double pulse waveforms from a hand-selected sample as possible by applying rather loose cuts to the steepness of the first and second rising edge with no restrictions on the falling edge steepness. They were later re-optimized to reject single cascade waveforms more efficiently.

Background waveforms for training are sampled uniformly at random from all single cascade background components (all flavor neutral current neutrino events and charged current electron neutrino events) according to their relative occurrence of expected waveforms from an assumed  $E^{-2.13}$  astrophysical flux [13]. In addition to the already described derivative features, eight new features are added. The new features are primarily focused on characterizing the statistical properties of the waveforms, their smoothness and their consistency with a single cascade waveform. The waveform mean, an energy proxy, allows the model to easily vary cuts depending on the energy deposited in the DOM. Another important feature describes the agreement of the waveform with a fit to an exponential function starting at the maximum of the first pulse. A good agreement is consistent with single cascade waveforms.

These features are used in a Random Forest [11] to distinguish double pulse waveforms from single cascade waveforms. The forest is trained and tested in a 10-fold cross validation with 200 trees, using  $\sim 6500$  signal and  $1.8 \cdot 10^6$  background waveforms. The resulting Random Forest score distributions for signal and background waveforms are shown on the left side of Fig. 3. The output of the Random Forest is a score from 0 to 1, spanning waveforms that are more background-like to



those that are more double pulse-like.

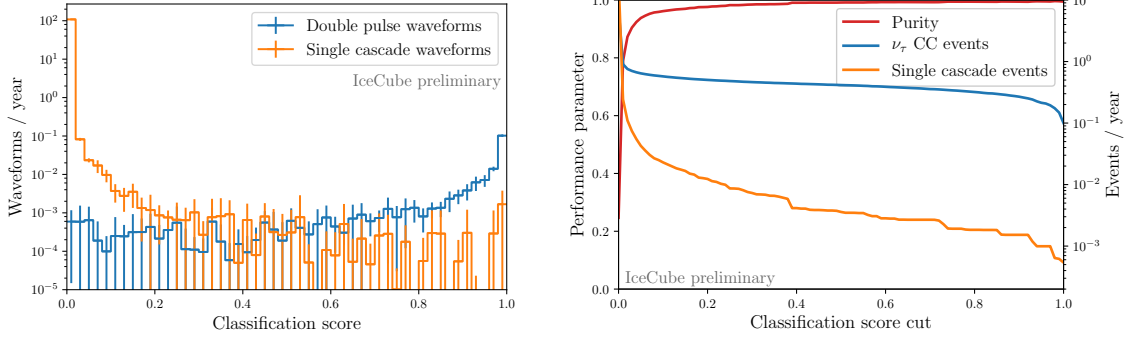


Figure 3: Results of the double pulse waveform selection. Left: Distribution of the classification score of the waveforms. The standard deviation of each bin is determined within the cross validation. Right: Purity as well as the expected remaining event rates per year as a function of the classification score cut.

This selection requires at least one waveform per event passing the Random Forest score cut. The right side of Fig. 3 shows the resulting purity as well as expected event rates from  $\nu_\tau$  CC interactions and all single cascade background components. The score cut was chosen at 0.2 to retain as much signal as possible, while still reaching a purity of  $\sim 97\%$ . The assumed astrophysical flux is an unbroken power law with a per flavor normalization of  $0.9 \cdot 10^{-18} \text{ GeV}^{-1} \text{ cm}^{-2} \text{ s}^{-1} \text{ sr}^{-1}$  at 100 TeV and a spectral index of 2.13 [13]. Expected remaining event rates for signal and single cascade background components can be found in Tab. 2. The resulting effective area of this selection in comparison to [7] at the same analysis stage is depicted on the left in Fig. 2. It shows an improvement of the effective area with respect to the original DPI at energies above  $\sim 70$  TeV which leads an increase in expected signal rate of around 50 %.

### 3.3 Charge Stacking Technique

Another way to extend the double pulse analysis currently under investigation is to stack the information gained from multiple DOMs. Instead of using the raw waveforms, a common frame of time and charge amplitude across all DOMs based on unfolded charge-timing information is produced and analyzed [14].

The stacked charge information is ideally the recovered arrival time of all the photoelectrons produced within the DOMs and so not a continuous function. It is much coarser than the original waveforms. Thus, the double pulse identification algorithm had to be adjusted. The extracted charge of each DOM being stacked is combined in a single charge-time distribution with 12 ns time bins starting at the time that 1% of the total charge has been deposited within the whole

Table 2: Preliminary event rates for signal and single cascade background components of the machine learning based double pulse selection. The assumed astrophysical flux can be found in [13]. Uncertainties are statistical only.

Event Type	Events per year
Astrophysical $\nu_\tau$ CC	$0.486 \pm 0.005$
Astrophysical $\nu_e$ CC	$0.010 \pm 0.001$
Astrophysical $\nu$ NC	$0.004 \pm 0.001$



detector. The distribution is further smoothed using a three bin moving average ("box smoothing") algorithm. For an example of such a histogram compare Fig. 4 (left). An upper time bound of the distribution of 500 ns is chosen to avoid issues with the known "afterpulsing" behavior of DOMs [9] that might mimic a second pulse. To ensure a proper reconstruction quality and to meet minimum energy requirements a total charge of 1000 PE within the whole detector and a charge of 100 PE deposited in the time bin with the highest charge is demanded to pass the selection. The requirements for the pulse identification algorithm differ for the first and second pulses. Since the beginning of the first pulse often falls outside the previously defined start time, the first pulse is defined as either a region of positive "slope" followed by a region of at least three bins of negative "slope" or simply a region of at least three bins of negative "slope" starting from the beginning of the distribution. The "slope" is being defined by the use of derivative proxies  $D_i$  at bin  $n$ . The three proxies  $D_1, D_2, D_3$  used are based on the charge  $Q_n$  of neighboring bins:  $D_i \propto (Q_{n+i} - Q_{n-1})$ .

If any of the proxies has the same sign as the "slope" in the previous bin, it is considered unchanged. The additional requirement for the second pulse is an amplitude of at least half that of the highest charge bin in the distribution and a minimum start time of 100 ns. Unlike for the first pulses, both a rising and falling edge are now required. As before the falling (rising) edge is defined by at least three bins of negative (positive) derivative  $D$  using any of the three proxies.

Depending on the exact event geometry stacking the charge of multiple neighboring DOMs can lead to very sharp, short time frame charge pulses. This is caused by arrival time difference of light corresponding to the distance of the DOMs instead of the geometric difference between the  $\nu_\tau$  interaction and  $\tau$  decay. The algorithm removes these "false" double pulses by requiring that none of the bins defining the start of the falling edge have a charge smaller than half the amplitude of the pulse. For an example of this charge structure compare Figure 4 (right).

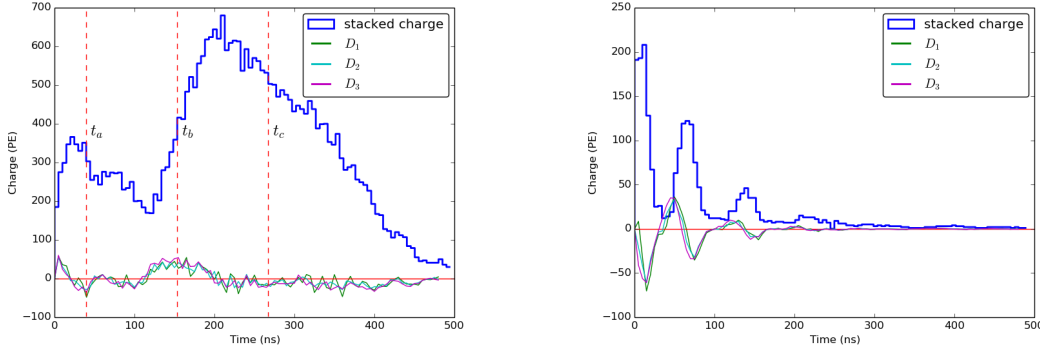


Figure 4: Left: Example of a stacked charge distribution of a  $\nu_\tau$  event for the brightest string. At times  $t_a$ ,  $t_b$  and  $t_c$  the slope shows a falling, a rising and another falling behavior respectively. Right: Stacking the charge information can lead to multiple pulses for single cascade events. The time structure corresponds to the DOM separation. Lower curves: Derivative proxy  $D_i$  behavior.

The final open issue remaining for this technique is how to choose which DOMs to stack. The first naïve choice is to use them all. This, however, introduces a similar false positive problem as mentioned before due to the large separation between the IceCube strings. This time though, the distance is of the same order of magnitude as the actual separation of the interaction and decay

vertices of the  $\nu_\tau$  signal and so cannot easily be removed. A way around this is to only consider DOMs on the string with the highest total charge. Still, charge information of too many DOMs far from the event vertex "wash out" the double pulse signal and lead to a rather low passing rate of signal events. A promising approach seems to be to start with a selection of a combination of any two adjacent DOMs on the string and see if the event passes the selection. If not, we take three, four, etc. adjacent DOMs and repeat the algorithm until either the algorithm finds a double pulse or all combinations have been checked. If no double pulses are found the event is considered a background event. For a benchmark  $E^{-2}$  spectrum this leads to a signal passing rate of  $\approx 0.24$  events per year with a  $\nu_e$  event background contribution that is  $< 5\%$ . The overlap fraction with the original double pulse method [7] is smaller than  $1/3$  showing that this method adds additional information.

In addition to members of the IceCube collaboration we'd like to acknowledge the work of James Parkes who was directly involved in developing this technique.

#### 4. Conclusion and Outlook

The direct observation of a  $\nu_\tau$  interaction in IceCube will be another confirmation of astrophysical neutrinos and can shed light on potential new physics. IceCube has yet to identify a  $\nu_\tau$  interaction but becomes more likely with increased observation time and improved methods as presented here. The improved double pulse identification methods presented here use more sophisticated techniques and additional information than the previous method that allows IceCube to access double cascade  $\nu_\tau$  events at lower energies and previously unexplored phase spaces.

#### References

- [1] **IceCube** Collaboration, [PoS \(ICRC2015\) 1081](#) (2016).
- [2] C. A. Argüelles, T. Katori, and J. Salvado, *Phys. Rev. Lett.* **115** (2015) 161303.
- [3] A. Fedynitch, R. Engel, T. K. Gaisser, F. Riehn, and T. Stanev, *EPJ Web Conf.* **99** (2015) 08001.
- [4] **IceCube** Collaboration, M. G. Aartsen et al., *Astrophys. J.* **809** (2015) 98.
- [5] **IceCube** Collaboration, M. G. Aartsen et al., *Phys. Rev. Lett.* **114** (2015) 171102.
- [6] **IceCube** Collaboration, [PoS \(ICRC2017\) 974](#) (these proceedings).
- [7] **IceCube** Collaboration, M. G. Aartsen et al., *Phys. Rev. D* **93** (Jan, 2016) 022001.
- [8] M. Bustamante, J. F. Beacom, and W. Winter, *Phys. Rev. Lett.* **115** (2015) 161302.
- [9] **IceCube** Collaboration, M. G. Aartsen et al., *JINST* **12** (2017) P03012.
- [10] **IceCube** Collaboration, [PoS \(ICRC2017\) 973](#) (these proceedings).
- [11] L. Breiman, *Machine Learning* **45** (2001) 5–32.
- [12] **IceCube** Collaboration in *Proceedings, 33rd International Cosmic Ray Conference (ICRC2013): Rio de Janeiro, Brazil, July 2-9, 2013*, p. 0643.
- [13] **IceCube** Collaboration, M. G. Aartsen et al., *Astrophys. J.* **833** (2016) 3.
- [14] **IceCube** Collaboration, M. G. Aartsen et al., *Journal of Instrumentation* **9** (2014) P03009.